Numerical modelling of a parabolic trough solar collector

Centre Tecnològic de Transferència de Calor
Departament de Màquines i Motors Tèrmics
Universitat Politècnica de Catalunya

Ahmed Amine Hachicha
Doctoral Thesis

Numerical modelling of a parabolic trough solar collector

Ahmed Amine Hachicha

TESI DOCTORAL

presentada al

Departament de Màquines i Motors Tèrmics
E.T.S.E.I.A.T.
Universitat Politècnica de Catalunya

per a l'obtenció del grau de

Doctor per la Universitat Politècnica de Catalunya

Terrassa, September, 2013

Numerical modelling of a parabolic trough solar collector

Ahmed Amine Hachicha

Directors de la Tesi

Dr. Ivette Rodríguez Pérez
Dr. Assensi Oliva Llena

Tribunal Qualificador

Dr. Carlos David Pérez-Segarra
Universitat Politècnica de Catalunya
Dr. José Fernández Seara
Universidad de Vigo
Dr. Cristobal Cortés Garcia
Universidad de Zaragoza
Dr. Jesús Castro González
Universitat Politècnica de Catalunya
Dr. Maria Manuela Prieto González
Universidad de Oviedo

In the name of God, Most
Gracious, Most Merciful

Acknowledgements

It would not have been possible to complete this doctoral thesis without the guidance of my PhD advisors, help from friends, and support from my family.

I would like to express my deepest gratitude to Prof Assensi Oliva the head of the heat and mass transfer technological center CTTC for giving me the opportunity to do my doctoral program under his guidance and to learn from his research expertise. His personal support and great patience provided me with an excellent atmosphere for doing research work.

I would like also to thank Dr Ivette Rodríguez for her excellent guidance, patience, motivation, enthusiasm and immense knowledge. Her guidance helped me in all the time of the research and writing of this thesis, as well as, in developing my background in solar energy and fluid dynamics.

Moreover, I want to give my gratitude to Dr Roser Capdevila for her guidance and precious advices which resulted in increase of the quality of this thesis. Her expert knowledge in radiative heat transfer area and kind support have been essential for this work.

I extend my sincere thanks to all members of the CTTC center for their help and support whenever I was in need. I would thank also all my colleagues and friends for the great time that we have had in particular the CTTC football team.

I gratefully acknowledge the funding received towards of my PhD from the Spanish Agency for International Development Cooperation (AECID). I am also thankful to Prof Chiheb Bouden from the National Engineering School of Tunis for his recommendation to pursue my research in CTTC.

Finally, my most sincere and very heartfelt thanks to my Parents and Family who have been utmost supportive to me in my life and help me become today what I am.

Contents

Abstract

Concentrated Solar Power (CSP) technologies are gaining increasing interest in electricity generation due to the good potential for scaling up renewable energy at the utility level. Parabolic trough solar collector (PTC) is economically the most proven and advanced of the various CSP technologies. The modelling of these devices is a key aspect in the improvement of their design and performances which can represent a considerable increase of the overall efficiency of solar power plants. In the subject of modelling and improving the performances of PTCs and their heat collector elements (HCEs), the thermal, optical and aerodynamic study of the fluid flow and heat transfer is a powerful tool for optimising the solar field output and increase the solar plant performance. This thesis is focused on the implementation of a general methodology able to simulate the thermal, optical and aerodynamic behaviour of PTCs. The methodology followed for the thermal modelling of a PTC, taking into account the realistic non-uniform solar heat flux in the azimuthal direction is presented. Although ab initio, the finite volume method (FVM) for solving the radiative transfer equation was considered, it has been later discarded among other reasons due to its high computational cost and the unsuitability of the method for treating the finite angular size of the Sun. To overcome these issues, a new optical model has been proposed. The new model, which is based on both the FVM and ray tracing techniques, uses a numerical-geometrical approach for considering the optic cone. The effect of different factors, such as: incident angle, geometric concentration and rim angle, on the solar heat flux distribution is addressed. The accuracy of the new model is verified and better results than the Monte Carlo Ray Tracing (MCRT) model for the conditions under study are shown.

Furthermore, the thermal behaviour of the PTC taking into account the non-uniform distribution of solar flux in the azimuthal direction is analysed. A general performance model based on an energy balance about the HCE is developed. Heat losses and thermal performances are determined and validated with Sandia Laboratories tests. The similarity between the temperature profile of both absorber and glass envelope and the solar flux distribution is also shown.

In addition, the convection heat losses to the ambient and the effect of wind flow on the aerodynamic forces acting on the PTC structure are considered. To do this, detailed numerical simulations based on Large Eddy Simulations (LES) are carried out. Simulations are performed at two Reynolds numbers of $Re_{W1} = 3.6 \times 10^5$ and $Re_{W2} = 1 \times 10^6$. These values corresponds to working conditions similar to those encountered in solar power plants for an Eurotrough PTC. The study has also considered different pitch angles mimicking the actual conditions of the PTC tracking mechanism along the day. Aerodynamic loads, i.e. drag and lift coefficients, are calculated and validated with measurements performed in wind tunnels. The independence of the aerodynamic coefficients with Reynolds numbers in the studied range is shown. Regarding the convection heat transfer taking place around the receiver, averaged local Nusselt number for the different pitch angles and Reynolds numbers have been computed and the influence of the parabola in the heat losses has been analysed. Last but not the least, the detailed analysis of the unsteady forces acting on the PTC structure has been conducted by means of the power spectra of several probes. The analysis has led to detect an increase of instabilities when moving the PTC to intermediate pitch angles. At these positions, the shear-layers formed at the sharp corners of the parabola interact shedding vortices with a high level of coherence. The coherent turbulence produces vibrations and stresses on the PTC structure which increase with the Reynolds number and eventually, might lead to structural failure under certain conditions.

Chapter 1

Introduction

1.1 Solar concentrating technology

Solar radiation arriving at the Earth's surface is a fairly dispersed energy source. The photons comprising the solar radiation can be converted directly to electricity in photovoltaic devices, or, in concentrating solar power (CSP). In the latter case ,the solar radiation heats up a fluid that is used to drive a thermodynamic cycle. Opposed to photovoltaic cells or flat plate solar thermal collectors, the diffuse part of the solar irradiation which results from the scattering of the direct sunlight cannot be concentrated and can therefore not be used in CSP power plants. In the CSP technology, concentration of sunlight using mirrors or optical lenses is necessary to create a sufficiently high energy density and temperature level. Solar concentrating systems enable the thermal conversion to be carried out at high solar flux and with relatively little heat loss. Different solar concentrating technologies are today developed and demonstrated in solar market and can be divided according to the method of concentration [1] in two groups: line concentrating and point concentrating.

1.1.1 Line concentrating

Line concentration use a trough-like mirror to concentrate the incoming solar radiation onto an absorber tube by one-axis tracking system. The most important line concentrating technologies are the parabolic trough collectors (PTC) and linear Fresnel reflector systems (LF) (see figure 1.1).

Depending to their design, PTC and LF are able to concentrate the solar radiation flux $30 - 80$ times in order to heat a thermal fluid up to 400°C.

The absorber tube may be made by steel or cooper and coated with a heat resistant black paint. Parabolic trough is today considered a fully mature technology where technological and financial risks are expected to be low. The parabolic trough


(a) (b)

Figure 1.1: Line concentrating systems: (a) Parabolic trough collector: 50 MW power plant Andasol 1 in Granada, Spain [2] , (b) Linear Fresnel collector: 9 MW solar field at Liddell Power station, Australia [3]

collector consists of receiver, mirrors, metal support structure, pylons and foundations. The parabolic shaped and faceted mirrors concentrate the sunlight onto the receiver tube.

The absorber tube is typically surrounded by a glass tube creating a vacuum in the annular zone to reduce convective heat losses from the hot steel pipe. A selective coating with high solar absorptivity and low thermal emissivity may be used to reduce heat losses and achieve better performance. A thermal oil is commonly used as a working fluid that circulate through the absorber tube and transform the solar radiation into thermal energy and carries heat to heat exchangers or similar for driving a Rankine stream turbine. Other heat transfer fluids can be also used in PTC technology such as molten salt and steam.

Linear Fresnel collectors are a variation of parabolic trough collectors. The main difference compared to the parabolic trough collectors is that LFCs use several parallel mirrors facets instead of parabolic bent mirrors to concentrate the sunlight onto one receiver, which is located several meters above the primary mirror field [4]. The receiver also consists of a long selectively coated absorber tube without any need for flexible hoses or rotating connectors as it is the case for parabolic trough. Due to the optical principles of Fresnel collectors, the focal line is distorted by astigmatism [5]. This requires a secondary mirror above the tube in order to refocus the rays missing the tube in a secondary reflection onto the tube. Another concept is based on several parallel tubes forming a multi-tube receiver (increasing the width) instead of using a secondary reflector [6]. Compared to trough plants, commercial LFC technology is relatively novel.

(a) (b)

Figure 1.2: Point concentrating systems: (a) Central receiver system: Solar tower plants: PS10 (11MW) and PS20(20MW) a in Seville, Spain [7], (b) Dish Stirling prototype plants at Plataforma Solar de Almera, Spain [8]

1.1.2 Point concentrating

The other kind of concentrating devices focus the incident solar radiation onto a point. Dish/engine systems (DE) and central receiver systems (CRS) are the most known application for point concentrating technology (see figure 1.2).
DE use a parabolic dish to concentrate the incident direct radiation onto a receiver. DE are 3 D concentrators with high concentration ratios $(1000 - 4000)$. The parabolic dish must track the sun on two-axis tracking system to maintain the light convergence at its focal point. DE systems have modular collector and receiver and uses small autonomous generation of electricity such as Stirling engines or small gas turbine located at the focal point. The receiver absorbs the radiant solar energy converting it into thermal energy in a circulating fluid [1]. Two general schemes are possible for power conversion: thermal energy can be transported to a central power conversion or converted directly into electricity using an engine-generator mounted at near/at the focal point which is the most common way [4].
The CRS technology is more complex and incorporates a field of large reflecting mirrors known as heliostats that concentrate the solar energy on the receiver mounted at the top of a tower. The immense solar flux reflected towards the receiver yields high concentration ratios $(200 - 1500)$. Every heliostat is individually oriented to reflect incident solar radiation directly onto the receiver taking into account the shading with other heliostats. A fluid passes through the receiver to absorb the thermal energy for power production and storage. A diversity of thermal fluids are used in the CRS technology such as air, water/steam, molten salt, and liquid sodium. Although it is less mature than PTC, CRS is today a proven technology and CRS plants are

Figure 1.3: Parabolic trough power plants Andasol 1 (in front) and Andasol 2 (rear) in Spain with a capacity of 50 MW each and a storage size of 7.5 hours [2]

being implemented, either in the design or in the construction phase [9].

1.2 Parabolic trough technology

This section is related to components of PTC and their main features and applications. It also includes some existing application and the evolution of this technology throughout the history. As mentioned in the previous section, PTC is a focal line solar concentrating technology where thermal fluid passes through a receiver tube to absorb the concentrated solar energy reflected by parabolic trough-shaped mirrors.
PTC applications can be divided in two main groups depending on the temperature range. The first and most important application is the concentrated solar power (CSP) plants for electric generation where temperature are from 300 to 400 °C. The other group of applications requires temperature between 100 and 250 °C. The main applications of this range are the industrial process heat (IPH), low-temperature heat demand, space heating and swimming pool and heat-driven refrigeration and cooling. This thesis is concerned with the first kind of applications, i.e. CSP plants.
There are two ways to integrate a PTC solar field in a steam-turbine power plant:*i)* directly, i.e., generating steam in the solar field (Direct Steam Generation (DSG) technology), or *ii)* indirectly, by heating thermal oil in the solar field and using it to generate steam in a heat exchanger (Heat Transfer Fluid (HTF) technology).
The PTCs were initially developed for industrial process heat (IPH) applications [10]. In 1983, Southern California Edison (SCE) signed an agreement with Luz International Limited to purchase power from the Solar Electric Generating System (SEGS) I and II plants. In total, Luz built nine SEGS plants range in size from 14

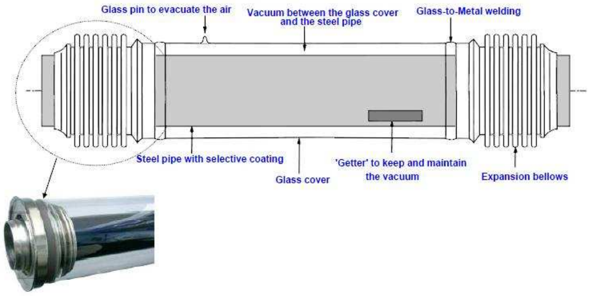

Figure 1.4: Typical receiver tube [11]

to 80 MWe and represent 354 MWe of installed electric generating system in the Mojave desert of California . The technology was also considerably stimulated in Europe when the first SEGS plants were erected. In 1996, the DIrect Solar Steam (DISS) project was initiated at the Plataforma Solar de Almería (PSA) to test parabolic trough collectors that generate steam directly in the solar field.

Recently, many research projects and solar plants are constructed or under construction in many countries.

1.2.1 Receiver tube

The receiver tube or heat collector element (HCE) is the main component of parabolic trough solar technology. It is composed of an inner steel tube with a selective coating surrounded by an anti-reflective evacuated glass tube. The HCE incorporates conventional glass-to-metal seals and metal bellows to ensure vacuum in annular zone and accommodate for thermal expansion difference between the steel and glass tubes. The vacuum in the HCE is typically maintained at about 0.013 Pa to reduce convection losses within the annulus. A typical selective coating used above the steel tube is the multilayer cermet coating which result in excellent selective optical properties with high solar absorptivity and low thermal emissivity. Receiver tube is generally about 4 m long between the support braces that support it at the focal line and can be extended to 150 m. The inner steel tube is about 70 mm outside diameter and the glass envelope tube is about 115 mm outside diameter [10]. An aluminium shield is usually used to protect welds and chemical getter (metallic compounds) are also placed in the vacuum space to eliminate gas molecules such as hydrogen that permeate into the vacuum annulus over time.

Figure 1.5: Structure and mirrors at a SEGS solar plant [12]

1.2.2 Structure and mirrors

PTC reflectors have a high specular reflectance (greater than 88%) to reflect as much solar radiation as possible. The reflectors are usually made from low-iron float glass (about $4mm$) with high solar transmittance. The mirrors are commonly silvered on the back and covered with several selective coatings since their durability and solar reflectance are better than the polished aluminium and metallized acrylic which are also available in the market. Solar reflectance is about 0.93 for silvered glass mirrors and 0.87 for polished aluminium [1]. The parabolic reflector is held by a steel support structure on pylons in the foundation. Ceramic pads used for mounting the mirrors to the collector structure are attached with a special adhesive. The installation and mounting of the support structure has high influence on the total plant performance. The support structure has to meet the following structural requirements:

- Stiffness: The structure has to be a robust, with a rigid frame, capable to maintain exact geometry (optical precision) at all times: It has to withstand deformations through the collector weight, through wind and through temperature differences of ambience and of the receiver.
- Weight: Low weight reduces cost of both material and transport.
- Motion: A high angular tolerance is necessary to enable one-axis tracking requirements. The tracking has to be accurate, robust and sufficiently strong to be capable to operate even under extreme weather conditions.

The metal support structure design is optimized to follow accuracy goals and to reduce investment cost. Several structural concepts of parabolic trough collectors exist.

One basic point where the concepts differ is how they transfer the torsional moment when tracking the Sun because high torsion would lead to a smaller intercept factor and lower optical efficiency. There are basically two concepts: the torque concept and the space frame concept.

1.2.3 Thermal fluid

Parabolic trough solar collectors utilize a heat transfer fluid (HTF) that flows through the receiver collecting and transporting solar thermal energy to the power block. The choice of the thermal fluid or heat transfer fluid (HTF) can effect the kind of storage technologies that can be used in the plant. Several HTF options may be used in PTC solar plants. The selection of the HTF is related to the required temperature and further options like storage. Thermal oils are commonly used as the working fluid in PTC plants for temperature above 200°C because the use of water can rise the price of the solar plant since it would produce high pressures inside the receiver tube and piping. Biphenyl-diphenyl-oxide, known by trade names Therminol VP-1 [13] and Dowtherm A [14], is widely used and has shown excellent stability. Although it is flammable, safety and environmental protection requirements can be satisfied with reasonable effort.

1.2.4 Thermal storage

Thermal storage is in principle applicable not only to parabolic trough power plants, but also to the other CSP technologies. However, most of the existing solar thermal power plants that have integrated thermal storage use PTC technology. The aim of the thermal storage system is to supply the steam turbine with the steam necessary for its operation when solar radiation is not available. In addition, during times of low irradiation, when solar energy alone is not sufficient, the system output can be increased by using additional steam generated by the storage system. Combined with thermal energy storage (TES), the CSP technology can provide not only dispatchable electricity but also stability to the electricity network in case of high fraction of renewable production or intermittency due to cloudy weather conditions.

Thermal energy storage can be classified by storage mechanism (sensible, latent, chemical) and by storage concept (active or passive) [16]. Different storage systems have been proposed in the literature: sensible heat storage both in solid media and liquid media; latent heat storage where the energy is stored through a phase change from a solid to liquid state; and chemical storage by reversing the direction of the endothermic chemical reactions. The sensible heat storage in liquid phase is considered the simplest and cheapest method which is the storage system most used in operational solar thermal power plants. Both oil and salts are possible candidate to the liquid media. Two main configurations are possible with these storage method: one

Figure 1.6: The two-tank storage system in the Andasol-1 plant [19]

or two-tank systems. In the first type, a one tank or thermocline is used as packed bed to store thermal energy. Because of density difference cold and hot fluid are separated: the hot fluid accumulated at the top and the cold is stratified at the bottom. Buoyancy forces help to maintain stable the thermal stratification in the same tank [17].

The two-tank system uses one tank for cold fluid coming from the steam generator and one tank for the hot fluid coming directly from the solar field before it is fed to the steam generator. The main advantage of this storage system is that cold and hot HTF are stored separately.

The state-of-the-art storage systems for PTC technology employ molten salts in an indirect two-tank design where the heat transfer occurs during charging and discharging process through forced convection [18].

1.2.5 Solar power cycle

PTC technology utilize usually a heat transfer fluid to collect heat energy based on a good solar-to-thermal efficiency which make possible to integrate this heat in a Rankine water/steam power cycle to produce electricity. If oil is used as a heat transfer fluid, it is heated in the solar field and goes on the steam generator which is an oil-water heat exchanger. Therefore, the oil transfers its thermal energy to the water in order to generate preheating and superheating steam required by the steam turbine. The steam generator is composed of three stages: preheater, evaporator and superheater where the water is transformed to a superheated steam [1]. The majority of power plants with PTC technology deployed to date use thermal oil as the working fluid in the solar field [20]. However, a number of alternative process concept are currently under development to reduce costs and increase efficiency. One of these initiative is the integration of a PTC field into the Rankine steam bottoming cycle of a combined gas-fired power plant. The concept is called Integrated Solar Combined-Cycle System (ISCCS) and it consists on over-sizing the steam turbine to handle the increased steam capacity. The ISCCS configuration is currently being considered and promoted in different power plants such as in India, Egypt, Morocco and Mexico [21]. The ISCCS concept is considered as an economic alternative because the incremental cost for increasing the steam turbine size on a combined-cycle plant is lower than a stand-alone Rankine cycle power plant. Another power concept is the use of direct steam generation (DSG) which refers to the generation of steam in the collector field and eliminates the need of an intermediate heat transfer fluid. The environmental risks associated with the oil would be then avoided. DSG concept reduces the overall plant investment cost because it eliminates the HTF steam generation and the associated element. However, it presents some challenges especially the two-phase flow existing in the absorber tube. PTCs can also be integrated in a geothermal power plant using Organic Rankine Cycle (ORC)[10]. Hot water and steam from geothermal wells can be directly fed into an absorber pipe going through a PTC field. The combination of both thermal energy sources increases the volume and the quality of generated steam for power production.

1.3 State-of-the-art of modelling PTC

Given the importance of the modelling of PTC, numerous models have been proposed to evaluate the optical, thermal and aerodynamic performance of the parabolic trough solar collectors. Different test cases have been studied in order to prove the accuracy of the implemented code and its applicability to solve the realistic non-uniform solar heat flux in the azimuthal direction. However, few published works have treated this dependence. Jeter [22, 23] presented a mathematical formulation based on the Gaussian function to calculate the concentrated solar flux density and the optical behaviour of a PTC taking into account imperfect reflection, transmission and absorption. Güven and Bannerot [24] established an optical model which used a ray-tracing technique to evaluate the optical performance and determined the optical errors by means of a statistical analysis. He et al. [25] combined the Monte Carlo ray-tracing method (MCRT) with a computational fluid dynamics (CFD) analysis in the HTF to simulate the coupled heat transfer problem. As for the thermal modelling of PTC, many works have been carried out to study the coupled heat transfer problem in the solar receiver assuming a uniform solar flux. Dudley et al. [26] proposed a one-dimensional (1D) model to analyse the thermal behaviour and performance of the LS2 SEGS collector. Foristall [27] implemented both a 1D and a two-dimensional model (2D) by dividing the absorber into several segments. A direct steam generation (DSG) collector model was proposed by Odeh et al. [28] based on the absorber wall temperature rather than the working fluid temperature. García-Valladares and Velázquez [29] proposed a numerical simulation of the optical, thermal and fluid dynamic behaviour of a single-pass solar PTC and extended the study by replacing the absorber with a counter-flow concentric circular heat exchangers (double-pass). Stuetzle [30] proposed a 2D unsteady state analysis of solar collector absorber to calculate the collector field outlet temperature: the model was solved by discretising the partial differential equations obtained by the energy balance. Padilla et al. [31] presented a 1D heat transfer model of a PTC taking into account the thermal interaction between adjacent surfaces and neglecting the non-uniformity of the solar flux. Roldán et al. [32] presented a CFD model to calculate the temperature profile in the wall of the absorber tubes of PTC for direct steam generation. They adopt a typical solar flux distribution around the receiver which is estimated by a square profile. Finally, only few studies of wind flow around the PTC have been published. In the late of 1970s and early 1980s, Sandia National Laboratories sponsored some wind tunnel tests, which were published in different reports [33, 34, 35, 36]. From March 2001 to August 2003, Hosoya et al. [37] conducted a series of wind tunnel tests about a PTC with different configurations in which they included the peak load and the local pressure across the face of the solar collector and, investigated the effect of the location of the PTC in the collector field, as well as, the use of a porous fence. Gong et al. [38] performed field measurements on the Yan Qing solar collector in China to determine the boundary layer wind characteristics and the effect of wind loads on solar collectors for different configurations. However the numerical study of wind flow around PTC are rare. Naeeni and Yaghoubi [39, 40] developed a turbulent model based on resolving the Reynolds-averaged Navier-Stokes equations (RANS) to analyse the fluid flow and heat transfer around a parabolic trough solar collector from Shiraz solar power plant.

1.4 Objectives of this thesis

The modelling of the HCE is a powerful tool to evaluate and improve the HCE designs and increase the performance of PTC solar plants. Several models have been proposed to analyse heat transfer about the HCE and develop parabolic trough receivers with higher performance[27]. However, as commented in the previous section, the majority of the thermal models are either unidimensional and too simplified or they neglect the realistic non-uniform solar heat flux in the azimuthal direction. The thermal and optical modelling of the HCE can be very useful for the evaluation of the performance of the solar receiver and improve the design.

Furthermore, the thermal and fluid dynamics study of the flow around the PTC and the HCE is very useful in order to predict the stability of the parabolic structure and mirrors against winds, as well as, the heat losses in the receiver [41]. Up to now, the turbulence modelling of the fluid flow and heat transfer around the PTC has been solved using RANS models which suffer from inaccuracies for the prediction of flows with massive separations and vortex shedding [42, 43]. However, the advances in computational fluid dynamics (CFD) together with the increasing capacity of parallel computers have made possible the use of more accurate turbulent models such as Large-Eddy Simulation models (LES) for solving industrial flows.

Considering the actual state-of-the-art in modelling parabolic trough solar collectors, this thesis aims at studying the fluid flow and heat transfer in a parabolic trough collector by means of detailed numerical models. To do this:

- A new optical model to accurately calculate the solar distribution around the HCE taking into account the solar angle has been implemented.
- A general thermal model that could predict accurately the heat losses and thermal performance of a PTC and takes into account the solar distribution around the HCEs has been developed.
- The wind flow around the PTC and its effect on the stability and the heat transfer around the HCE has been studied by means of three-dimensional simulations of the turbulent flow using Large-Eddy Simulations techniques.

1.5 Background

The present thesis has been developed at the Heat and Mass Transfer Technological Centre, (Centre Tecnológic de Transferéncia de Calor CTTC), of the Polytechnic University of Catalonia (Universitat Politècnica de Catalunya UPC-BarcelonaTech). CTTC is devoted to the mathematical formulation, numerical resolution and experimental validation of heat and mass transfer phenomena and, at the same time, the application of the acquired know-how to the design and optimisation of thermal systems and equipments. Within these research activities the Centre is working on: CFD & HT (which involves different issues such as high performance computing [44], turbulence modelling [45, 46], multi-phase modelling [47, 48], multi-physics modelling [49] , fluid structure interaction [50], wind energy [51], solar thermal energy, thermal and thermo-chemical storage [52], heat exchangers [53, 54], HVAC & Refrigeration [55, 56] and energy efficiency in building and/or districts [57]. A more extensive information about research activities (projects and publications) carried out within the fundamental working lines at CTTC can be found at [58].

Turbulence modelling has always been a challenging research topic with a wide experience in the centre. First turbulence modelling experiences were based on RANS for solving both natural convection and forced convection [59, 60, 61]. Furthermore, direct numerical simulations (DNS) for studying the natural convection inside a differential heat cavity [62] were also performed. Based on the acquired know-how in turbulence modelling and parallel computing, the experience was later extended to unstructured grids which has allowed to tackle turbulent flows with complex geometries by using both DNS and Large-Eddy Simulations (LES) [63, 64].

Furthermore, numerical simulation of energy transfer by radiation has been addressed in many works at CTTC. A significant experience has been acquired in the resolution of radiation in both, transparent and participating medium [65]. Net radiation Method was implemented for resolving radiation in transparent medium in axial symmetric geometries. Discrete ordinates method (DOM) was also used in Cartesian and cylindrical geometries to compute the radiation energy transfer within either transparent or participating media [66]. Another popular angular quadrature method, the finite volume method FVM, has been tested for the resolution of radiation transport problems [67]. Radiative transfer equation was solved within unstructured meshes for both quadrature methods (DOM and FVM) by means of parallel sweep method [68].

Besides, solar energy field constitutes one of the main applied research topics, with more than two decades of experience. CTTC research in this subject has covered a wide spectrum of applications such as passive solar energy systems [69, 70], low temperature solar systems and equipment [71, 72] and high temperature solar thermal power plants [73, 74, 75].

This thesis takes advantage of the previous experience in the different subjects to make one step forward in the modelling of solar thermal equipments, specially parabolic trough collectors for CSP plants. In addition, the accumulated knowledge in the resolution of the the radiative thermal equation and in particular to the finite volume method FVM, was the starting point for the optical modelling of the PTC (see chapter 2). Although, it has been shown that the FVM is costly expensive and less efficient for such applications, the experience gained in resolving energy transfer by radiation has allowed to develop a new optical model based on the FVM and ray tracing techniques. The new optical model is more suitable for such applications and takes into account the finite size of the Sun (see chapter 2). Apart form that, the previous experience in turbulence modelling and more specifically in the turbulent flow around bluff bodies [73, 76, 77, 78] has been very useful for the study of the fluid flow and heat transfer around the PTC (see chapters 4 and 5). The characteristics encountered in turbulent flows with massive separations were key factors to handle the aerodynamic behaviour of the PTC and its solar receiver. In this context, turbulence modelling in this thesis is carried out using the multi-physics software

Termofluids [45] developed by Termo Fluids S.L., a spin-off of the CTTC. This code has been programmed following the object oriented methodology and designed to run in parallel super computers. The main objective of this code is to contribute to solve complex multi-physics problems with high level methods including many functionalities such as: radiation, reactive flows, multiphase flows, fluid-structure interactions, problems with dynamic meshes and multi-scale systems.

1.6 Outline of the thesis

This thesis aims at modelling the fluid flow and heat transfer around a parabolic trough solar collector. In order to accomplish the goals detailed in section 1.4, the next chapter is devoted to present the optical model and the different steps in investigations that have been taken to develop a new optical model. This model is based on the finite volume method (FVM) and ray trace techniques and takes into account the finite size of the Sun in order to calculate accurately the non-uniform solar flux distribution around the receiver. The model has been validated respect to analytical and numerical results from the literature.

Chapter 3 is dedicated to present the details of the thermal model for simulation of PTC. This numerical heat transfer model is based on the finite volume method and it applies an energy balance about each components of the solar receiver. This model includes the direct normal solar irradiation, the optical losses from both, the parabola and the HCE, the thermal losses from the HCE, and the gains in the heat transfer fluid. The main contribution of this model is to take into account the realistic non-uniform solar heat flux in the azimuthal direction and its effect on the thermal behaviour of the components of the solar receiver.

After this chapter, the three-dimensional turbulent fluid flow and heat transfer around the PTC is studied. This model is based on Large Eddy Simulations to calculate the convection heat transfer from the receiver and the drag forces on the solar collector. First, it is verified on a circular cylinder in a cross flow and then validated with available experimental measurements from literature on solar collectors. Simulations are performed for various pitch angles and wind speeds and aerodynamic coefficients and heat transfer coefficients are calculated. A power spectra analysis is also conducted to study the unsteady forces acting on the PTC.

References

[1] F. Kreith and D.Y. Goswami. *Handbook of energy efficiency and renewable energy*. Taylor & Francis, 2007.

[2] Solar Millennium. Online technology information brochure. Available at: http://www.solarmillennium.de, date of laste visit: May2013.

[3] Novatec Solar. Online technology information brochure. Available at: http://www.novatecsolar.com/28-1-Press-Images.htm, date of laste visit: May2013.

[4] D. Barlev, R. Vidu, and P. Stroeve. Innovation in concentrated solar power. *Solar Energy Materials & Solar Cells*, 95(10):2703–2725, 2011.

[5] M. Mertins. *Technische und wirtschaftliche Analyse von horizontalen Fresnel-Kollektoren*. PhD thesis, Universität Karlsruhe (TH), 2009. http://digbib.ubka.uni-karlsruhe.de/volltexte/1000013884(accessed May 2013).

[6] D.R. Mills and G.L. Morrison. Compact linear fresnel reflector solar thermal powerplants. *Solar Energy*, 68:263–283, 2000.

[7] Abengoa Solar. Online technology information brochure. Available at: http://www.abengoasolar.com/web/es/galeria, date of laste visit: May2013.

[8] Deutsches Zentrum für Luft- und Raumfahrt / German Aerospace Center. Online technology information brochure. Available at: http://www.dlr.de/, date of laste visit: May2013.

[9] H.L. Zhang, J. Baeyens, J. Degrième, and G. Cacères. Concentrated solar power plants: Review and design methodology. *Renewable and Sustainable Energy Reviews*, 22:466–481, 2013.

[10] H. Price, E. Lüpfert, D. Kearney, E. Zarza, G. Cohen, R. Gee, and R. Mahoney. Advances in parabolic trough solar power technology. *Journal of Solar Energy Engineering*, 124(2):109–125, 2002.

[11] Plataforma Solar de Almeria (PSA). Online technology information brochure. Available at: http://www.psa.es/webesp/index.php, date of laste visit: May2013.

[12] F. Burkholder and C. Kutscher. Heat loss testing of Schoot's 2008 PTR70 parabolic trough receiver. Technical Report NREL/TP-550-45633, National Renewable Energy Laboratory, 2009.

[13] Solutia. Therminol vp-1 heat transfer fluid, solutia. *Technical Bulletin 7239115B , St Louis*, 1999. Available at : www.therminol.com.

[14] Dow. Dowtherm a-synthetic organic heat transfer fluid. *Product information No. 176-021463-1101, AMS*, 1999.

[15] R. Gabbrielli and C. Zamparelli. Optimal design of a molten salt thermal storage tank for parabolic trough solar power plants. *Journal of Solar Energy Engineering*, 131:041001–10, 2009.

[16] Pilkington Solar International GmbH. Survey of thermal strorage for parabolic trough power plants. Technical Report NREL/SR-550-27925, National Renewable Energy Laboratory, 2000.

[17] J.E. Pacheco, S.K. Showalter, and W.J. Kolb. Development of a molten-salt thermocline thermal storage system for parabolic trough plants. *Solar Energy*, 124: 153–159, 2002.

[18] S. Kuravi, J. Trahan, Y. Goswami, M.M. Rahman, and E.K. Stefanakos. Thermal energy storage technologies and systems for concentrating solar power plants. *Progress in Energy and Combustion Science*, 39:285–319, 2013.

[19] S. Relloso and E. Delgado. Experience with molten salt thermal storage in a commercial parabolic trough plant; Andasol 1 commissioning and operation. In *Proceedings of the 15 th International SolarPACES Symposium, Sept*, pages 14–18, 2009.

[20] Parabolic-trough solar collectors and their applications. *Renewable and Sustainable Energy Reviews*, 14:1695–1721, 2010.

[21] J. Dersch, M. Geyer, U. Hermann, S. Jones, B. Kelly, R. Kistner, W. Ortmanns, R. Pitz-Paal, and H. Price. Trough integration into power plants-a study on the performance and economy of integrated solar combined cycle systems. *Energy*, 29:947–959, 2004.

[22] M.S. Jeter. Analytical determination of the optical performance of parabolic trough collectors from design data. *Solar Energy*, 39(1):11–21, 1987.

[23] M.S. Jeter. Calculation of the concentrated flux density distribution in a parabolic trough collectors by a semifinite formulation. *Solar Energy*, 37(5):335–345, 1986.

[24] H.M. Güven and R.B. Bannerot. Derivation of universal error parameters for comprehensive optical analysis of parabolic troughs. *Journal of Solar Energy Engineering*, 108:275–281, 1986.

[25] Y-L. He, J. Xiao, Z-D. Cheng, and Y-B. Tao. A MCRT and FVM coupled simulation method for energy conversion process in parabolic trough solar collector. *Renewable Energy*, 36:976–985, 2011.

[26] V. Dudley, G. Kolb, M. Sloan, and D. Kearney. SEGS LS2 solar collector-test results. Technical report, Report of Sandia National Laboratories (SANDIA-94-1884), 1994.

[27] R. Foristall. Heat transfer analysis and modeling of aparabolic trough solar receiver implemented in engineering equation solver. Technical report, National Renewable Energy Laboratory(NREL), 2003.

[28] S. Odeh, G. Morrison, and M. Behnia. Modelling of parabolic trough direct steam generation solar collectors. *Solar energy*, 62(6):395–406, 1998.

[29] O. García-Valladares and N. Velázquez. Numerical simulation of parabolic trough solar collector: improvement using counter flow concentric circular heat exchangers. *International Journal of Heat and Mass Transfer*, 52(3):597–609, 2009.

[30] T. Stuetzle. Automatic control of the 30 MWe SEGS IV Parabolic trough plant. Master's thesis, University of Wisconsin-Madison, College of Engineering, 2002.

[31] R.V. Padilla, G. Demirkaya, D.Y. Goswami, E. Stefanakos, and M. Rahman. Heat transfer analysis of parabolic trough solar receiver. *Applied Energy*, 88(12):5097–5110, 2011.

[32] M.I. Roldán, L. Valenzuela, and E. Zarza. Thermal analysis of solar receiver pipes with superheated steam. *Applied Energy*, 103:73–84, 2013.

[33] J.A. Peterka and R.G. Derickson. Wind load design methods for ground-based heliostats and parabolic dish collectors. Technical Report SAND 92-7009, Sandia National Laboratories, 1992.

[34] J.A. Peterka, J.M. Sinou, and J.E. Cermak. Mean wind forces on parabolic-trough solar collectors. Technical Report SAND 80-7023, Sandia National Laboratories, 1980.

[35] D.E. Randall, D.D. McBride, and R.E. Tate. Steady-state wind loading on parabolic-trough solar collectors. Technical Report SAND 79-2134, Sandia National Laboratories, 1980.

[36] D.E. Randall, R.E. Tate, and D.A. Powers. Experimental results of pitching moment tests on parabolic-trough solar-collector array configurations. Technical Report SAND 82-1569, Sandia National Laboratories, 1982.

[37] N. Hosoya, J.A. Peterka, R.C. Gee, and D Kearney. Wind tunnel tests of parabolic trough solar collectors. Technical Report NREL/SR-550-32282, National Renewable Energy Laboratory, 2008.

[38] B. Gong, Z. Wang, Z. Li, J. Zhang, and X. Fu. Field measurements of boundary layer wind characteristics and wind loads of a parabolic trough solar collector. *Solar energy*, 86(6):1880–1898, 2012.

[39] N. Naeeni and M. Yaghoubi. Analysis of wind flow around a parabolic collector (1) fluid flow. *Renewable Energy*, 32(11):1898–1916, 2007.

[40] N. Naeeni and M. Yaghoubi. Analysis of wind flow around a parabolic collector (2) fluid flow. *Renewable Energy*, 32(11):1259–1272, 2007.

[41] L.M. Murphy. Wind loading on tracking and field mouted solar collectors. Technical Report SERI/TP-623-958, Solar Energy Research Institute, 1980.

[42] W. Rodi. Comparison of LES and RANS calculations of the flow around bluff bodies. *Journal of Wind Engineering and Industrial Aerodynamics*, 69:55–75, 1997.

[43] Z.T. Xie and I.P. Castro. LES and RANS for turbulent flow over arrays of wall-mounted cubes. *Flow Turbulence and Combustion*, 76(3):291–312, 2006.

[44] A.V. Gorobets, F.X. Trias, and A. Oliva. A parallel mpi+ openmp+ opencl algorithm for hybrid supercomputations of incompressible flows. *Computers & Fluids*, 2013. http://dx.doi.org/10.1016/j.comp¿uid.2013.05.021.

[45] O. Lehmkuhl, C. D. Pérez-Segarra, R. Borrell, M. Soria, and A. Oliva. TERMOFLUIDS: A new Parallel unstructured CFD code for the simulation of turbulent industrial problems on low cost PC Cluster. In I.H. Tuncer, Ü. Gülcat, D.R. Emerson, and K. Matsuno, editors, *Proceedings of the 2005 Parallel Computational Fluid Dynamics Conference*, volume 67 of *Lecture Notes in Computational Science and Engineering*, pages 275–282. Springer, 2007.

[46] O. Lehmkuhl, A. Baez, I. Rodríguez, and C.D. Pérez-Segara. Direct numerical simulation and large-eddy simultaions of the turbulent flow around a NACA-0012 airfoil. In *ICCHMT*, 2011.

[47] S. Morales-Ruiz, J. Rigola, I. Rodríguez, and A. Oliva. Numerical resolution of the liquid-vapour two-phase flow by means of the two-fluid model and a pressure based method. *Progress in Computational Fluid Dynamics, An International Journal*, 43:118–130, 2012.

[48] N. Balcázar, L. Jofre, O. Lehmkuhl, J. Castro, J. Rigola, and A. Oliva. A finite-volume/level-set interface capturing method for unstructured grids: Simulation of bubbles rising through viscous liquids. In *Proceedings of the 7th International Conference on Computational and Experimental Methods in Multiphase and Complex Flow*, 2013.

[49] H. Giràldez, C.D. Pérez Segarra, I. Rodríguez, and A. Oliva. Improved semi-analytical method for air curtains prediction. *Energy and Buildings*, 66:258–266, 2013.

[50] O. Estruch, O. Lehmkuhl, R. Borell, C.D. Pérez-Segarra, and A. Oliva. A parallel radial basis function interpolation method for unstructured dynamic meshes. *Computers & Fluids*, 80:44–54, 2013.

[51] J. Calafell, O. Lehmkuhl, I. Rodríguez, and A. Oliva. On the Large-Eddy Simulation modelling of wind turbine dedicated airfoils at high Reynolds numbers. In K. Hanjalić, Y. Nagano, D. Borello, and S. Jakirlic, editors, *Turbulence, Heat and Mass Transfer*, volume 7, pages 1–12, Palermo, Italy, 2012. Begell House, Inc.

[52] P.A. Galione, O. Lehmkuhl, J. Rigola, A. Oliva, and I. Rodriíguez. Numerical simulations of energy storage with encapsulated phase change materials. special emphasis on solid-liquid phase change CFD modelling. In *12th International Conference on Energy Storage INNOSTOCK*, Lleida, Spain, 2012.

[53] C. Oliet, C.D. Pérez-Segarra, J. Castro, and A. Oliva. Modelling of fin-and-tube evaporators considering non-uniform in-tube heat transfer. *International Journal of Thermal Sciences*, 49(4):692–701, 2010.

[54] S. Danovand, Pérez-Segarra, C.D., C. Oliet, and A. Oliva. Experimental facility for the study of liquid overfeed fin-and-tube evaporators. validation of numerical models. *International Journal of Heat Ventilation Air Conditioning and Refrigeration Research*, 14(2):221–239, 2008.

[55] J. Jaramillo, C.D. Pérez-Segarra, O. Lehmkuhl, and J. Castro. Detailed analysis of turbulent flows in air curtains. *Progress in Computational Fluid Dynamics, An International Journal*, 11(6):350–362, 2011.

[56] J. López-Mas, O. Lehmkuhl, J. Rigola, and C.D. Pérez-Segarra. Use of a low-mach model on a CFD & HT solver for the elements of an object oriented program to numerically simulate hermetic refrigeration compressors. In *International Compressor Engineering Conference*, Purdue, USA, 2012.

[57] D. Damle, O. Lehmkuhl, G. Colomer, and I. Rodríguez. Energy simulation of buildings with a modular object-oriented tool. In *Proceedings of ISES Solar World Congress*, Kassel, Germany, 2011.

[58] http:/www.cttc.upc.edu/.

[59] J. Jaramillo, C.D. Pérez-Segarra, I. Rodríguez, and A. Oliva. Numerical study of plane and round impinging jets using rans models. *Numerical Heat Transfer*, 54 (3):251–275, 2008.

[60] J.E. Jaramillo. *Suitability of Different RANS Models in the Description of Turbulent Forced Convection Flows. Application to Air Curtains.* PhD thesis, Universitat Politècnica de Catalunuya, 2008.

[61] X. Albets. *Numerical Studies of Natural and Forced Convective Heat Transfer Processes Using Two-Equation Turbulence Models.* PhD thesis, Universitat Politècnica de Catalunuya, 2006.

[62] F.X. Trias, M. Soria, C.D. Pérez-Segarra, and A. Oliva. A direct schur-fourier decomposition for the efficient solution of high-order poisson equations on loosely coupled parallel computer. *Numerical Linear Algebra with Applications*, 13:303–326, 2006.

[63] J. Jaramillo, F.X. Trias, C.D. Pérez-Segarra, and A. Oliva. Dns and rans modelling of a turbulent plane impinging jet. *International Journal of Heat and Mass Transfer*, 55(4):789–801, 2012.

[64] I. Rodríguez, O. Lehmkuhl, R. Borell, and C.D. Pérez-Segarra. On DNS and LES of natural convection of wall-confined flows: Rayleigh-bernard convection. In Springer Netherlands, editor, *In Direct and Large-Eddy Simulation VIII*, pages 389–394, 2011.

[65] G. Colomer. *Numerical methods for radiative heat transfer*. PhD thesis, Universitat Politècnica de Catalunuya, 2006.

[66] G. Colomer, M. Costa, R. Cònsul, and A. Oliva. Three dimensional numerical simulation of convection and radiation in a differential heated cavity using the discrete ordinates method. *International Journal of Heat and Mass Transfer*, 47(2): 257–269, 2004.

[67] R. Capdevila. *Numerical simulation of radiative heat transfer in turbulent flows*. PhD thesis, Universitat Politècnica de Catalunuya, 2012.

[68] G. Colomer, R. Borrell, F. X. Trias, and I. Rodrǵuez. Parallel algorithms for sn transport sweeps on unstructured meshes. *Journal of Computational Physics*, 232 (1):118–135, 2013.

[69] D. Faggembauu, M. Costa, M. Soria, , and A. Oliva. Numerical analysis of the thermal behaviour of glazed ventilated facades in mediterranean climates. part i: Development and validation of a numerical model. *Solar Energy*, 75(3):217–228, 2003.

[70] D. Faggembauu, M. Costa, M. Soria, , and A. Oliva. Numerical analysis of the thermal behaviour of glazed ventilated facades in mediterranean climates. part ii: Applications and analysis of results. *Solar Energy*, 75(3):229–239, 2003.

[71] I. Rodríguez. *Unsteady laminar convection in cylindrical domains: numerical studies and application to solar water storage tanks*. PhD thesis, Universitat Politècnica de Catalunuya, 2006.

[72] H. Kessentini, R. Capdevila, O. Lehmkuhl, J. Castro, and A. Oliva. Numerical simulation of heat transfer and fluid flow in a flat plate solar collector with tim and ventilation channel. In *Proceedings of Eurosun conference*, Rijeka, Croatia, 2012.

[73] I. Rodríguez, C.D. Pérez-Segarra, O. Lehmkuhl, and A. Oliva. Modular object-oriented methodology for the resolution of molten salt storage tanks for csp plants. *Applied Energy*, 109:402–414, 2013.

[74] J. Chiva, O. Lehmkuhl, M. Soria, and A. Oliva. Modelization of heat transfer and fluid dynamics in solar power towers. In *Proceedings of ISES Solar World Congress*, Kassel, Germany, 2011.

[75] G. Colomer, J. Chiva, O. Lehmkuhl, and A. Oliva. Advanced CFD & HT numerical modelling of solar receivers. In *SolarPACES conference*, Las Vegas, USA, 2013.

[76] O. Lehmkuhl, I. Rodríguez, R. Borrell, and A. Oliva. Low-frequency unsteadiness in the vortex formation region of a circular cylinder. *Physics of Fluids*, 25 (085109), 2013. doi:10.1063/1.4818641.

[77] D. Aljure, I. Rodríguez, O. Lehmkhul, R. Borrell, and A. Oliva. Flow and turbulent structures around simplified cars models. In *Conference on Modelling Fluid Flow (CMFF'12)*, pages 247–254, Budapest, Hungary, 2012.

[78] O. Lehmkuhl, I. Rodríguez, A. Baez, A. Oliva, and C.D. Pérez-Segarra. On the large-eddy simulations for the flow around aerodynamic profiles using unstructured grids. *Computers & Fluids*, 84:176–189, 2013.

Chapter 2

Radiative analysis and optical model of a PTC

Part of the contents of this chapter have been published as:

A.A. Hachicha, I. Rodríguez, R. Capdevila and A. Oliva. Numerical simulation of a parabolic trough solar collector considering the concentrated energy flux distribution. *30th ISES Biennial Solar World Congress 2011, SWC 2011*, (5)3976-3987.

A.A. Hachicha, I. Rodríguez, R. Capdevila and A. Oliva. Heat transfer analysis and numerical simulation of a parabolic trough solar collector . *Applied Energy* 2013; 111: 582-592.

Abstract. The finite volume method for solving the radiative transfer equation (RTE) has been implemented and tested for different cases including transparent, absorbing, emitting and isotropically scattering media in enclosures. The same methodology is applied to determine the solar heat flux distribution around the absorber tube of a parabolic trough solar collector (PTC). In order to reduce the computational cost and take into account the finite size of the Sun, a new geometrical-numerical method inspired from the FVM and ray tracing techniques has been developed to analyse the optical performances of a PTC. The new optical has been validated with available analytical and numerical data from the literature and a good agreement is encountered. The effect of different factors, such as: incident angle, geometric concentration and rim angle on the solar heat flux distribution has also been studied.

2.1 Introduction

The optical modelling of a parabolic trough solar collector (PTC) is very useful to determine the azimuthal distribution of the non-uniform solar flux around the receiver as well as its optical performance. The optical model is a pre-processing task that should be included into the thermal model as a boundary condition for the outer surfaces of the absorber/glass tube. One of the main approaches to develop a numerical optical model is the resolution of the radiative transfer equation (RTE). With the development of computers, different numerical methods to solve the RTE were formulated. Among the existing methods to solve the RTE, the finite volume method (FVM) proposed by Raithby and Chui [1] is one of the most popular ones used in CFD that is capable of handling radiation in transparent and participating gray medium. It has been extensively applied at different situations because it leads to the exact satisfaction of the conservation laws.

First, several benchmark and preliminary cases are solved using the FVM in order to prove the accuracy of the model. This method is then implemented and applied at a PTC and its receiver. However, the difficulties encountered to simulate the finite size of the Sun together with the high computational costs were the main motivations to develop a new geometrical-numerical method inspired by the FVM and ray tracing techniques. The new optical model takes into account the finite size of the Sun and the incident angle. Numerical results are performed for different configurations and then compared to analytical and numerical results available in the literature.

2.2 Radiative Transfer Equation (RTE)

In many engineering applications, the interaction between absorbing, emitting and scattering in a participating medium must be accounted for. This can be modelled using a balance of energy, known as Radiative Transfer Equation (RTE), which describes the radiative intensity field as a function of location (fixed by location vector r), direction (fixed by unit direction vector $\hat{s}$) and spectral variable (wavenumber ν). Consider a beam of radiation with intensity $I_\nu(r, \hat{s})$ propagating in the absorbing, emitting and scattering medium in a given direction. The energy of radiation will decrease owing to its absorption by the medium and owing to the deviation of a part of the radiation from the initial trajectory as a result of the scattering in all directions (out-scattering). But, at the same time, the energy will increase because of thermal radiation emission by the medium volume and by the incoming scattering from other directions (in-scattering). The absorption, scattering and emission of radiation by a medium have effect on the energy of a radiation beam that propagates in it.

Consider the emitting, absorbing and scattering medium characterized by the spectral absorption coefficient κ_ν and spectral scattering coefficient $\sigma_{s,\nu}$. The beam of monochromatic radiation with intensity $I_\nu(r,\hat{s})$ propagates in this medium in the observation direction Ω along the path s. The radiative balance is applied on an elementary volume in the form of a cylinder with cross section dA, length dS, disposed in the vicinity of coordinate s, the axis of a cylinder coinciding with the direction of s (see figure2.1).

Let $I_\nu(r,s,\hat{s},t)$ be the radiation intensity at point s for the time t and $I_\nu(r,s+dS,\hat{s},t+dt)$ be the radiation intensity at point $s+dS$ for the time $t+dt$ in the vicinity of t. The change in radiative intensity in the path length dS is obtained by taking into account the augmentation by emission and in-scattering and the reduction by absorption and out-scattering.

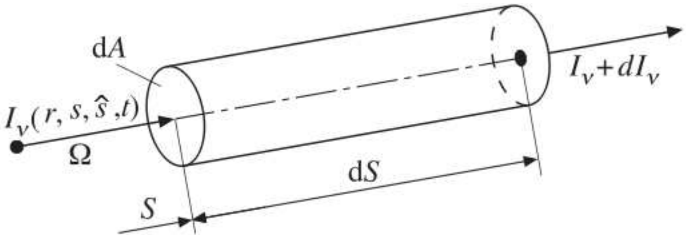

Figure 2.1: An elementary volume for the derivation of the RTE.

The energy balance of the radiative energy gives

$$\begin{aligned}(I_\nu(r,s+dS,\hat{s},t+dt)-I_\nu(r,s,\hat{s},t))dA &= \kappa_\nu I_{b\nu}(r,s,t)dAdS-\kappa_\nu I_\nu(r,s,t)dAdS\\ &-\sigma_{s,\nu}I_\nu(r,s,\hat{s},t)dAdS+\tfrac{\sigma_{s,\nu}}{4\pi}\textstyle\int_{4\pi}I_\nu(r,\hat{s})\phi_\nu(\hat{s},\hat{s}')d\Omega dAdS \qquad (2.1)\end{aligned}$$

Since the ray travels at the speed of light, this control volume and the speed of light is so large compared to characteristic time of the majority of engineering problems [2], the general equation of transfer for an absorbing, emitting and scattering medium is

$$\frac{dI_\nu}{dS}=\hat{s}.\nabla I_\nu(r,\hat{s})=\kappa(r)_\nu I_{b\nu}(r)-\beta(r)I_\nu(r,\hat{s})+\frac{\sigma_{s,\nu}(r)}{4\pi}\int_{4\pi}I_\nu(\hat{s})\Phi_\nu(\hat{s},\hat{s}')d\Omega \qquad (2.2)$$

Most frequently this equation is presented in a more compact form:

$$\frac{dI_\nu(r,\hat{s})}{dS}=-\beta_\nu I_\nu(r,\hat{s})+S_\nu(r,\hat{s}) \qquad (2.3)$$

where

$$\beta_\nu=\kappa_\nu+\sigma_{s,\nu} \qquad (2.4)$$

$$S_\nu(r,\hat{s}) = \kappa(r)_\nu I_b(r) + \frac{\sigma_{s,\nu}(r)}{4\pi}\int_{4\pi} I_\nu(\hat{s})\Phi_\nu(\hat{s},\hat{s}')d\Omega \tag{2.5}$$

In these relations, S_ν is called the source function, β_ν is the spectral extinction coefficient. Equation (2.2) is valid for a gray medium or, in spectral basis, for a nongray medium. By assuming the medium is gray, I_ν becomes I.

In the present work, two different boundary conditions are used. The boundary condition of radiative intensity for an opaque diffuse surface is given by the following equation.

$$I(r_w,\hat{s}) = \epsilon(r_w)I_b(r_w) + \frac{\rho(r_w)}{\pi}\int_{\hat{n}\cdot\hat{s}'<0} I(r_w,\hat{s'})|\hat{n}\cdot\hat{s}'|d\Omega' \tag{2.6}$$

For diffusely emitting, specularly reflecting opaque surfaces the boundary condition is described by

$$I(r_w,\hat{s}) = \epsilon(r_w)I_b(r_w) + \frac{\rho_d(r_w)}{\pi}\int_{\hat{n}\cdot\hat{s'}<0} I(r_w,\hat{s'})|\hat{n}\cdot\hat{s'}|d\Omega' + \rho_s(r_w)\pi I(r_w,\hat{s_s}) \tag{2.7}$$

where ρ_d, ρ_s and s_s are the diffuse reflectivity, the specular reflectivity and the specular direction, respectively.

The radiative flux is defined by the following equation

$$q(r) = \int_{4\pi} I(r,\hat{s})\hat{s}d\Omega \tag{2.8}$$

The divergence of the heat flux can be calculated by integrating the RTE over all solid angles

$$\int_{4\pi}\hat{s}\cdot\nabla I(r,\hat{s})d\Omega = \int_{4\pi}\kappa(r)I_b(r)d\Omega - \int_{4\pi}\beta(r)I(r,\hat{s})d\Omega + \int_{4\pi}\frac{\sigma_s(r)}{4\pi}\int_{4\pi}I(r,\hat{s})\Phi(\hat{s},\hat{s}')d\Omega d\Omega' \tag{2.9}$$

where Φ is the scattering phase function and $\Phi = 1$ for isotropic scattering. The scattering function obeys the following relation

$$\int_{4\pi}\Phi(\hat{s},\hat{s}')d\Omega = 4\pi \tag{2.10}$$

Scattering is only a redistribution phenomena of the photons without changing its energy.

Then, the last integration leads to

$$\nabla\cdot q = 4\pi\kappa(r)I_b(r) - \beta(r)\int_{4\pi}I(r,\hat{s})d\Omega + \sigma_s(r)\int_{4\pi}I(r,\hat{s})d\Omega \tag{2.11}$$

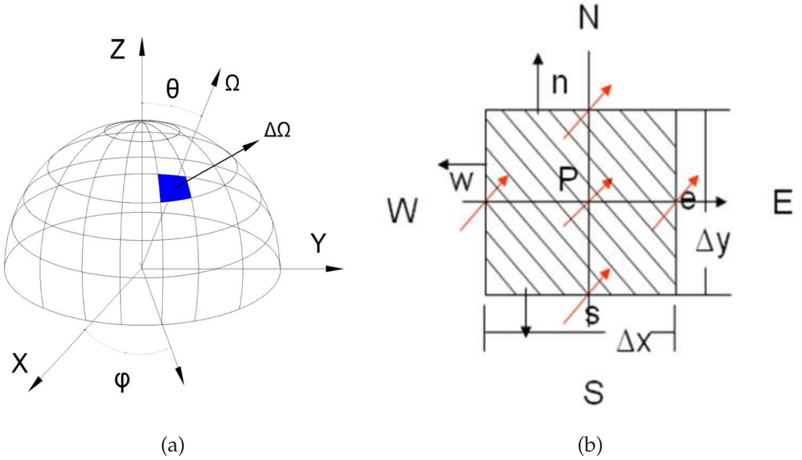

(a) (b)

Figure 2.2: Example of (a) angular discretisation (control angle) and (b) spatial discretisation (control volume).

Using the relation $\kappa = \beta - \sigma$ the divergence of the heat flux can be expressed as

$$\nabla \cdot q = \kappa(r)\left(4\pi I_b(r) - \int_{4\pi} I(r,\hat{s})d\Omega\right) \tag{2.12}$$

2.2.1 The Finite Volume Method (FVM)

Many methods have been developed to solve the RTE. Raithby and Chui [1, 3, 4] presented new angular and spatial discretisation practices that integrates the RTE on control angles as well as on control volumes to assure energy conservation. An exact integration is applied to evaluate solid angle integrals which is analogous to the evaluation of areas and volumes in the finite volume approach. The FVM permits also to capture the collimated directions without constraint and handle the specular reflection boundaries by using symmetric angular discretisation.

Following the spatial discretisation practice, the angular space is subdivided into $N_\theta \times N_\phi = M$ control angles (see figure 2.2(a)). The RTE is then, integrated over the control volume ΔV and over each of the solid angle elements $\Delta\Omega$.

Integrating RTE equation (2.3) over a typical two dimensional control volume and control angle $\Delta\Omega$ and applying the divergence theorem in a surface integral ΔA gives

$$\int_{\Delta\Omega^l}\int_{\Delta A} I^l(\hat{s}^l,\hat{n})dAd\Omega^l = \int_{\Delta\Omega^l}\int_{\Delta V}(-\beta I^l + S^l)dVd\Omega^l \tag{2.13}$$

where $\hat{s}^l$ is a unit direction vector in the control angle l. Applying the finite volume approach, the intensity is assumed constant within the control volume and the control angle then equation (2.13) can be simplified to

$$\sum_{i=1}^{4} I_i^l \Delta A \int_{\Delta\Omega^l}(\hat{s}^l,\hat{n})d\Omega^l = (-\beta I^l + S^l)\Delta V \Delta\Omega^l \tag{2.14}$$

where

$$S^l = \kappa I_b + \frac{\sigma}{4\pi}\sum_{l'=1}^{M}(I^{l'}\Phi^{ll'}\Delta\Omega^{l'}) \tag{2.15}$$

$\Phi^{ll'}$ is the phase function for scattering from the solid angle Ω^l to the solid angle $\Omega^{l'}$. In order to accelerate the iterative solution procedure, the treatment presented by Chai et al. [5], where a modified extinction coefficient and a modified source function are defined, is adopted.

$$\beta_m = \beta - \frac{\sigma}{4\pi}\Phi^{ll}\Delta\Omega^l \tag{2.16}$$

$$S_m^l = \kappa I_b + \frac{\sigma}{4\pi}\sum_{l'=1, l\neq l'}^{M} I^{l'}\Phi^{l'l}\Delta\Omega^{l'} \tag{2.17}$$

If equation (2.13) is discretised for a typical two-dimensional Cartesian coordinates control volume and radiation direction (see figure 2.2(b)). The discretised RTE takes the form

$$(I_e^l - I_w^l)\Delta A_x D_{cx}^l + (I_n^l - I_s^l)\Delta A_y D_{cy}^l = [-\beta_m^l I_P^l + S_m^l]\Delta V \Delta\Omega^l \tag{2.18}$$

where

$$D_{cx}^l = \int_{\Delta\Omega^l}(\hat{s}\cdot\hat{n}_x)d\Omega^l, \quad D_{cy}^l = \int_{\Delta\Omega^l}(\hat{s}\cdot\hat{n}_y)d\Omega^l \tag{2.19}$$

$$\Delta A_x = \Delta y, \qquad \Delta A_y = \Delta x \tag{2.20}$$

$$\Delta V = \Delta x \Delta y, \qquad \Delta\Omega^l = \int_{\phi^{l-}}^{\phi^{l+}}\int_{\theta^{l-}}^{\theta^{l+}} sin\theta d\theta d\phi \tag{2.21}$$

For example, for a direction that lies on the first quadrant ($0 < \theta < \pi/2$ and $0 < \phi < \pi$) like in figure 2.2(b), the intensities I_n^l and I_e^l are related with I_s^l and I_w^l, respectively through:

$$I_P^l = wI_n^l + (1-w)I_s^l = wI_e^l + (1-w)I_w^l \tag{2.22}$$

where w is an appropriate spatial weighting factor which defines the numerical scheme to evaluate the downstream boundary intensity. The weighting factors for diamond and step schemes are $w = 0.5$ and 1, respectively. The step scheme, which is the analogous of upwind scheme in the CFD community, is the simplest differencing scheme which sets the downstream boundary intensities equal to the upstream nodal intensities; i.e. $I_n^l = I_e^l = I_P^l$, $I_w^l = I_W^l$ and $I_s^l = I_S^l$. In the diamond scheme, the interpolation factor is set to 0.5, however this may lead to physically unreal negative intensities. In the present work negative intensities are set to zero following Clarson and Lathrop suggestion [6].

After applying equation (2.22) in equation 2.18 leads to the final expression of nodal intensity

$$I_P^l = \frac{\Delta y D_{cx}^l I_w^l + \Delta x D_{cy}^l I_s^l + w(S_m^l)_P \Delta V \Delta\Omega^l}{\Delta y D_{cx}^l + \Delta x D_{cy}^l + w(\beta_m^l)_P \Delta V \Delta\Omega^l} \tag{2.23}$$

The solution process is initialized with guessed values in the inner domain and the boundary conditions (in the case of gray walls) for any point in the boundaries and for all directions pointing away from the surface. For a 2 D Cartesian mesh, the control angles are divided into 4 quadrants taking into account the direction of the beam: the lower left corner is chosen as a starting point for those directions that lie in $(0 \leq \theta \leq \frac{\pi}{2})$ and $(0 \leq \phi \leq \pi)$. The source terms S_m are estimated by equation (2.17) and the values of the west and south intensities are known from the boundary conditions. Given the boundary values along the left and south faces, nodal values are found by direct substitution into equation (2.23). Once I_P^l has been calculated, I_e^l and I_n^l are determined from equation (2.22), thus the first quadrant intensities are calculated for the remaining control volumes of all the domain (I_E, I_W... and so on). The procedure is then repeated three times, starting from the remaining three corners of the enclosure and using the corresponding directions. After a pass over all directions and all the volumes, the whole process is repeated until convergence of the intensities.

The FVM can suffer from some shortcomings. Some are crucial to the solution accuracy, while others affect the efficiency of the solution procedure. Two major shortcomings of the FVM : ray effect and false scattering.

Ray effect is due to the discretisation of the angular variable: it arises from the approximation of a continuously varying angular nature of radiation by considering a specified set of discrete angular directions [7] which may give a wavy solution. This effect can be reduced by means of using finer angular discretisations [8].

False scattering arises from the spatial discretisation practice. It is nonphysical and thus could also be called numerical scattering. This effect is known as false diffusion in the Computational Fluid Dynamic (CFD) community. This is due essentially to the fact that the beam is oblique to the grid lines [7] which lead to a smeared solution. This effect can be reduced by refining the spatial grid or using more accurate spatial discretisation schemes.

Both shortcomings arise independently one from each other. However, there is an interaction between them [7, 9] because their effects tend to compensate each other. Ray effect tend to make the heat flux on a surface stepwise and the false scattering tend to smooth the steps. This compensation effect should not be relied on since no shortcoming is eliminated and should be reduced separately.

2.2.2 Collimated irradiation

If collimated irradiation that penetrates from the outside into a participating medium is considered, the RTE remains the same as equation (2.2).

$$\hat{s}.\nabla I(r,\hat{s}) = \kappa(r) I_b(r) - \beta(r) I(r,\hat{s}) + \frac{\sigma_s(r)}{4\pi}\int_{4\pi} I(\hat{s})\Phi(\hat{s},\hat{s}')d\Omega \tag{2.24}$$

However, intensity $I(r,\hat{s})$ within the medium is in this case composed of two components: *i)* the remnant of the collimated beam $I_c(r,\hat{s})$ after partial extinction by absorption and scattering along its path and *ii)* a diffuse part $I_d(r,\hat{s})$ which results from the emission from the boundaries, emission from within the medium and the radiation scattered away from the collimated irradiation. Thus,

$$I(r,\hat{s}) = I_c(r,\hat{s}) + I_d(r,\hat{s}) \tag{2.25}$$

where the collimated remnant of the irradiation obeys the equation of transfer

$$\hat{s}.\nabla I_c(r,\hat{s}) = -\beta I_c(r,\hat{s}) \tag{2.26}$$

This equation has the following solution

$$I_c(r,\hat{s}) = [1-\rho(r_w)]q_0(r_w)\delta[\hat{s}(r_w) - \hat{s_c}(r_w)]e^{-\tau_c} \tag{2.27}$$

where ρ is the reflectivity, q_0 is the collimated radiative flux incident on the boundary, δ is the Dirac delta function and τ_c is the optical depth in the direction of the collimated radiation defined as : $\tau_c = \int_0^s \beta ds'$.

Substituting equations (2.25) and (2.26) into equation (2.24), the RTE becomes

$$\hat{s}.\nabla I_d(r,\hat{s}) = \kappa(r) I_b(r) - \beta(r) I_d(r,\hat{s}) + \frac{\sigma_s(r)}{4\pi}\int_{4\pi} I_d(\hat{s})\Phi(\hat{s},\hat{s}')d\Omega + S_c(r,\hat{s}) \tag{2.28}$$

where $S_c(r,\hat{s})$ is the collimated source term resulting from radiation scattered away from the collimated beam and given by

$$S_c(r,\hat{s}) = \frac{\sigma_s(r)}{4\pi}\int_{4\pi} I_c(\hat{s})\Phi(\hat{s},\hat{s}')d\Omega = \frac{\sigma_s(r)}{4\pi}[1-\rho(r_w)]q_0(r_w)e^{-\tau_c}\Phi(\hat{s},\hat{s_c}) \tag{2.29}$$

For a diffusely emitting and reflecting boundaries the intensity for any location r_w on the surface is described as

$$I(r_w,\hat{s}) = [1-\rho(r_w)]I_{0w}(r_w,\hat{s})+\epsilon(r_w)I_b(r_w)+\frac{\rho(r_w)}{\pi}\int_{\hat{n}\cdot\hat{s'}<0} I(r_w,\hat{s'})|\hat{n}\cdot\hat{s'}|d\Omega' \tag{2.30}$$

2.3 Case studies

In order to test the accuracy of the implemented code, several test cases are solved using the FVM and compared with benchmark results found in the literature. The FVM has been applied to two dimensional radiative heat transfer in rectangular enclosures with isothermal diffusely reflecting, gray walls. The enclosed medium is also assumed to be gray and scatter isotropically in the case of scattering medium. The following notation $(N_x \times N_y)(N_\theta \times N_\phi)$ is considered to design the spatial and angular discretisations for the two dimensional cases.

2.3.1 Isothermal absorbing-emitting medium

The problem consists of a square enclosure with cold walls (at 0 K) which contains an absorbing emitting medium at uniform temperature T_g. The gas in the enclosure does not scatter ($\sigma_s = 0$) but emits and absorbs ($\kappa \neq 0$). In this case the medium

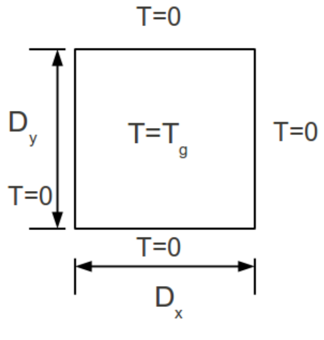

Figure 2.3: Schematic of the case 2.3.1.

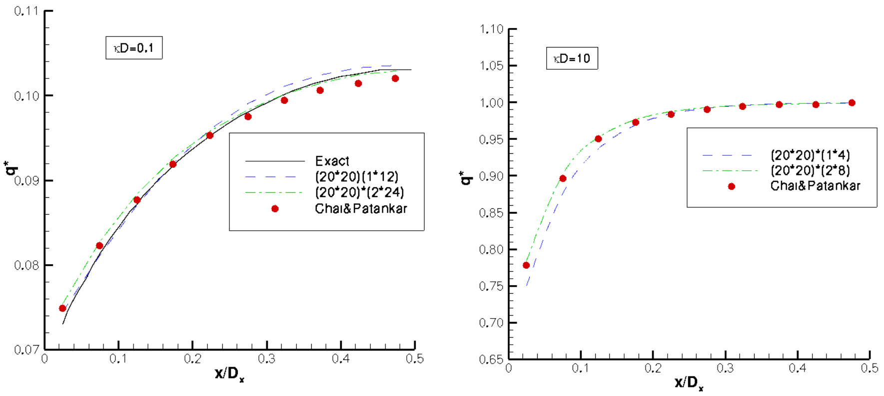

(a)

(b)

Figure 2.4: Case 2.3.1 dimensionless heat flux along the bottom wall for: (a) $\kappa D = 0.1$ and (b) $\kappa D = 10$

is supposed homogeneous and isothermal at uniform temperature T_g. The exact solution was taken from the results presented by Raithby and Chui [1].

The dimensionless heat flux on the bottom wall ($q* = \frac{q}{\sigma T_g^4}$) has been calculated for two optical thicknesses: $\kappa D_x = \kappa D_y = 0.1$ and $\kappa D_x = \kappa D_y = 10$ and compared with Chai and Patankar's [10] solutions (see figures 2.4(a) and 2.4(b)).

The domain is discretised into (20×20) uniform control volumes in the x and y directions, respectively. For the strongly absorbing-emitting/participating medium $\kappa D_x = \kappa D_y = 10$, two angular discretisations are used: (1×4) and (2×8) control angles with uniform $\Delta\theta$ and $\Delta\phi$ in the θ and ϕ directions, respectively. For the weakly emitted medium $\kappa D_x = \kappa D_y = 0.1$, two angular discretisations are used (1×12) and (2×24) control angles. These are the same control angles used by Chai and Patankar [10].

The results obtained using the step scheme (see figures 2.4(a) and 2.4(b)) give a good agreement with those found by Chai and Patankar [10] even for the coarse angular grids. By refining the angular discretisation, the solution of the FVM converges to the exact solution.

2.3.2 Purely scattering medium

The problem consists of a rectangular enclosure with the left, top and right wall temperatures set to $T_c = 0$ K and the bottom wall set at higher temperature, T_h

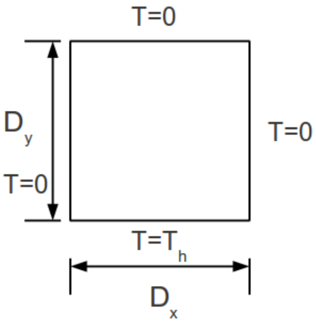

Figure 2.5: Schematic of the case 2.3.2.

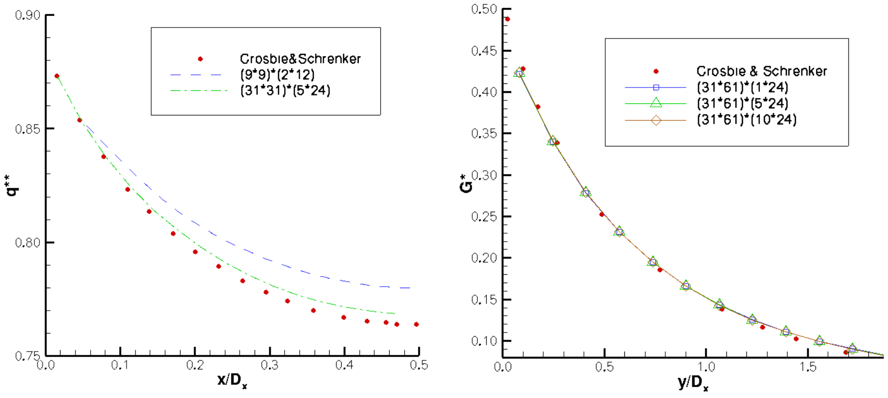

(a) (b)

Figure 2.6: Case 2.3.2 dimensionless: (a) heat flux for $D_y/D_x = 1$ and (b) centreline average incident radiation for $D_y/D_x = 10$.

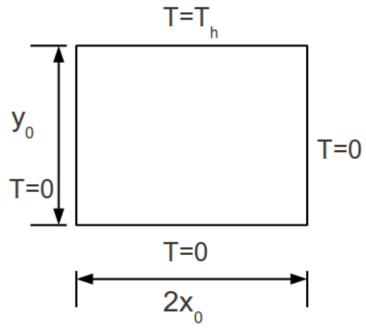

Figure 2.7: Schematic of the case study 2.3.3

(see figure 2.5). The medium scatters isotropically and is assumed to be in radiative equilibrium, i.e the thermodynamic equilibrium is assumed by virtue of thermal radiation which is supposed the dominant mode of heat transfer. The numerical results of the FVM for dimensionless heat flux on the hot wall ($q^{**} = \frac{q}{\sigma T_h^4}$) and the dimensionless centreline incident radiation ($G*$) have been calculated and compared with the exact solution of Crosbie and Shrenker [11]. Two geometries were tested in the simulations: $D_y/D_x = 1$ and $D_y/D_x = 10$ using the step scheme and different grid sizes. There is a good agreement between the numerical results and the exact solution of Crosbie and Schrenker [11]. The numerical results approached to the exact solution by refining the spatial and angular mesh (see figure2.6(a)). Figure 2.6(b) shows the dimensionless incident radiation $G*$ at $x/D_x = 0.5$ for $D_y/D_x = 10$ which gives a good agreement with exact solution of Crosbie and Schrenker. Fixing N_ϕ and varying N_θ the numerical results practically remain unchanged because of the two dimensional simulation which varies essentially with the ϕ angle.

2.3.3 Absorbing, emitting and isotropically scattering medium

This study case is a two dimensional rectangular enclosure which contains an absorbing, emitting and isotropically scattering medium. The enclosure with a width of $2x_0$ and a height of y_0 is surrounded by black walls: the top wall is hot and the other three are cold. All results are non-dimensional with respect to the incident flux, i.e. the radiative heat flux introduced by the hot wall. The geometric configurations are described in terms of the aspect ratio $A = 2x_0/y_0$, if the geometry is a square enclosure then $A = 1$ [12]. The medium properties are expressed in terms of the single scattering albedo $\omega = \frac{\sigma}{\beta}$ and the extinction coefficient β. Figures 2.8(a) and 2.8(b) show the nondimensional heat flux in the bottom wall in the case: A=1,

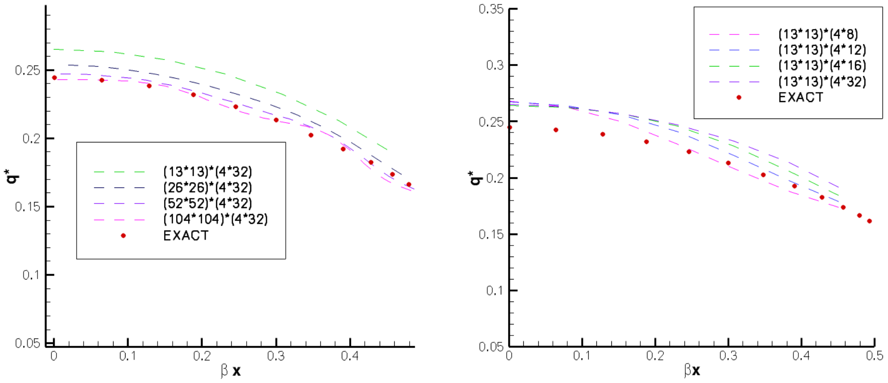

(a)

(b)

Figure 2.8: Case 2.3.3: Variation of the dimensionless heat flux (a) with spatial discretisation and (b) with angular discretisation.

$\omega = 1$ and $\beta y_0 = 1$ for different spatial and angular discretisations. By fixing the angular discretisation and refining the spatial grid (see figure 2.8(a)) the results approach to the exact results of Crosbie and Schrenker [13] and the errors due to false scattering decrease, however a wavy nature of the radiative flux appear at the finer spatial grids which reveals the presence of the ray effects. Such effect is not noticed in coarse spatial grid because the false scattering and ray effects tend to compensate each other.

This phenomena can be explained by the fact that the grid refinement reduce the spatial discretisation errors (false scattering), but have no influence on the error due to ray effects. The observed wavy solution is due to ray effects errors which are no longer masked by spatial discretisation errors [9] (see also section 2.2.1).

On the other hand, by fixing a coarse spatial discretisation and decreasing the angular discretisation (fig 2.8(b)) a smooth distribution is obtained and the ray effect seems to have decreased, however, the solution accuracy was not improved. In fact the ray effects are only reduced by using a finer angular discretisation.

2.3.4 Normal collimated incidence problem

This problem consists of the study of a normal collimated incidence radiation in a black square enclosure and filled with a pure isotropically scattering medium ($\sigma_s =$

1, $\kappa = 0$). The top wall of the black enclosure is subjected to a normal collimated beam and the other walls are maintained at 0 K. This problem has been simulated with two methods: *i)* by arranging the control angles in a manner where the collimated incidence can be captured by matching the direction of the collimated beam (see figure 2.10) [5], *ii)* by separating the diffuse part and the collimated remnant as it is explained in section 2.2.2 [2].

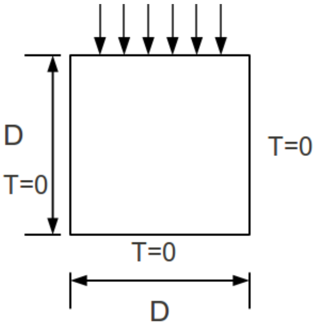

Figure 2.9: Schematic of the case 2.3.4.

In the first method, the control angle was set to 2° around the direction of the collimated beam (for θ and ϕ directions) and the remaining control angle has been divided in equal angles.

The simulations have been carried out for a spatial discretisation of (25×25) control volumes and (3×24) control angles in the θ and ϕ directions which are similar to the Kim and Lee 's discretisations [14]. The nondimensional heat flux that reach different walls of the enclosure (q^{***}) has been calculated using the two methods and compared with the discrete ordinates solution of Kim and Lee [14]. All the heat fluxes have been calculated respect to the incident collimated radiation which penetrate across the top wall. Both methods give a good agreement with the solution proposed by Kim and Lee [14] and the separating method (method 2) seems to be more accurate (see figure 2.11). Figure (2.11) shows that the scattering media transmits (to the bottom wall) more radiative energy through the medium and scatters (to the top wall) less energy back. There is a nonuniformity of the flux distribution for the energy losses through the side walls; the flux is large near to the top wall where the collimated energy is incident and is small near to the bottom wall.

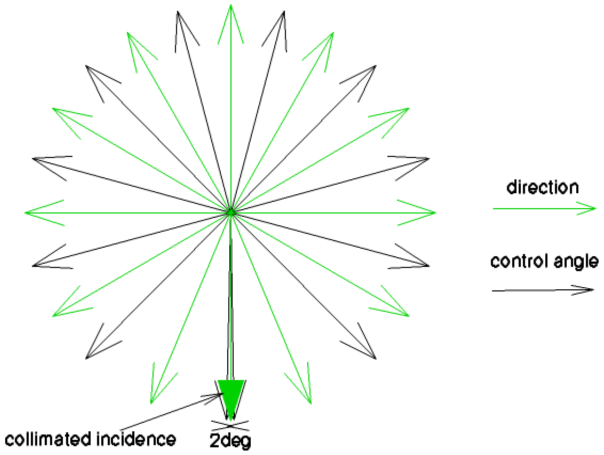

Figure 2.10: Case 2.3.4. Control angle arrangement.

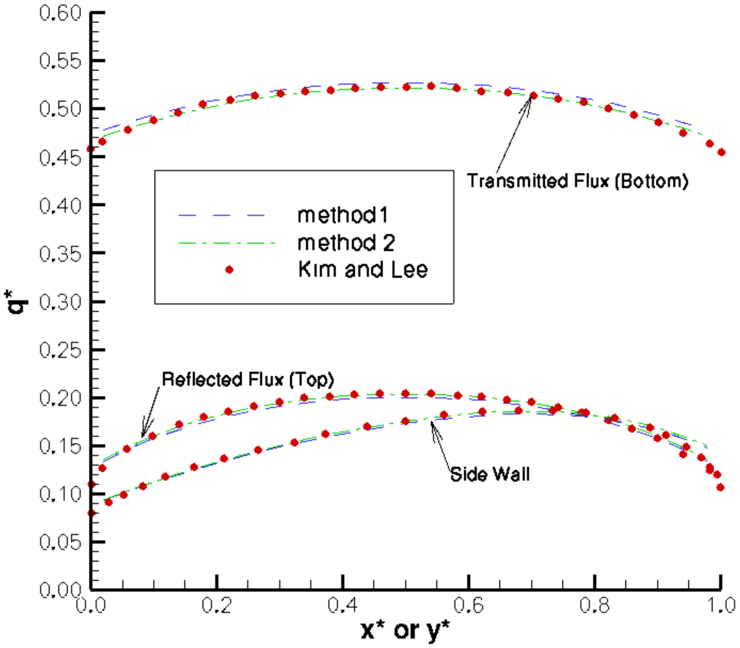

Figure 2.11: Case 2.3.4. Comparison of dimensionless heat fluxes for all walls.

2.3.5 Oblique collimated incidence problem

In order to examine the influence of the direction of the collimated incidence, the previous problem has been considered with a transparent section of the top wall ($0 \leq x \leq 0.2$) exposed to a uniform collimated beam which travels in the direction of $\theta_c = 90\,^{\circ}$ and $\phi_c = 300\,^{\circ}$. The other part of the top wall ($0.2 \leq x \leq 1$) is black and cold. The medium is homogeneous and pure isotropically scattering.

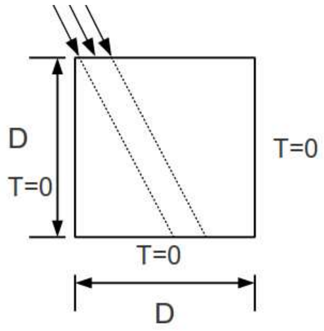

Figure 2.12: Schematic of the case 2.3.5.

This case has also been simulated with the same methods employed in section 2.3.4. The nondimensional heat flux at the bottom wall respect to the incident radiation (q^{***}) has been calculated for both methods and with different discretisations. The numerical results have been compared with the results of the step scheme using $ISW_1 + LSH$ based on discret ordinate method presented by Li [15] and the Monte Carlo Method.

The heat flux distributions on the bottom wall present a step change at $x = 0.5773505$ m and $x = 0.7773503$ m which is the region where the collimated radiation would be transmitted. The radiative flux in the shaded region is due strictly to the scattered radiation from the illuminated region (collimated) of the enclosure. Figure (2.13(a)) shows the numerical results obtained by the first method (control angle arrangement) for different spatial and angular discretisations. The results remain practically constant for different angular discretisations, however, a refinement of the spatial grids improve significantly the results accuracy compared to the Monte Carlo Method [15]. This is due essentially to the false scattering as the collimated beam is oblique and it is very clear in the coarse meshes. Figure (2.13(b)) shows the results obtained using the separation between diffuse and collimated radiation (method 2) for different spatial and angular discretisations. This method gives better results than the first method even for coarse spatial grids and reduce clearly the

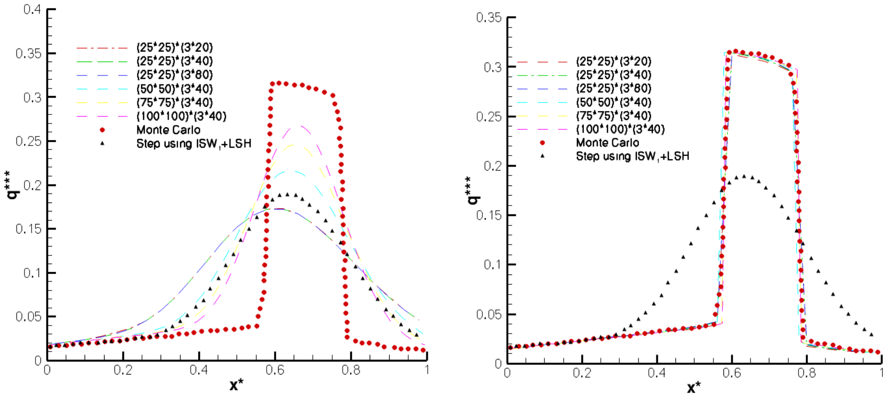

(a) (b)

Figure 2.13: Case 2.3.5 dimensionless heat flux distributions on the bottom wall using (a) method 1 and (b) method 2.

effect of false scattering. This is due to the fact that the separating method calculates the collimated remnant analytically which is the most part affected by the false scattering.

2.3.6 Oblique collimated with specular reflecting walls

This case is similar to the case 2.3.5 with the difference that the bottom wall emissivity is assumed to be 0.5 rather than 1.0 and the oblique collimated travels in the direction of $\theta_c = 90^\circ$ and $\phi_c = 285^\circ$. The reflectivities of the bottom wall are segmented into diffuse and specular components defined by f_d which is the diffuse fraction of the reflectivity. First, the problem has been solved in a transparent medium and then in an isotropically scattering medium ($\sigma_s = 1$, $\kappa = 0$). Both methods commented in section (2.3.4) have been implemented and compared using different values of f_d. The main objective of this case is to simulate the effect of specular reflecting walls under oblique collimated, however due to the lack of similar cases in literature the predicted results were not validated with other numerical or experimental data.

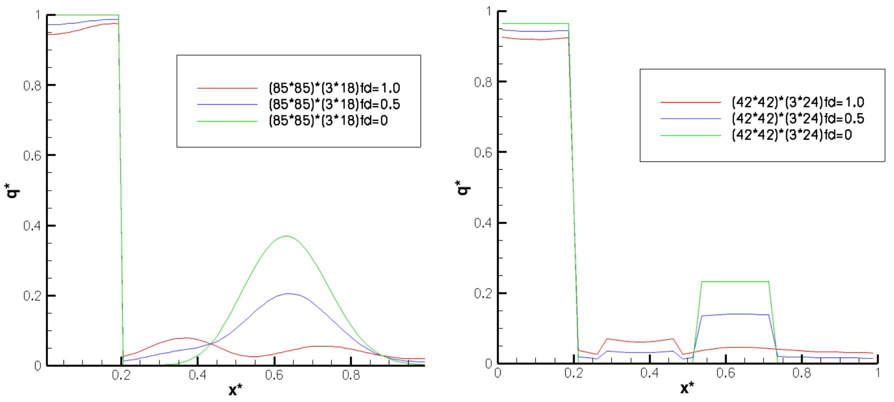

(a) (b)

Figure 2.14: Case 2.3.6 dimensionless heat flux along the top wall using (a) the arrangement method and (b) the separation method

Transparent medium

The method of arrangement of control angle is implemented using fine spatial grids to reduce the effect of false scattering. Figure (2.14(a)) shows the results of the dimensionless heat flux along the top wall for different fraction of reflectivity in a transparent medium.

The dimesionless heat flux along the top wall starts with a stair in the entrance of the collimated beam $(0.0 \leq x \leq 0.2)$. The change of heat flux in the region where the collimated beam is reflected by the bottom wall $(0.53 \leq x \leq 0.73)$ is smeared. This is mainly due to false scattering. In the diffuse boundary cases ,i.e. $f_d = 1.0$ or 0.5, the heat flux presents a small peak in the region $(0.26 \leq x \leq 0.46)$ which corresponds to the opposite region where the collimated beam shocks the bottom wall. The diffuse bottom wall reflects the incoming heat flux to nearest zone of the top wall $(0.26 \leq x \leq 0.46)$. The separation method is also used to solve this problem using a spatial grids of (42×42) and an angular discretisation of (3×24). Figure (2.14(b)) shows that the dimensionless heat flux presents a stair in the region where the collimated beam is reflected $(0.53 \leq x \leq 0.73)$ in the purely and partially specular reflecting cases. It also shows other peak in the region $(0.26 \leq x \leq 0.46)$ which is due to the diffuse part and it is significant in the diffuse reflecting case.

The specular boundary condition reflect the incoming heat flux symmetrically. The separation gives a clear stair at the region where the collimated beam is reflected. However, the heat flux is smeared in the arrangement method due to the

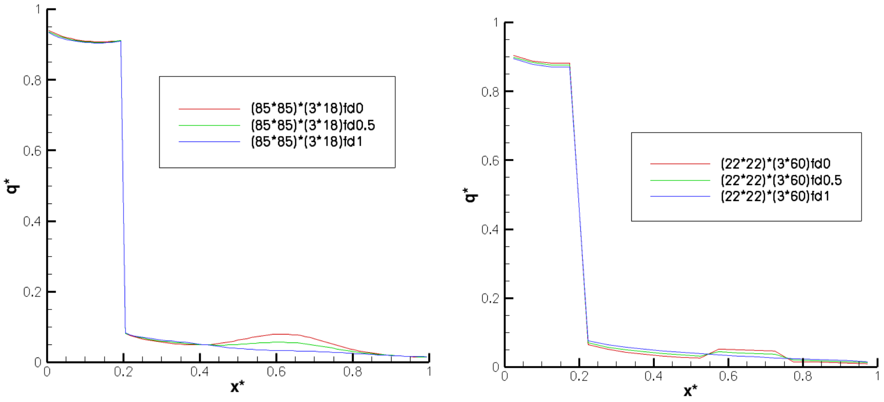

(a) (b)

Figure 2.15: Case 2.3.6 dimensionless heat flux along the top wall in a scattering medium using (a) the arrangement method and (b) the separation method

false scattering. In diffuse boundary cases a small peak is noticed in the opposite region where the collimated beam hits the bottom wall and the heat flux is reflected diffusely.

Pure scattering medium

The same simulation was done for the case of pure scattering medium using both methods: arrangement and separation methods. The same angular discretisation is used in the separation method like in the transparent medium. Both figures (2.15(a)) and (2.15(b)) show that the dimesionless heat flux was attenuated in the pure scattering medium compared to the transparent medium. This attenuation is due to the scattering medium and the redirection of the radiative flux to the sides. Furthermore, the two methods used in this simulation give a good similarity and the same differences commented in the transparent medium. The arrangement method shows also a smeared heat flux due to the effect of the false scattering.

2.3.7 Central blockage problem

The problem consists of a square enclosure with a central blockage (an internal square with the half length of the enclosure). All the walls are assumed black and maintained at $300K$ except for the left boundary of the enclosure which is set to

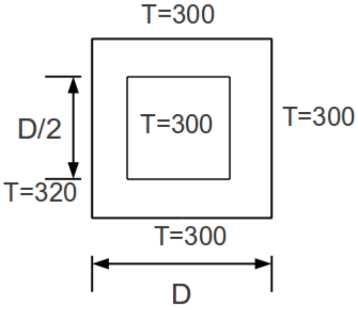

Figure 2.16: Schematic of the central blockage problem

$320K$. The heat flux has been calculated along the enclosure walls for the superior half of the enclosure because of the symmetry of the problem. The solution agrees with the NRM solution [16] and presents a high radiation flux in the hot wall with negative radiation flux in the walls that see the hot wall. Figure (2.17(b)) shows the heat flux distribution at the walls of the square internal blockage. It is observed from this figure that the incoming heat flux to the side in front of to the hot wall is high and decreases at the shaded faces.

2.3.8 Normal collimated radiation in a rectangular enclosure containing a black square

This case is a preliminary case to simulate the collimated solar radiation passing through a PTC. The geometry of the problem is similar to the geometry presented in section 2.3.7 and consists of a rectangular enclosure subjected to a normal collimated beam at the top wall and a black square placed in the centre of the enclosure (see figure 2.18). The medium is supposed transparent medium. Except in the top wall, which is transparent, the rest of the walls (also for the centred square) are gray and the reflectivities are segmented into diffuse and specular components defined by f_d. The FVM has been used in the simulations by arranging the control angles to capture the collimated beam. The domain is divided into (40×40) uniform control volumes and (3×24) control angles in the θ and ϕ directions. In the same way as the previous section, the control angle corresponding to the collimated beam was set to 2 °, as well as, for the others symmetric directions which are used in the specular reflection. The absolute non-dimensional heat flux is calculated along the internal square for different values of f_d and shown in figure (2.19). In the total specular reflection case $(f_d = 0)$, the radiative flux is higher in the top wall of the internal square where

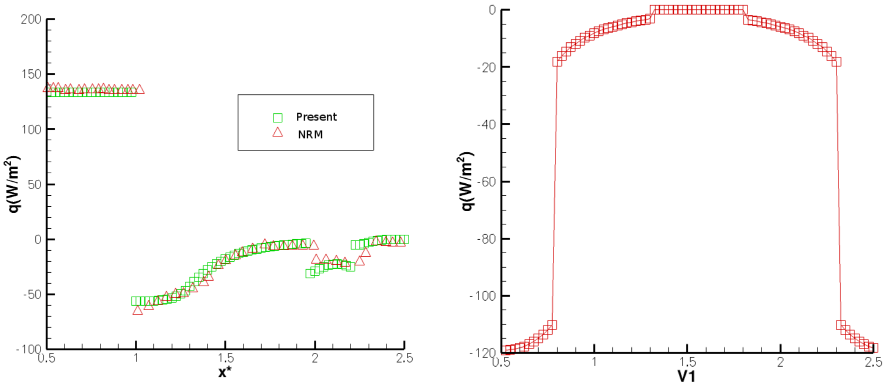

(a) (b)

Figure 2.17: Case 2.3.7. Local heat flux along (a) the enclosure walls and (b) the centered internal blockage.

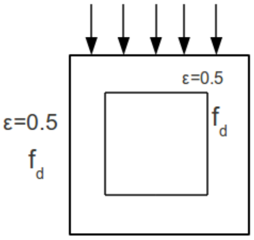

Figure 2.18: Schematic of the case 2.3.8.

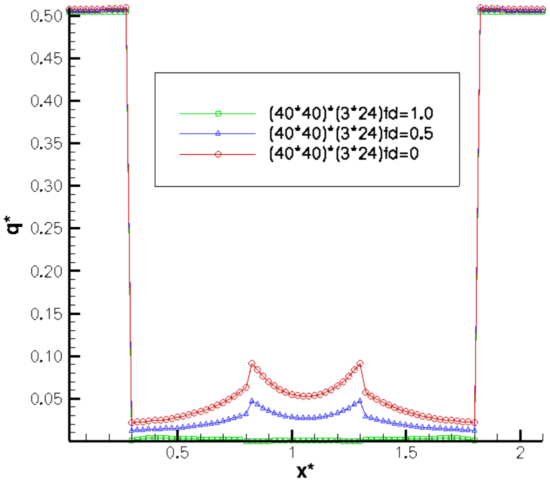

Figure 2.19: Case 2.3.8. Absolute nondimensional heat flux along the internal square.

is exposed to the collimated beam and practically zero in the other walls due to the shadow effect and the normal incidence of the collimated beam. Increasing the diffuse fraction, the heat flux at the walls of the internal square also increases and the normal incidence is distributed in many directions which could reach the walls of the internal block. The radiative flux increases in the sides walls (left and right) near to the down corner due to the reflection of the enclosure walls. Furthermore, the radiative heat flux decreases in the centre of the bottom wall of the internal square due to the shadow effect.

2.4 Resolution of the RTE for a parabolic trough solar collector using the FVM

After all these preliminary study cases, the FVM is applied to a parabolic trough solar collector placed in the horizontal position (perpendicular to the solar rays). The solar irradiation is modelled as a collimated beam without taking into account the influence of the finite size of the Sun [17]. The collimated beam is solved through its path to the absorber tube. The direct part of the solar radiation is only considered as it is several times higher than the diffuse one. The medium is assumed transparent and no participating, i.e $\sigma_s = \kappa = 0$. The mirror is assumed to be totally specular

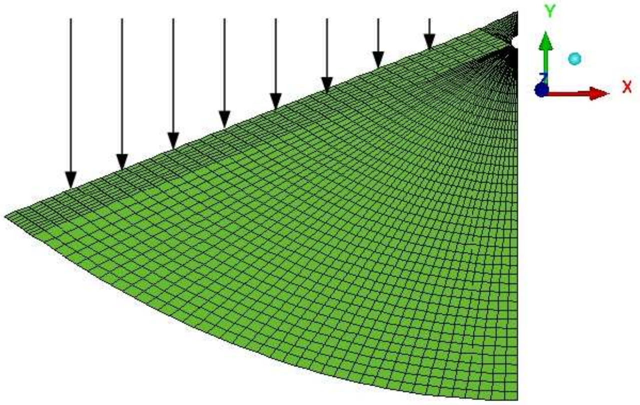

Figure 2.20: Domain and mesh used for the radiation analysis around a PTC

reflecting for solar irradiation and opaque. The specular direction is determined by the reflection law.

$$\vec{s}_s = \vec{s}_i - 2(\vec{n} \cdot \vec{s}_i)\vec{n} \tag{2.31}$$

Optical properties are obtained from the literature [18] according to the specifications defined by the manufacturer and determined at zero incident angle. A 3D structured, non-orthogonal and non-overlapping grid is used to discretise the domain between the parabola and the receiver tube. The domain is reduced to the half because of the symmetry around the y axis. The angular space (4π) is subdivided into $N_\theta \times N_\phi = M$ non-overlapping control angles. In order to reduce the effect of the false scattering, the mesh is arranged to follow the direction of the reflected rays. The number of directions in the azimuthal direction is chosen according to the spatial discretisation along the parabola and adjusted to capture the direction of the specular reflection (see figure 2.20). The angular mesh contains all the directions of the reflection focused on the focal point of the parabola. The angular discretisation is arranged to capture the collimated incidence which comes from the Sun irradiation [5]. The collimated intensity is solved directly by the FVM (method 1 presented in section 2.3.4). The angular space between two consecutive reflection directions is filled with an extra direction. The step scheme is used to relate the control volume facial intensity to the nodal one. The discretised algebraic radiative transfer equations and boundary conditions are solved by means of a parallel sweep solver [19]. Numerical results are compared first with semi-analytical results of Jeter [20] and then with numerical results of Cheng et al. [21] which are obtained with the MCRT

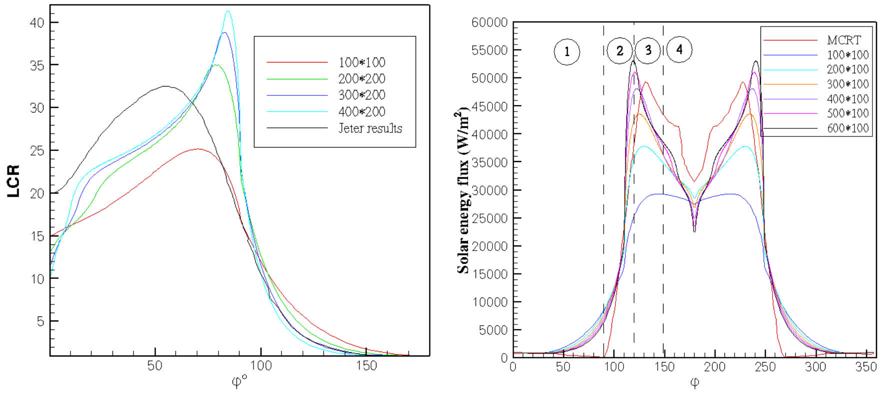

(a) (b)

Figure 2.21: Verification of the optical model: (a) comparison of the LCR distribution with Jeter's results [20] (b) comparison of the solar energy flux distribution with MCRT resutls [21].

method. The geometric shape of the PTC (Model 3001-03) used by Jeter [20] is reproduced. Jeter considered the influence of the finite size of the sun, "the cone optics" , which is not considered in the FVM resolution. This phenomenon causes a spreading of the reflected incident radiation around the absorber and can not be considered by assuming the solar radiation as a collimated beam. The solar heat flux is expressed by a parameter called Local Concentration Ratio (LCR) [20] which presents the ratio of the concentrated solar flux at the absorber surface to the incident solar radiation. Figure 2.21(a) shows the comparison of the LCR obtained by the optical model and the analytical results of Jeter [20]. It can be seen that increasing the number of nodes in the azimuthal direction of the absorber, the false scattering decreases. The main differences between the present results and the results of Jeter is the influence of the finite size of the sun, which tends to moderate the solar flux distribution around the absorber and the false scattering. This is why the maximum obtained by the present model is higher when decreasing the false scattering.

The optical model has also been verified with the numerical results of Cheng et al. [21] for a typical LS-2 PTC module which has been tested by Dudley et al. [18]. Different grids systems are studied and compared with the MCRT solution [21]. The spatial grid system ($n_A = 100$, $n_P = 600$ where n_A is total number control volumes in the aperture of the parabola and n_P is the total number of control volume in the parabola) has been chosen as the most adequate one because it presents low false scattering and good trend to the results of Cheng et al. [21]. The main difference between the present results and those of Cheng et al. [21] is due to the cone optic effect which is taken into account in their paper. As it is shown in figure 2.21(b) the solar flux distribution is symmetrical but non-uniform. The curve of the solar flux can be divided into 4 zones (which have been indicated in in figure 2.21(b)): i) the direct radiation zone where the absorber tube only receives the direct solar irradiation without concentration, ii) the heat flux increasing zone where the heat flux increases rapidly because of the reflection of the solar irradiation, iii) the heat flux decreasing zone where the reflected solar flux decreases because of the parabolic shape, iv) the shadow effect zone where the heat flux is much lower and decreases rapidly because of the solar irradiation is shadowed by the absorber tube.

2.5 New optical model

In order to take into account the cone optic and reduce the computational cost of the application of FVM, a new optical model is developed to calculate the solar heat flux around the HCE. This model uses a numerical-geometrical method based on ray trace and FVM techniques to project the solar optic cone of so known the finite size of the Sun [17] on the absorber surface.

The incident solar irradiation is represented as a ray package, defined by the optic cone or *sunshape*, i.e., rays are symmetrically distributed around a central one within the angle range $(\phi_s, -\phi_s)$, where $\phi_s = 16$ arcminutes [22]. The solar-optical properties of the system (specular reflectance of the collector parabola, ρ_s, the effective glass envelope transmittance, τ_{eff}, and the effective coating absorptance of the absorber, α_{eff}) are assumed to be independent of the temperature and the angle. It is considered that the thickness of the glass is very small, so the change of direction of the rays that cross the glass according to the Snell's law is neglected. Thus, the present method computes directly the solar irradiation that reaches the absorber tube. The effect of the glass is considered by means of reducing the solar irradiation that arrives at the absorber tube by τ_{eff}.

The method consists of resolving the RTE as expressed in equation 2.3. The medium is assumed transparent leading to,

$$\frac{dI(x, y, \hat{s})}{ds} = 0 \tag{2.32}$$

Because of the symmetry of the problem, the treatment is described for one half of the PTC and is the same for the other part. The PTC is discretised into four grid systems as shown in Figure 2.22: *i)* N_1: the number of CVs in the space between the absorber and the edge of the aperture, *ii)* N_2: the number of CVs in the front space of the absorber tube, where it receives only the direct irradiation from the Sun, *iii)* N_3:

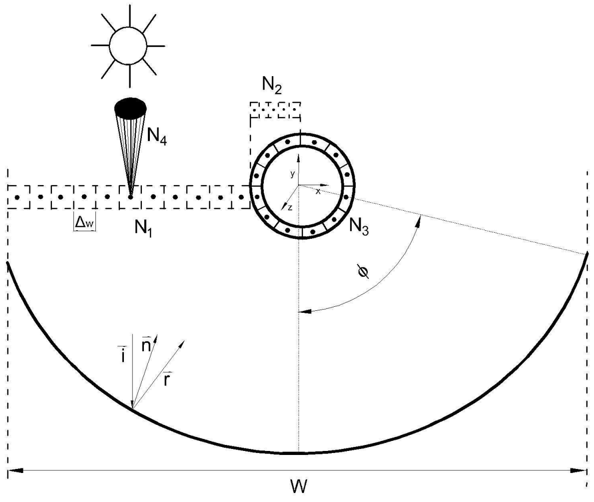

Figure 2.22: Schematic of spatial and angular distcretisation of the system.

the number of CVs around the absorber tube in the azimuthal direction and, *iv)* N_4 the total number of the control angles in the optic cone.

First, the incident optic cone is symmetrically discretised into N_4 control angles around the central ray and projected on the parabola surface, represented by N_1 CVs, and on the front face of the absorber, represented by N_2 CVs. The direct incident solar irradiation, i.e., solar irradiation that reaches the absorber surface, without reflection on the parabola, is integrated directly over each absorber CV. The other part of the incident solar irradiation, hits the parabola surface and is then specularly reflected. The incident ray in the direction $\vec{i}$ is reflected respect to the normal of reflector surface $\vec{n}$ (see Figure 2.22). The direction $\vec{r}$ of the reflected ray is given by the law of specular reflection,

$$\vec{r} = \vec{i} - 2(\vec{n} \cdot \vec{i})\vec{n} \tag{2.33}$$

Since perfect solar elevation tracking system is considered, the reflected rays are concentrated in the focus line of the parabola. The amount of solar energy transported by a reflected ray q_{ref} is given by,

$$q_{ref} = \frac{\rho_s I_{s.in} \Delta_w}{N_4} \tag{2.34}$$

where $\Delta_w = \left(\frac{\frac{W}{2} - r_a}{N_1}\right)$ is the length of the CV in the aperture zone represented by N_1

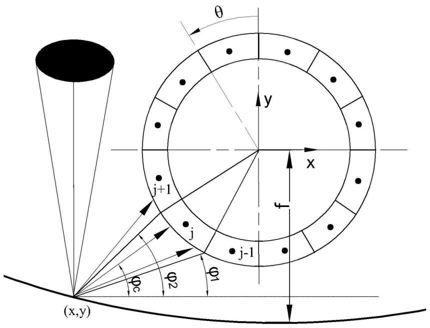

Figure 2.23: Schematic of the reflection of the optic cone on the absorber tube.

CVs.

For a given CV of the aperture zone, the reflected central ray, which is coming from the central ray of the optic cone, makes an angle $\varphi_c = \tan^{-1}(\frac{f-y}{x})$ with the x axis, where x and y define the spatial position of the intersection point of the ray at the parabola (see Figure 2.23). The angle φ formed by a general reflected ray that impinges in a given CV of the aperture zone, and the x axis for each coming ray from the optic cone is then calculated as $\varphi_m = \varphi_c \pm m\Delta\varphi$ where m is an integer that varies from 0 to $N_4/2$. After that, the absorber tube is looped to determine the intercepted rays coming from the reflected rays of the optic cone. For an absorber CV j, φ_1 and φ_2 are defined (see Figure 2.23).

$$\varphi_1 = \tan^{-1}\left[\frac{|f-y| - r_a\cos\theta_j}{|x - r_a\sin\theta_j|}\right] \tag{2.35}$$

$$\varphi_2 = \tan^{-1}\left[\frac{|f-y| - r_a\cos\theta_{j+1}}{|x - r_a\sin\theta_{j+1}|}\right] \tag{2.36}$$

A reflected ray which forms an angle φ with the x axis is intercepted by j-th absorber CV if φ lays between φ_1 and φ_2. This procedure is repeated for all CVs of the aperture zone N_1. The solar energy absorbed by the absorber tube and the glass envelope is obtained by summing the reflected rays (q_{ref}) that reach the j-th CV.

$$\dot{q}^{j}_{a,s.rad} = (\tau\alpha)_{eff}\sum q_{ref} \tag{2.37}$$

$$\dot{q}^{j}_{g,s.rad} = (1 - (\tau\alpha)_{eff})\sum q_{ref} \tag{2.38}$$

The total absorbed energy $\dot{q}_{a,s.rad}$ is determined by adding the direct (that lies in N_2) and the reflected incident solar irradiation, which corresponds to the integral of equation (2.37), over all CVs of the absorber (N_3).

The optical model provides the solar heat flux distribution around the HCE, as well as, the optical efficiency η_{opt} of the PTC, which is defined as the ratio of energy absorbed by the absorber to the energy incident on the collector's aperture.

$$\eta_{opt} = \frac{\dot{q}_{a,s.rad}}{\dot{q}_{s.inc}} = \frac{((W - D_a)\rho_s + D_a)\,(\tau\alpha)_{eff}}{W} \tag{2.39}$$

This ratio is often approximated to $\rho_s(\tau\alpha)_{eff}$ as the reflected part is much more important than the direct one.

The previous treatment have dealt with the PTC having a perfect parabolic cross-sections. However, in practice, the optical errors are included in the so-called intercept factor γ which is usually calculated using statistical approaches [23, 24] or experimentally [25] and remains only an approximation.

Using a solar elevation tracking system, the Sun will be maintained in the $y - z$ plane but not usually normal to the collector aperture ($x - z$ plane) making an incident angle φ_{inc} respect to the normal. Then, the reflected energy q_{ref} is decreased by $\cos(\varphi_{inc})$ while the apparent cone optic is expanded and increased as $1/\cos(\varphi_{inc})$. Thus, the algorithm of solar absorption analysis for non-zero incident solar irradiation remains the same as described before with both modifications of the reflected energy and cone optic size. It should be pointed out that, the implementation and the resolution of this optical model is much faster than other ray tracing techniques and requires lower computational efforts for obtaining similar results.

In order to verify the accuracy of the optical model, the results are compared with available references from the literature. The geometrical-numerical method presented in this work is validated using the ideal PTC with round absorber adopted by Jeter [26], where geometric concentration $GC = 20$, rim angle $\theta_{rim} = 90°$ for an optic cone of 0.0075 rad and optical properties (ρ_s,τ and α) are equal to unity. Under these conditions, the solar heat flux distribution is compared to the analytical results found by Jeter [26]. A grid independence study is carried out and tested for different grid systems. The grid with parameters $N_1 = 640$, $N_2 = 160$, $N_3 = 160$, and $N_4 = 320$ is regarded as grid-independent since there is no significant difference with the finer one. The Local Concentration Ratio (LCR), which is defined by the ratio of solar radiative heat flux falling on the surface of the absorber tube to that which falls on the reflective surface of the collector, is calculated. It is a significant parameter of the heat flux distribution. The present results are in a good agreement with those of Jeter with the same trend and the same minimum and maximum values and deviations smaller than 8% (see Figure 2.24).

The distribution of the LCR along the azimuthal direction can also be divided in

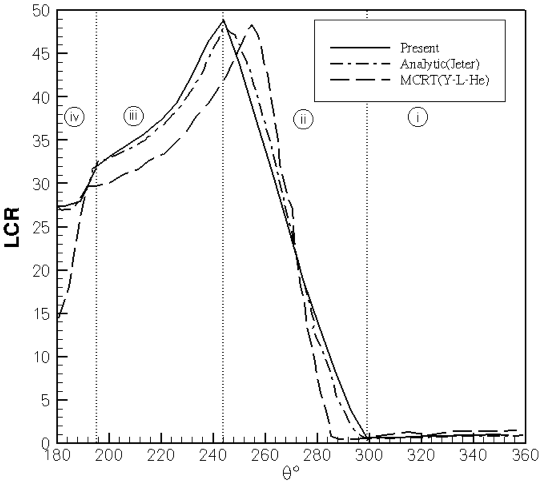

Figure 2.24: Local concentration ratio distribution along the azimuthal direction. Solid line: present results, dashed line: analytical results of Jeter [26], dashed-dotted line: MCRT results of He et al. [27]

four zones similarly to section 2.4 depending to radiation and concentration zones.

In figure 2.24, the results obtained by He et al. [27] for the same case using a MCRT method are also plotted. As can be seen from the figure, the present model yields better results than those presented in [27] especially for the shadow effect zone.

The solar heat flux distribution around the HCE is also simulated for the same PTC described above (Jeter case) and for different incident angles.

Figure 2.25 shows the comparison between the computed results obtained by the present optical model and the analytical results of Jeter [26]. There is a good agreement between both results for different incident angles which proves the accuracy of the present optical model. It can also be seen from Figure 2.25 that the heat flux distribution decreases with the increase of the incidence angle ϕ_{inc}. This decrease is due to the effect of the cosine of the incident angle which becomes significant for larger angles (near to 90°). The optical efficiency is at maximum only when the incoming radiation is normal to the aperture. The peak of concentration is approached to the lowest position of the absorber tube (θ=180°) as the incident angle increases. The concentration tends to spread around the lower half of the absorber tube with the increasing of the incident angle.

The heat flux distribution around the absorber tube is compared with the MCRT

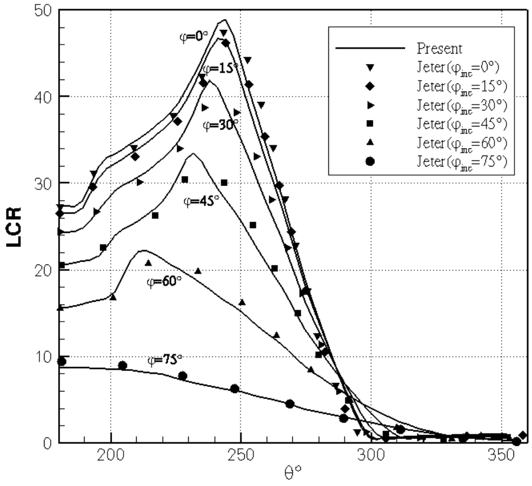

Figure 2.25: Local concentration ratio distribution along the azimuthal direction for different incident angles. Solid line: present results, dashed line: analytical results of Jeter [26]

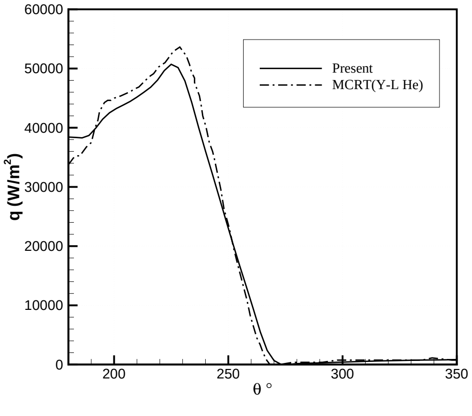

Figure 2.26: Heat flux distribution around the absorber tube for LS-2 collector with incident radiation of 933.7 W/m^2. Comparison with the results of He et al. [27].

Table 2.1: Parameter of the LS-2 solar collector [18] used in the model validation

Parameter	Value
Receiver length (L)	7.8m
Collector aperture (W)	5m
Focal distance (f)	1.84m
Absorber internal diameter ($D_{a,in}$)	0.066m
Absorber external diameter ($D_{a,ex}$)	0.070m
Glass internal diameter ($D_{g,in}$)	0.109m
Glass external diameter ($D_{g,ex}$)	0.115m
Receiver absorptance (α)	0.96
Glass transmittance (τ)	0.95
Parabola specular reflectance (ρ_s)	0.93
Incident angle (φ_{inc})	0.0

results of He et al. [27] for the case of LS-2 solar collector [18] with an incident solar irradiation of $933.7 W/m^2$. The detailed specifications of a LS-2 solar collector are given in Table 2.1. Figure 2.26 shows the comparison of the solar heat flux distribution with the MCRT results and demonstrates a good agreement being the maximum deviation lower than 13 %. However, there are some differences in the shadow effect zone, which have been discussed before.
The influence of geometric concentration is also studied by varying the ratio of $GC = \frac{W}{\pi D_{a,ex}}$. For this purpose, the aperture is kept constant and only the absorber radius is changed. The solar heat flux is calculated for different GCs: 10, 30, 50 which correspond to the radius of the absorber: $0.08m$, $0.027m$, $0.016m$, respectively, with an aperture of $W = 5m$ and a rim angle of $90°$. The numerical results of the heat flux distribution around the circumference of the absorber tube are compared with the results of He et al. [27] for the same GCs in figure 2.27. The results show a good agreement with the MCRT results of He et al. [27] with the same maximum and minimum values. As it was expected the heat flux increase with the geometric concentration and the peak is displaced toward the shadow effect zone. Therefore, the span angle of the heat flux increasing zone become larger and the shadow effect become weaker.

Finally, the influence of the rim angle on the heat flux distribution is also studied by fixing the absorber radius $R_{a,ex} = 0.035m$ and changing the rim angle. Figure 2.28 shows the variation of the heat flux distribution on the outer surface of the absorber under different rim angles and compared with the MCRT results of He et al. [27]. Present results are in good agreement with the MCRT results except some dif-

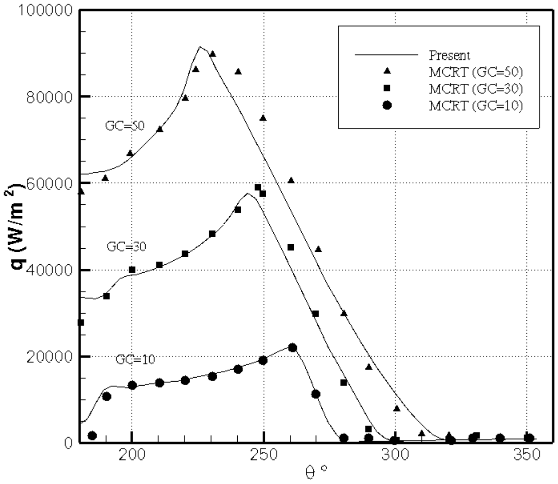

Figure 2.27: Variation of the heat flux distribution with the geometric concentration. Comparison with the MCRT results of He et al. [27].

ferences in the shadow zone which have been discussed before. By increasing the rim angle the maximum value of the heat flux become lower and moves toward the position θ =360° except for $\theta_{rim} = 15°$. The span angle heat flux decreasing zone and the shadow effect zone increase with rising the rim angle because the concentration area becomes larger which cause the maximum heat flux reduction. At $\theta_{rim} = 15°$ the maximum value of the heat flux is decreased because the rim angle is so small causing some reflected rays to go out and miss the absorber. According to Riveros and Oliva [17], the minimum absorber radius able to intercept all the reflected rays coming from the parabola is $R_{min} = 2fsin\phi_s/(1+cos\theta_{rim})$. This minimum is equal to $0.0449m$ for the case of $\theta_{rim} = 15°$ (f=9.49) which is bigger than the radius of the absorber tube.

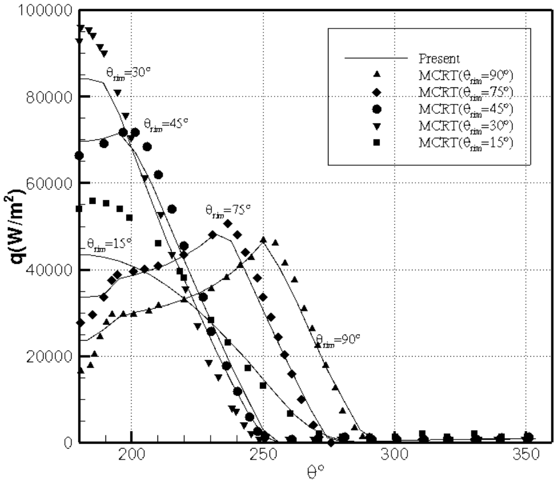

Figure 2.28: Variation of the heat flux distribution with the rim angle. Comparison with the MCRT results of He et al. [27].

2.6 Conclusions

The RTE has been implemented for a participating medium taking into account the act of absorption, emission and scattering. A general solution for this equation was proposed applying the FVM. This method has been applied to different test cases and preliminary cases for the study of the solar radiation around the receiver of a PTC. These cases include transparent, absorbing, emitting and isotropically scattering media in two-dimensional enclosures. The implemented code has been validated according to numerical solutions found in the literature. Two shortcomings of the FVM have been identified: ray effect and false scattering. Ray effect arises from angular discretisation and false scattering is a consequence of the spatial discretisation practice. The interaction between these two shortcomings has been discussed. The collimated irradiation has also been studied for normal and oblique incidence. Two methods have been proposed to solve the collimated radiation. The first method is similar to the iterative process used to solve the RTE with the only difference is the arrangement of control angles to capture the collimated incidence. The second method is the separation of the collimated remnant and the diffuse part and solve the RTE of each part. Both methods have been implemented and compared to the results found in the literature where a good agreement is observed, however the second method gives better solution and reduces the false scattering. The same methodology has been followed to solve the solar distribution around the HCE of a PTC by means of a parallel sweep solver. Only the direct part of the solar radiation has been considered. The mirror is assumed to be totally specular reflecting for solar irradiation and opaque surface. The solar radiation is modelled as a collimated beam without taking into account the finite size of the Sun. The comparison between the FVM results and the numerical results found in literature gives an overestimation of the maximum of the solar flux distribution around the absorber due to the effect of the aforementioned finite size of the Sun. This phenomenon result in spreading of the reflected incident radiation around the absorber.

For this reason, a new optical model has been developed in order to take into account the optic cone and reduce the high computational cost of the FVM solution. The new method uses a numerical-geometrical approach based on ray trace and FVM techniques to project the solar optic cone on the absorber surface. The accuracy of the new optical model has been verified with the comparison with analytical results of Jeter and for different incident angles. The present model yields better results than the MCRT model especially for the shadow effect zone. A good agreement is also found in the comparison of the solar heat flux distribution around a HCE of a LS-2 solar collector respect to the MCRT results.

References

[1] G.D. Raithby and E.H. Chui. A Finite-Volume Method for predicting a radiant heat transfer in enclosures with participating media. *Journal of Heat Transfer*, 112:415–423, 1990.

[2] M.F. Modest. *Radiative heat transfer*. Academic Press, 2003.

[3] E.H. Chui and G.D. Raithby. Prediction of radiative transfer in cylindrical enclosures with the finite volume method. *Journal of Thermophysics and Heat Transfer*, 6(4):605–611, 1992.

[4] E.H. Chui and G.D. Raithby. Computation of radiant heat transfer on a nonorthogonal mesh using the finite-volume method. *Numerical Heat Transfer*, 23(3):269–288, 1993.

[5] J.C. Chai, H.S. Lee, and S.V. Patankar. Improved treatment of scattering using the discrete ordinates method. *Journal of Heat Transfer*, 116:260–263, 1994.

[6] B.G. Carlson and K.D. Lathrop. *Computing Methods in Reactor Physics*, chapter Transport Theory-The Method of Discrete-Ordinates, pages 165–266. Gorden and Breach, 1968.

[7] J.C. Chai, H.S. Lee, and S.V. Patankar. Ray effect and false scattering in the discrete ordinates method. *Numerical Heat Transfer*, 24(4):373–389, 1993.

[8] S.H. Kim and K.Y. Huh. A new angular discretization scheme of the finite volume method for 3-D radiative heat transfer in absorbing, emitting and anisotropically scattering media. *International Journal of Heat and Mass Transfer*, 43:1233–1242, 2000.

[9] P. Coelho. The role of ray effects and false scattering on the accuracy of the standard and modified discrete ordinates methods. *Journal of Quantitative Spectroscopy and Radiative Transfer*, 73(2):231–238, 2002.

[10] J.C. Chai, H.S. Lee, and S.V. Patankar. Finite volume method for radiation heat transfer. *Journal of Thermophysics and Heat Transfer*, 8(3):419–425, 1994.

[11] A.L. Crosbie and R.G. Schrenker. Radiative transfer in a two dimensional rectangular enclosures. *Journal of Heat Transfer*, 106:699–706, 1984.

[12] M.A. Ramankutty and A.L. Crosbie. Modified discrete ordinates solution of radiative transfer in two-dimensional rectangular enclosures. *Journal of Quantitative Spectroscopy and Radiative Transfer*, 57:107–140, 1997.

[13] A.L. Crosbie and R.G. Schrenker. Radiative transfer in a two-dimensional rectangular medium exposed to diffuse radiation. *Journal of Quantitative Spectroscopy and Radiative Transfer*, 31(4):339–372, 1984.

[14] T.K. Kim and H.S. Lee. Radiative transfer in two-dimensional anisotropic scattering media with collimated incidence. *Journal of Quantitative Spectroscopy and Radiative Transfer*, 42:225–238, 1989.

[15] H.S. Li. Reduction of false scattering in arbitrarily specified discrete directions of the discrete ordinates method. *Journal of Quantitative Spectroscopy and Radiative Transfer*, 86:215–222, 2004.

[16] A. Sanchez and T.F. Smith. Surface radiation exchange for two-dimensional rectangular enclosures using the discrete-ordinates method. *Journal of Heat Transfer*, 114(2):465–472, 1992.

[17] H.G. Riveros and A.I. Oliva. Graphical analysis of sun concentrating collectors. *Solar Energy*, 36(4):313–322, 1986.

[18] V. Dudley, G. Kolb, M. Sloan, and D. Kearney. SEGS LS2 solar collector-test results. Technical report, Report of Sandia National Laboratories (SANDIA-94-1884), 1994.

[19] G. Colomer, R. Borrell, O. Lehmkuhl, and A. Oliva. Parallelization of combined convection-radiation numerical. In *Proceedings of International Heat Transfer Conference14*, volume 14, pages 8–13. IHTC14, 2010.

[20] M.S. Jeter. Analytical determination of the optical performance of parabolic trough collectors from design data. *Solar Energy*, 39(1):11–21, 1987.

[21] Z.D. Cheng, Y.L. He, J. Xiao, Y.B. Tao, and R.J. Xu. Three-dimensional numerical study of heat transfer characteristics in the receiver tube of parabolic trough solar collector. *International Communications in Heat and Mass Transfer*, 37(7): 782–787, 2010.

[22] D.L. Evans. On the performance of cylindrical parabolic solar concentrators with flat absorbers. *Solar Energy*, 19:379–385, 1977.

[23] H.M. Güven and R.B. Bannerot. Derivation of universal error parameters for comprehensive optical analysis of parabolic troughs. *Journal of Solar Energy Engineering*, 108:275–281, 1986.

[24] H.M. Güven and R.B. Bannerot. Determination of error tolerances for the optical design of parabolic troughs for developing countries. *Solar Energy*, 36(6):535–550, 1986.

[25] S. García-Cortés, A. Bello-García, and C. Ordóñez. Estimating intercept factor of a parabolic solar trough collector with new supporting structure using off-the-shelf photogrammetric equipment. *Applied Energy*, 92:815–821, 2012.

[26] M.S. Jeter. Calculation of the concentrated flux density distribution in a parabolic trough collectors by a semifinite formulation. *Solar Energy*, 37(5):335–345, 1986.

[27] Y-L. He, J. Xiao, Z-D. Cheng, and Y-B. Tao. A MCRT and FVM coupled simulation method for energy conversion process in parabolic trough solar collector. *Renewable Energy*, 36:976–985, 2011.

Chapter 3

Heat transfer analysis and numerical simulation of a parabolic trough solar collector

Most of the contents of this chapter have been published as:

A.A. Hachicha, I. Rodríguez, R. Capdevila and A. Oliva. Heat transfer analysis and numerical simulation of a parabolic trough solar collector. *Applied Energy* 2013; 111: 582-592.

Abstract. Parabolic trough solar collector is the most proven industry-scale solar generation technology today available. The thermal performance of such devices is of major interest for optimising the solar field output and increase the efficiency of power plants. In this chapter, a detailed numerical heat transfer model based on the finite volume method for these equipments is presented. In the model, the different elements of the receiver are discretised into several segments in both axial and azimuthal directions and energy balances are applied for each control volume. The new optical model developed in the previous chapter is used for calculating the non-uniform solar flux distribution around the receiver. The solar heat flux is determined as a pre-processing task and coupled to the energy balance model as a boundary condition for the outer surface of the receiver. The set of algebraic equations are solved simultaneously using direct solvers. The model is thoroughly validated with results from the literature. The performance of the overall model is tested against experimental measurements from Sandia National Laboratories and other un-irradiated receivers experiments. In all cases, results obtained shown a good agreement with experimental and analytical results.

3.1 Introduction

Concentrated solar power plants are one of the most promising and mature renewable options for electric generation. Parabolic trough collectors (PTC) are the most proven, widespread and commercially tested technology available for solar harnessing. The majority of the parabolic trough plants deployed operate at temperatures up to 400 °C

According to the state-of-the-art of modelling PTC (see section 1.3), the majority of the published studies about heat transfer process in PTC are one-dimensional or two-dimensional and neglect the realistic non-uniform distribution of solar radiation around the HCE.

In this chapter, a detailed numerical simulation of the optical and thermal behaviour of a PTC is presented. The new optical model developed in the previous chapter is coupled with a heat transfer model to calculate the heat losses and thermal performance of the PTC considering the energy flux distribution around the receiver. A thermal radiation analysis is carried out between the HCE and the surrounding to calculate the radiative heat losses. Adequate correlations have been selected carefully from the literature for the convective heat transfer losses. The heat collector element is discretised into several segments in both axial and azimuthal directions using the Finite Volume Method (FVM) and an energy balance is applied for each control volume. For the solar heat flux distribution around the HCE, the new numerical-geometrical method developed in the previous chapter has been applied. The partial differential equations were discretised by using the FVM and the set of non-linear algebraic equations were solved iteratively.

In order to validate the proposed numerical model, it was compared with experimental results obtained by Sandia National Laboratories [1] as well as un-irradiated receivers experiments [2].

3.2 PTC numerical model

The general modelling approach is based on an energy balance about the HCE. It includes the direct normal solar irradiation, the optical losses from both, the parabola and the HCE, the thermal losses from the HCE, and the gains in the HTF.

During a sunny day, the incident solar radiation is reflected by the mirrors and concentrated at the HCE. A small amount of this energy is absorbed by the glass envelope $\dot{q}_{g,s.rad}$ and the remaining is transmitted and absorbed by the absorber selective coating $\dot{q}_{a,s.rad}$. A part of the absorbed energy is transferred to the HTF by forced convection $\dot{q}_{a-f,conv}$ and the other part is returned to the glass envelope by natural convection $\dot{q}_{a-g,conv}$ and thermal radiation $\dot{q}_{a-g,t.rad}$. The energy coming from the absorber (convection and thermal radiation) pass through the glass envelope and

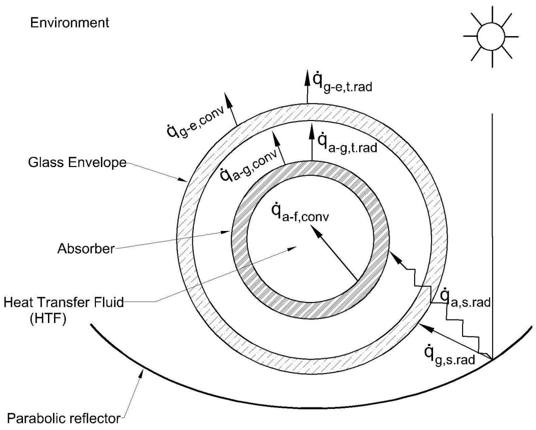

Figure 3.1: Heat transfer model in a cross section of the HCE (not to scale).

along with the absorbed energy by the the glass envelope, is lost to the environment by convection $\dot{q}_{g-e,conv}$ and thermal radiation $\dot{q}_{g-e,t.rad}$ (see Figure 3.1).

In this heat transfer model, an energy balance is applied over each component of the HCE. The energy equation in its integral form can be written as

$$\dot{\mathrm{Q}} - \dot{\mathrm{W}} = \int_{cs} \left(h + \frac{v^2}{2} + gz \right) \left(\rho \overrightarrow{v} \overrightarrow{dA} \right) + \frac{\partial}{\partial t} \int_{cv} \left(u + \frac{v^2}{2} + gz \right) (\rho dV) \tag{3.1}$$

The FVM is used to discretise the domain and apply the energy conservation at each control volume (CV) under steady state conditions. The HCE is divided into N_z CVs in the axial direction and N_θ CVs in the azimuthal direction. The HTF is only discretised in the longitudinal direction (see figure 3.2 a and b). Both, temperatures and heat fluxes, vary along the circumference and the length of the HCE except for the fluid which varies only along the length of the absorber. The temperature of the HTF is assumed to be uniform in the cross-section of the absorber tube where it is evaluated as the average fluid bluk temperature. The energy balance equations are determined by applying equation 3.1 at each CV as is shown hereafter.

For an i-th HTF CV, the energy balance equation can be expressed as (see figure 3.2 c)

$$\dot{q}^{i}_{a-f,conv} = \dot{m} \left[\hbar^{i}_{f} - \hbar^{i+1}_{f} \right] = \dot{m} C_p \left[T^{i}_{f} - T^{i+1}_{f} \right] \tag{3.2}$$

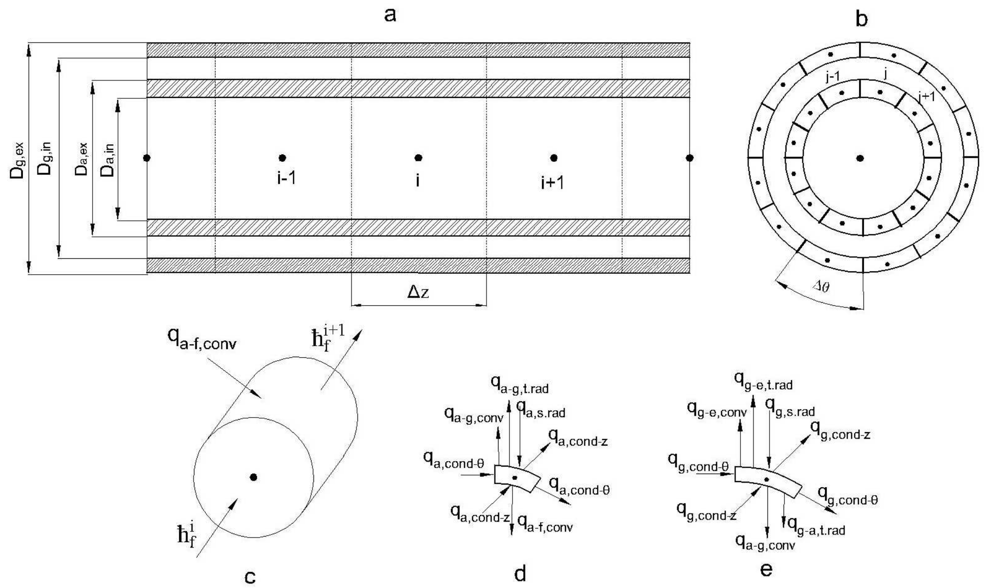

Figure 3.2: Longitudinal and azimuthal discretisation of the HCE: (a) longitudinal discretisation (b) azimuthal discretisation (c) HTF CV (d) absorber CV (e) glass envelope CV

For an absorber tube CV, the energy balance equation is given by (see figure 3.2 d)

$$\sum_{cv} \dot{q}^{ij} = \dot{q}_{a,cond} + \dot{q}^{ij}_{a,s.rad} - \dot{q}^{ij}_{a-g,conv} - \dot{q}^{ij}_{a-g,t.rad} - \dot{q}^{ij}_{a-f,conv} = 0 \tag{3.3}$$

where

$$\dot{q}_{a,cond} = \dot{q}^{ij}_{a,cond-z} - \dot{q}^{i+1j}_{a,cond-z} + \dot{q}^{ij}_{a,cond-\theta} - \dot{q}^{ij+1}_{a,cond-\theta} \tag{3.4}$$

In a similar way, the energy balance for a glass envelope tube CV can be obtained as follows (see figure 3.2 e)

$$\sum_{cv} \dot{q}^{ij} = \dot{q}_{g,cond} + \dot{q}^{ij}_{g-a,conv} + \dot{q}^{ij}_{g-a,t.rad} - \dot{q}^{ij}_{g-e,conv} - \dot{q}^{ij}_{g-e,t.rad} + \dot{q}^{ij}_{g-s.rad} = 0 \tag{3.5}$$

where

$$\dot{q}_{g,cond} = \dot{q}^{ij}_{g,cond-z} - \dot{q}^{i+1j}_{g,cond-z} + \dot{q}^{ij}_{g,cond-\theta} - \dot{q}^{ij+1}_{g,cond-\theta} \tag{3.6}$$

A detailed analysis of how each of these heat fluxes are determined is given hereafter.

3.2.1 Convection heat transfer between the HTF and the absorber

The convection heat transfer between the HTF and the absorber metal pipe is evaluated considering the convective heat flux from each absorber CV in the azimuthal direction as,

$$\dot{q}^{i}_{a-f,conv} = \sum_{j} h_f (T^{ij}_a - T^{i}_f) \frac{\pi D_{a,in}}{N_\theta} \tag{3.7}$$

where $h_f = \dfrac{Nu_{D_{a,in}} k}{D_{a,in}}$ is the HTF convection heat transfer coefficient at T^{ij}_a and is evaluated as a function of the Nusselt number $Nu_{D_{a,in}}$. Due to the lack of specific correlations in literature for evaluating the Nusselt number taking into account the temperature distribution of the absorber at each azimuthal CV, correlations for isothermal cylinders are considered. Specifically, the Gnielinski correlation [3] is used for turbulent and transitional flow ($Re > 3200$) in circular ducts, which reads,

$$Nu_{D_{a,in}} = \frac{(C/8)(Re_{D_{a,in}} - 1000)Pr}{1 + 12\sqrt{C/8}(Pr^{2/3} - 1)} \left(\frac{Pr}{Pr_w}\right)^{0.11} \tag{3.8}$$

with $C = (1.82log(Re_D) - 1.64)^{-2}$.

A study of the convection heat transfer between the HTF and the absorber with circumferentially varying thermal boundary conditions was also conducted (see Appendix B). This study is limited to sinuusoidal profile of temperature.

3.2.2 Conduction heat transfer through the absorber wall and the glass envelope

Heat conduction through the absorber wall and the glass cover is considered in the axial and azimuthal directions, whereas the heat conduction through the support brackets is neglected. The energy rate per unit length conducted across the azimuthal direction of a cylinder is defined as

$$\dot{q}_{cond-\theta} = -\frac{kdT}{rd\theta}e \tag{3.9}$$

where in the above expression e represents the thickness of either the absorber or glass envelope tube. In a similar manner, for the axial direction the conduction heat flux is defined as

$$\dot{q}_{cond-z} = -\frac{kdT}{dz}A_z \tag{3.10}$$

where A_z is the cross-section area of the CV. Both equations (3.9 and 3.10) are applied to the absorber and the glass envelope tubes taking into account the conductivity as a function of temperature of both materials.

3.2.3 Convection heat transfer between the absorber and the glass envelope

When the annular region is assumed as a perfect vacuum, the convection heat transfer can be ignored in the energy balance. However, in operational solar plants the vacuum condition in the annulus can change due to broken seals, hydrogen penetration and getter decomposition . In the present model, convection heat transfer $\dot{q}^{ij}_{a-g,conv}$ is calculated as follows,

$$\dot{q}^{ij}_{a-g,conv} = h_{an}(T^{ij}_a - T^{ij}_g)\frac{\pi D_{a,ex}}{N_\theta} \tag{3.11}$$

where h_{an} is calculated depending on free molecular convection or natural convection takes place.

When the HCE is under vacuum at low pressure ($P \simeq 0.013Pa$), free molecular convection occurs. The heat transfer coefficient is then evaluated as [4],

$$h_{an} = \frac{k_{std}}{[(D_{g,in}/2)ln(D_{g,in}/D_{a,ex}) + B\lambda(D_{a,ex}/D_{g,in} + 1)]} \quad (3.12)$$

$$b = \frac{(2-a)(9\gamma - 5)}{2a(\omega + 1)} \quad (3.13)$$

$$\lambda = \frac{2.331 \times 10^{-20} T^{ij}_{a-g}}{P_a \delta^2} \quad (3.14)$$

where T^{ij}_{a-g} the average temperature of the gas in the annulus $(T^{ij}_a + T^{ij}_g)/2$. The accommodation coefficient a depends on, either the gas surface arrangement or the level of contaminant gas layer absorbed on the surface and, varies between 0.01 to unity according to experimental studies [5]. In this study, the surface is assumed well cleaned and the accommodation coefficient is then fixed to one. When the vacuum is lost, natural convection within the annulus occurs. The heat transfer coefficient is then expressed with the Raithby and Holland's correlation [6] for natural convection in an annular space between horizontal cylinders,

$$h_{an} = \frac{2k_{eff}}{D_{a,ex} ln(D_{g,in}/D_{a,ex})} \quad (3.15)$$

$$k_{eff} = k(0.386)\left[\frac{Pr}{0.861 + Pr}\right]^{0.25} (Ra_c)^{0.25} \quad (3.16)$$

$$Ra_c = \frac{ln(D_{g,in}/D_{a,ex})^4}{L^3\left(D_{a,ex}^{-0.6} + D_{g,in}^{-0.6}\right)^5} Ra_L \quad (3.17)$$

being the effective thermal conductivity k_{eff} function of the thermophysical properties of the gas and the equivalent Rayleigh number Ra_c. This correlation is used for the range of $(10^2 \leq Ra_c \leq 10^7)$ and Ra_L is evaluated at the air gap distance $(D_{g,in} - D_{a,ex})/2$.

3.2.4 Thermal radiation heat transfer between the absorber and the glass envelope

The surfaces of the absorber and glass envelope are considered as grey and diffuse emitters and reflectors in the infrared band. The glass envelope is assumed to be opaque to the thermal radiation. The net radiation method [7] is applied to the cross section of the HCE in order to calculate $\dot{q}_{a-g,t.rad}$ as well as $\dot{q}_{g-a,t.rad}$ (equations 3.3 and 3.5). The effect of the axial direction is neglected. The Hottel's crossed-string

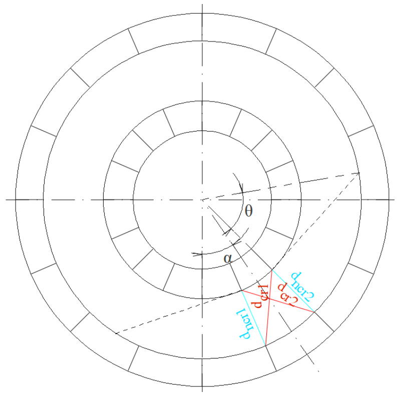

Figure 3.3: Geometric configuration for the View factor calculation

method [7] is used for calculating the view factors by connecting the faces of each tube and making sure that no visual obstruction remains between them.

In what follows, F_{ki}^{mn} is the view factor or shape factor from the surface of CV k at the material m to the surface of CV i at the material n. Since the absorber surface is convex, the view factor between any two CVs of the absorber tube is zero, $F_{ki}^{aa} = 0$. On the contrary, the view factors for the glass envelope, F_{ki}^{gg} are not null. They are calculated, all together with the view factors between the absorber and the glass envelope (F_{ki}^{ag} and F_{ki}^{ga}), using also the crossed-string method.

The limit angle that can see an absorber control volume is defined by $\theta = acos(\frac{r_{a,ex}}{r_{g,in}})$. The crossed distances between a fixed control volume in the receiver and a generic control volume 'i' of the glass envelope is defined by d_{cr1} and d_{cr2} as shown in figure (3.3).

Where $d_{cr1} = \sqrt{{r_{a,ex}}^2 + {r_{g,in}}^2 - 2r_{a,ex}r_{g,in}cos(\alpha[i] - (\frac{3\Delta\phi}{2}))}$.

$d_{cr2} = \sqrt{{r_{a,ex}}^2 + {r_{g,in}}^2 - 2r_{a,ex}r_{g,in}cos(\alpha[i] + \frac{\Delta\phi}{2})}$.

The no crossed distances between both control volumes is defined by d_{ncr1} and d_{ncr2}.

$d_{ncr1} = \sqrt{{r_{a,ex}}^2 + {r_{g,in}}^2 - 2r_{a,ex}r_{g,in}cos(\alpha[i] - (\frac{\Delta\phi}{2}))}$

$d_{ncr2} = \sqrt{{r_{a,ex}}^2 + {r_{g,in}}^2 - 2r_{a,ex}r_{g,in}cos(\alpha[i] - (\frac{\Delta\phi}{2}))}$

d_{cr2}, d_{ncr1} and d_{ncr2} should be modified when the other side of the glass envelope control volume exceeds θ to take into account the visible part.

The view factor between a receiver control volume and a glass envelope control volume may be expressed according to the crossed-string method as

$$F^{ag}_{ki} = \frac{d_{cr1} + d_{cr2} - d_{ncr1} - d_{ncr2}}{2 r_{a,ex} \Delta\phi} \tag{3.18}$$

F^{ga}_{ki} may be calculated according to law of reciprocity.

$$F^{ga}_{ki} = \frac{r_{a,ex}}{r_{g,in}} F^{ag}_{ki} \tag{3.19}$$

The thermal radiative heat flux leaving the j-th absorber CV is expressed by

$$\begin{aligned} \dot{q}^{ij}_{a-g,t.rad} &= \dot{q}^{j}_{a,t.rad} = (J^j_a - H^j_a) = \epsilon_a \left[\sigma {T^j_a}^4 - H^j_a \right] \\ &= \epsilon_a \left[\sigma {T^j_a}^4 - \sum_l (F^{ag}_{jl} J^l_g) \right] \end{aligned} \tag{3.20}$$

The thermal radiation gained by a glass envelope CV j is given by

$$\begin{aligned} \dot{q}^{ij}_{g-a,t.rad} &= \dot{q}^{j}_{g,t.rad} = (J^j_g - H^j_g) = \epsilon_g \left[\sigma {T^j_g}^4 - H^j_g \right] \\ &= \epsilon_g \left[\sigma {T^j_g}^4 - \sum_k (F^{ga}_{jk} J^k_a) - \sum_r (F^{gg}_{jr} J^r_g) \right] \end{aligned} \tag{3.21}$$

The total thermal radiative energy leaving the absorber tube is calculated by integrating the radiative heat flux around the absorber.

$$\dot{q}_{a-g,t.rad} = \sum_j^{N_\theta} \dot{q}^j_{a,t.rad} \tag{3.22}$$

The calculation of the view factor for the glass envelope is also carried out using the crossed-string method. First, the view factor of the same control volume is calculated F^{gg}_{ii} and then the view factor between two generic glass envelope control volumes F^{gg}_{ki}.

F^{gg}_{ii} is determined by supposing an imaginary surface that covers the control volume and using the summation and reciprocity laws.

$$F^{gg}_{ii} = (1 - \frac{\sqrt{2 {r_{g,in}}^2 (1 - cos(\Delta\phi))}}{r_{g,in} \Delta\phi}) \tag{3.23}$$

For the the view factor between two generic glass envelope control volumes, a similar procedure to the evaluation of F_{ag} has been used by calculating the crossed and

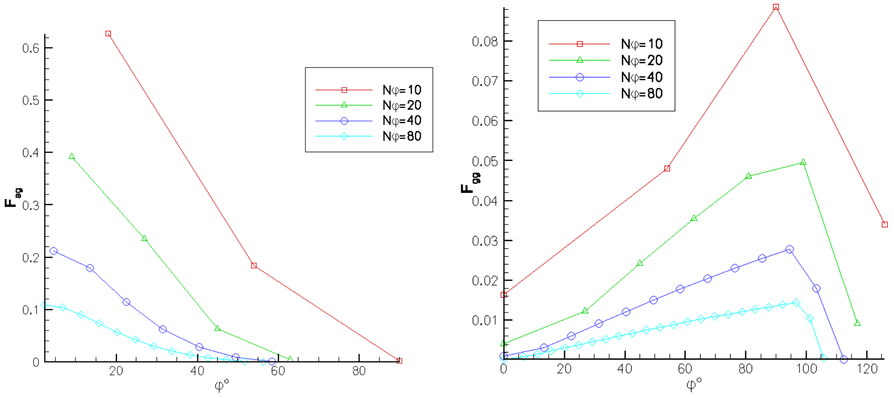

(a) (b)

Figure 3.4: View Factors for different azimuthal discretisations (a) F_{ag} (b)F_{gg}

no-crossed distances between two control volumes.
$d_{cr1} = \sqrt{2{r_{g,in}}^2(1 - cos(\alpha[i] - \frac{\Delta\phi}{2}))}$
$d_{cr2} = \sqrt{(2{r_{g,in}}^2 - 2{r_{g,in}}^2 cos(\alpha[i] - \frac{\Delta\phi}{2}))}$
$d_{ncr1} = \sqrt{(2{r_{g,in}}^2 - 2{r_{g,in}}^2 cos(\alpha[i] + \frac{\Delta\phi}{2}))}$
$d_{ncr2} = \sqrt{(2{r_{g,in}}^2(1 - cos(\alpha[i] - \frac{3\Delta\phi}{2})))}$
Of course, these distances should be changed in the case when the receiver tube make a visual obstruction between both control volumes.
The view factor F_{ki}^{gg} is given by

$$F_{ki}^{gg} = \frac{d_{cr1} + d_{cr2} - d_{ncr1} - d_{ncr2}}{2r_{g,in}\Delta\phi} \tag{3.24}$$

In a similar way, the total thermal radiative energy gained by the glass envelope is calculated as

$$\dot{q}_{g-a,t.rad} = \sum_{j}^{N_\theta} \dot{q}_{g,t.rad}^{j} \tag{3.25}$$

Figure 3.4 shows the view factors F_{ag} and F_{gg} around the circumference of the receiver for different number of n_ϕ. Both curves (a and b) present only one half of the view factors as they are symmetric around the node in question. The results of figure 3.4(a) show that view factor F_{ag} decreases away from the opposite control volume as well as when the number of control volumes increases. However, the view factors F_{gg} increase away from the i-th control volume but it decreases when the receiver tube starts to hide the opposite part of the glass envelope. It decreases also when the control volume increases.

3.2.5 Convection heat transfer from the glass envelope to the environment

The convection heat transfer from the glass envelope to the ambient is computed as

$$\dot{q}^{ij}_{g-e,conv} = h_e(T^{ij}_g - T_{amb})\frac{\pi D_{g,ex}}{N_\theta} \tag{3.26}$$

The heat transfer coefficient, h_e, is evaluated depending on whether the convection is natural or forced. After comparing different empirical correlations presented in the technical literature, the ones indicated hereafter are selected as they work better for the conditions under study. Thus, for natural convection the correlation developed by Churchill and Chu [8] for horizontal cylinders for the calculation of the average Nusselt number is recommended.

$$Nu_{D_{g,ex}} = \left[0.6 + 0.387\left(\frac{Ra_{D_{g,ex}}}{\left(1+(0.559/Pr)^{9/16}\right)^{16/9}}\right)^{1/6}\right]^2 \tag{3.27}$$

If the PTC is supposed to work exposed to wind conditions, i.e., under forced convection, then the convection heat transfer coefficient is determined using the correlation of Churchill and Bernstein [9] for a cylinder in cross flow. This equation is recommended to be used for all $Re_{D_{g,ex}}Pr > 0.2$.

$$Nu_{D_{g,ex}} = 0.3 + \frac{0.62 Re^{0.5}_{D_{g,ex}} Pr^{1/3}}{\left[1+(0.4/Pr)^{2/3}\right]^{1/4}}\left[1+\left(\frac{Re_{D_{g,ex}}}{282000}\right)^{5/8}\right]^{4/5} \tag{3.28}$$

3.2.6 Thermal radiation heat transfer between the glass envelope and the surrounding

The glass envelope is surrounded by the collector parabola and the sky. Thus, thermal radiation heat transfer must consider the radiation exchange with both. In the present model, the glass envelope is assumed to be a small convex grey object and the sky as a large black body cavity ($\epsilon_s = 1$) at temperature T_s. The collector parabola surface is considered diffuse and opaque to the thermal radiation. The view factors are determined using the crossed-string method, similar to the treatment in section 3.2.4. According to the geometry of the problem, a limit angle that can be seen by the parabola may be defined as $\theta = acos\left(\frac{r_{g,ex}}{\sqrt{\frac{A_w}{2}^2+(f-\frac{A_w^2}{16f})^2}}\right)$. Where A_w is the aperture and f is the focal distance. The crossed and no crossed distances between the parabolic collector and a generic glass envelope control volume are given by the following equations.

$$d_{cr1} = \sqrt{A_w^2 + \frac{A_w^2}{16f}^2 + r_{g,ex}^2 - 2r_{g,ex}\sqrt{0.5A_w^2 + \frac{A_w^2}{16f}^2} cos(\theta_{rim} + \alpha[k] + \frac{\Delta\phi}{2})}$$

$$d_{cr2} = \sqrt{A_w^2 + \frac{A_w^2}{16f}^2 + r_{g,ex}^2 - 2r_{g,ex}\sqrt{0.5A_w^2 + \frac{A_w^2}{16f}^2} cos(\theta_{rim} - \alpha[k] + \frac{\Delta\phi}{2})}$$

$$d_{ncr1} = \sqrt{A_w^2 + \frac{A_w^2}{16f}^2 + r_{g,ex}^2 - 2r_{g,ex}\sqrt{0.5A_w^2 + \frac{A_w^2}{16f}^2} cos(\theta_{rim} + \alpha[k] - \frac{\Delta\phi}{2})}$$

$$d_{ncr2} = \sqrt{A_w^2 + \frac{A_w^2}{16f}^2 + r_{g,ex}^2 - 2r_{g,ex}\sqrt{0.5A_w^2 + \frac{A_w^2}{16f}^2} cos(\theta_{rim} - \alpha[k] - \frac{\Delta\phi}{2})}$$

Where θ_{rim} is the rim angle of the parabola. All these distances should be modified to take into account the limit angle for the shadowed control volumes.
The view factor between a glass envelope control volume and the parabolic collector is given by

$$F_k^{gc} = \frac{d_{cr1} + d_{cr2} - d_{ncr1} - d_{ncr2}}{2r_{g,ex}\Delta\phi} \tag{3.29}$$

Hence, the view factor between the glass envelope and the sky can be deduced according to the summation law as

$$F_k^{gs} = 1 - F_k^{gc} \tag{3.30}$$

Figure (3.5) shows the view factor F_{gc} calculated for different azimuthal discretisations around the glass envelope. This figure is similar to figure (3.4(a)) and the view factors decrease by going away form the opposite control volume from the parabola.

$$\begin{aligned} \dot{q}^{ij}_{g-e,t.rad} = \dot{q}^{j}_{g,t.rad} = (J_g^i - H_g^i) \quad &= \quad \epsilon_g[\sigma {T_g^i}^4 - H_g^i] \\ &= \quad \epsilon_g\left[\sigma {T_g^i}^4 - \sum_k (F_k^{gc} J_c + F_k^{gs} J_s)\right] \end{aligned} \tag{3.31}$$

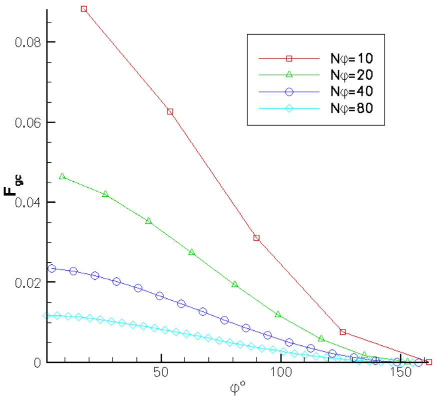

Figure 3.5: View factors for different azimuthal discretisations F_{gc}

where $j_c = \epsilon_c \sigma T_c^4$ and $J_s = \sigma T_s^4$. The thermal radiative heat energy lost to the environment is then calculated by integrating the radiative flux around the glass envelope.

$$\dot{q}_{g-e,t.rad} = \sum_{j}^{N_\theta} \dot{q}^{j}_{g,t.rad} \tag{3.32}$$

3.2.7 Solar irradiation absorption

The solar irradiation absorption and the optical efficiency are important parameters for the calculation of the heat transfer around the HCE. Both of the absorber and glass envelope tubes are discretized in the azimuthal direction and solar irradiation absorption is evaluated at each CV. The solar heat flux distribution depends only on the azimuthal direction as it is homogeneous in the longitudinal direction. Initially, the FVM developed in chapter 2 has been used to evaluate the solar radiation flux distribution (see Appendix C). Because of the limitations of this method, the new optical model developed in this thesis (see previous chapter) has been used to determine the solar irradiation absorbed by the absorber tube and the glass envelope. The same methodology described in section 2.5 is followed. The solar energy absorbed by the j-th CV of the absorber and the glass envelope is calculated by integrating the direct solar radiation that reaches each tube (without concentration) and the reflected incident solar radiation that hits them, i.e. $\dot{q}^{j}_{a,s.rad}$ and $\dot{q}^{j}_{g,s.rad}$. The total energy absorbed on the absorber tube and the glass envelope are obtained by summing the absorbed solar flux over all the CVs.

$$q_{a,s.rad} = \left((W - D_a)\rho_s + D_a\right)(\tau\alpha)I_{inc} \tag{3.33}$$

$$q_{g,s.rad} = \left((W - D_g)\rho_s + D_g\right)(1 - (\tau\alpha))I_{inc} \tag{3.34}$$

Where I_{inc} is the direct incident radiation per unit of aperture (W/m).

3.3 Numerical Solution

As commented in the previous section, the numerical analysis is carried out by using the FVM under steady state conditions. For the fluid inside the absorber, a single phase (liquid) incompressible flow is assumed. The energy balance equations (equations 3.2, 3.3 and 3.5) result in a set of non-linear algebraic equations where temperatures and heat fluxes are coupled and solved using an iterative procedure. The solar radiative heat flux (equations 2.37 and 2.38) is determined as a pre-processing task. This flux is added to the balance energy model as a boundary condition for the outer surface of the absorber/glass tube by assuming the solar absorption as surface phenomenon because of the small thickness of the surface layer over which absorption is taking place [7].

For a HTF control volume, the temperature values are obtained from the 1D discretised equations by using the known values at the inlet section and the wall boundary conditions. A high-order numerical scheme (SMART) [10] is used to calculate the temperature at the faces of the CVs. The set of algebraic equations are then solved by a direct solver (TDMA) in the longitudinal tube direction.

For the absorber tube and the glass envelope, a central difference scheme is used in the discretisation process. The linear algebraic equations obtained from the discretisation of the governing equations in the absorber and the glass envelope are implemented with the corresponding boundary conditions and then solved using a direct solver based on LU decomposition.

The general algorithm, as can be seen in Figure 3.6, is divided in two steps: the pre-processing calculation of the concentrated solar flux distribution (the optical model) and the thermal model for resolving the energy balance at the HCE. The optical model is based on the methodology described in the previous chapter (see section 2.5). A new numerical-geometrical method have been used to calculate the distribution of the solar flux around the HCE.

After the spatial and angular discretisation of the domain, the optic cone is projected on the HCE in order to quantify the reflected rays and calculate the solar radiative heat flux.

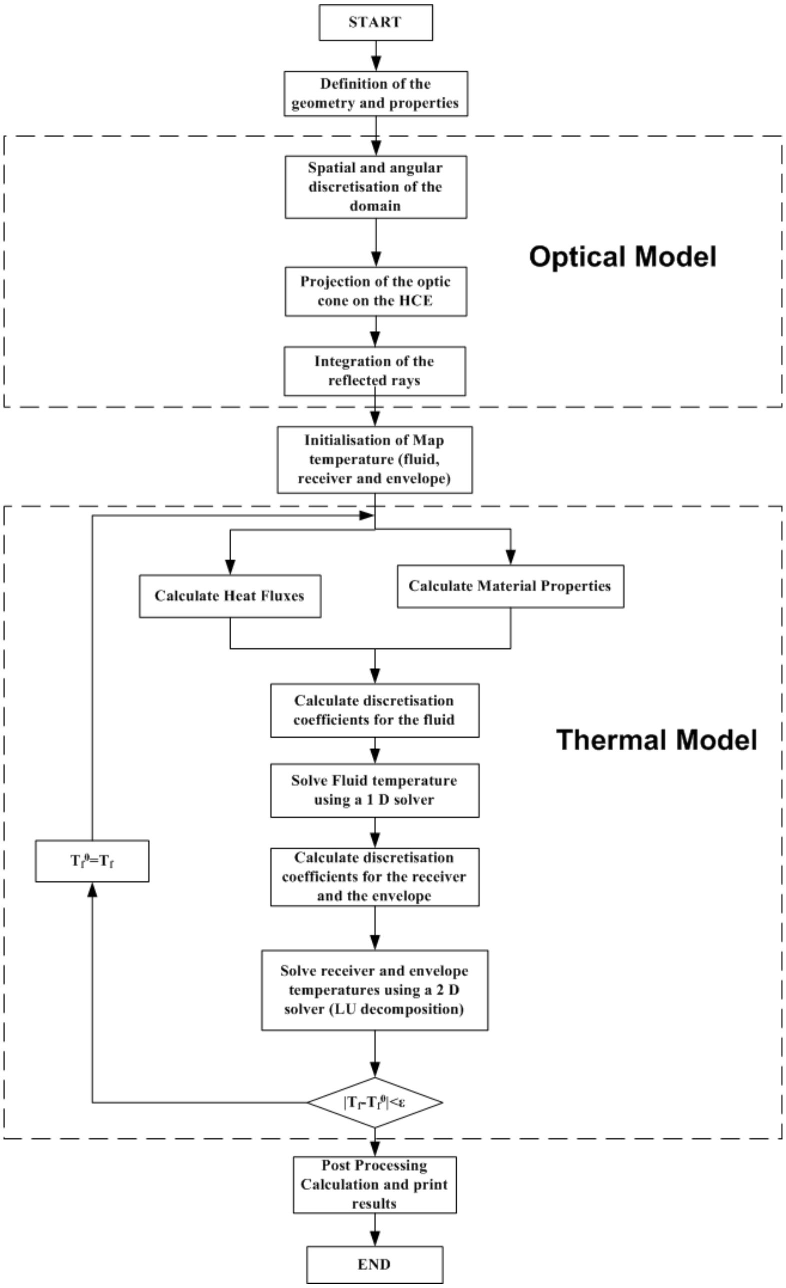

Figure 3.6: Flow chart of the general algorithm

The thermal model starts by initialising the temperature maps for the different components of the HCE, i.e. the fluid, the absorber tube and the glass envelope tube. All the heat fluxes and material properties have to be calculated and inserted into the discretised energy equations. These equations are then solved numerically using the appropriate numerical scheme and direct solver as described before. The coupling between the energy equations is performed iteratively. The global convergence is reached when the temperature of fluid T_f becomes stable and a strict convergence criterion is verified $|T_f - T_f^0| < \varepsilon$, where T_f^0 is the temperature of fluid in the previous iteration and $\varepsilon = 10^{-6}$. The energy balance model provides the temperature distribution in the HCE, as well as, the performance of a PTC by calculating the useful energy, the thermal losses and the thermal efficiency. The PTC thermal efficiency is determined as,

$$\eta_{th} = \frac{q_u}{A_w I_{s.inc}} \tag{3.35}$$

The useful energy is obtained by summing the heat gained by the HTF along the absorber. Thus,

$$q_u = \sum_{i}^{N_z} \sum_{j}^{N_\theta} \dot{q}_{a-f,conv}^{ij} \tag{3.36}$$

The heat losses are the sum of the convective and the thermal radiative flux lost by the absorber tube.

$$q_{heat\,loss} = \sum_{i}^{N_z} \sum_{j}^{N_\theta} (\dot{q}_{a-g,conv}^{ij} - \dot{q}_{a-g,rad}^{ij}) \tag{3.37}$$

3.4 Computational results and validation

Both optical models have been tested and compared to numerical data from literature in the previous chapter. The accuracy of the overall model, i.e. the optical model coupled with the thermal model, is also tested.

The thermal model is validated by comparing the results with experimental measurements obtained by Sandia National Laboratories for a collector assembly (LS-2) placed in the AZTRAK rotating platform [1]. The comparisons are carried out under different working conditions which are summarised in table 3.1 for a silicone HTF (syltherm 800).

In the numerical model, different numbers of longitudinal control volumes are tested to get a grid-independent solution. The grid $N_z \times N_\theta = 60 \times 60$, is considered

Table 3.1: Experimental conditions data from [1] used in the thermal model validation

Parameter	Value
Selective coatings	Cermet- Black chrome
Incident solar irradiation	755 - 982.3 W/m^2
Wind Speed	0.0 - 5.5 m/s
Flow rate	(7.95 - 9.46) $\times 10^{-4} m^3/s$
Air Temperature	267.95 - 304.85 K
Input Temperature	317.85 - 649.75 K

as grid-independent since there is no significant difference in the results for finer discretisations.

Comparisons are performed for irradiated and un-irradiated absorbers and two scenarios of the annulus: *i)* vacuum and *ii)* air between the absorber and the glass envelope. The experimental tests reported at zero incident angle are used for this comparison.

The comparison of the performance against the experimental data is shown in Figures (3.7-3.8). The results for the thermal losses and the thermal efficiency of the PTC follow the same trends of the experiments and the agreement here is good. The results are within the experimental uncertainty. For the cermet selective coating, the maximum error of thermal efficiency is 3.16 % with a mean deviation of less than 1.28 %. For the black chrome selective coating, the maximum error of thermal efficiency is 3.29 % with a mean deviation of less than 1.39 %. The increment of temperature of the fluid ($\Delta T = T_{out} - T_{in}$) was also compared with measurements and the differences are quite small. The maximum deviation are smaller than 7.2 % with mean deviation of not more than 4.94 %. Table 3.2 summarizes the error analysis for both selective coatings and different scenarios.

As it was expected, heat losses increase with the fluid temperature due to the convection, conduction, and thermal radiation losses in the annulus for both cases (air and vacuum), which cause the drop of efficiency. Moreover, the heat losses increase and the efficiency of the collector is degraded when allowing air into annulus, as well as for the use of black chrome coating, which has worse radiative properties (high emittance) than the cermet coating.

The discrepancies between the present results and the experimental measurements seem to increase with the temperature of the HTF. This can be explained by the optical properties of the HCE, which are based at lower temperatures. In addition, other unaccounted optical effects during the test operating [11], such as HCE and

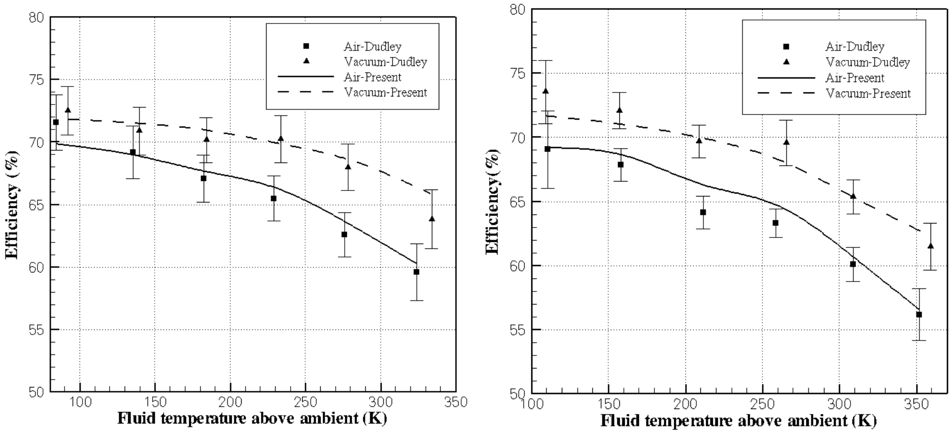

(a) (b)

Figure 3.7: Thermal efficiency comparison between Sandia experimental data and proposed model (a) cermet coating (b)black chrome coating

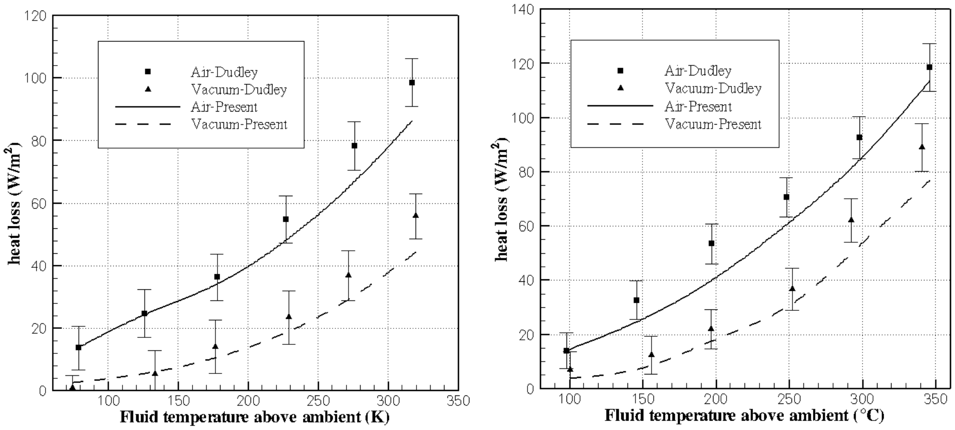

(a) (b)

Figure 3.8: Thermal losses comparison between Sandia experimental data and proposed model for un-irradiated case (a) cermet coating (b)black chrome coating

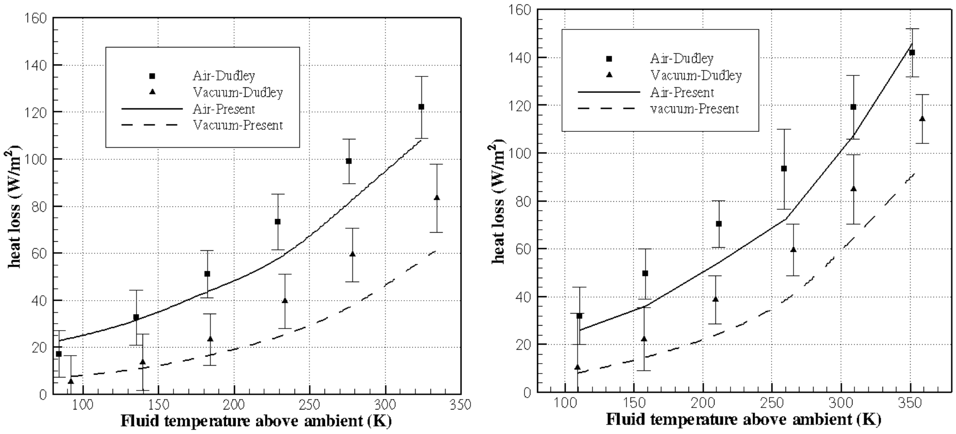

(a) (b)

Figure 3.9: Thermal losses comparison between Sandia experimental data and proposed model for irradiated case (a) cermet coating (b)black chrome coating

Table 3.2: Error analysis of thermal efficiency and increment of HTF temperature for irradiated case and both selective coatings (cermet and black chrome)

Selective coating	Scenario	Thermal efficiency		ΔT	
		Max error (%)	Mean error (%)	Max error (%)	Mean error (%)
Cermet	Air	2.42	1.28	5.52	3.94
	Vacuum	3.17	1.25	6.28	4.25
Black chrome	Air	3.29	1.39	7.2	4.94
	Vacuum	2.57	1.35	4.7	3.07

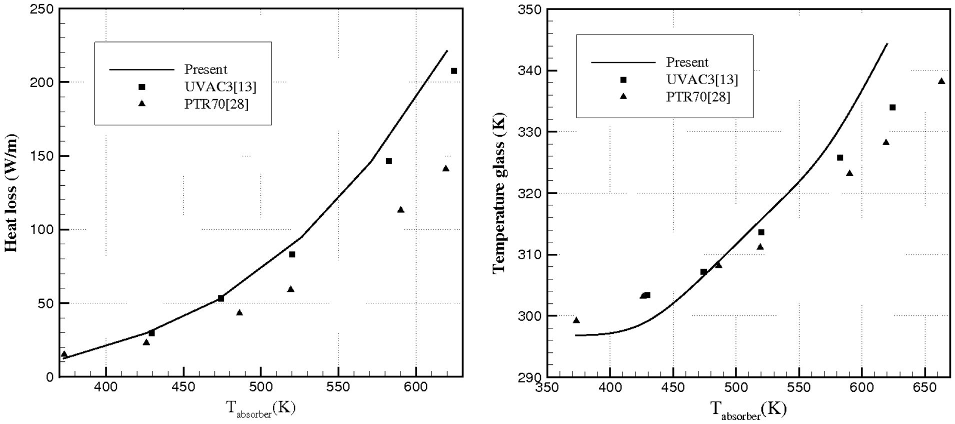

(a) (b)

Figure 3.10: Comparisons with un-irradiated absorbers experiments (a) heat losses and (b) glass temperature

mirror alignment, aberration in mirrors and tracking system errors are also causes of the discrepancies. Another source of errors might be the empirical correlations used for the heat transfer coefficients. In the present work, correlations for a cylinder in cross-flow are used, but when the PTC works under wind conditions, the presence of the parabolic mirror affects the heat transfer around the HCE [12, 13]. Further work is required for obtaining appropriate correlations for such situations.

The numerical model is also validated with more recent experimental measurements of heat losses which are performed in un-irradiated absorbers [2, 14]. The experiments are done indoors using a HCE with the same dimensions as in table 2.1, an ambient temperature of about 296K and the flow rate is changed to obtain the desired absorber temperature. The advantage of this validation is that these experiments are performed inside the laboratory under controlled ambient which can affect the convection heat transfer with environment as well as the optical errors in the PTC.

In these simulations, the thermal emittance of UVAC3 [2] is used. Although, in the experimental measurements of PTR70 [14] the emittance was different from UVAC3 [2], these results are also plotted just as a reference to illustrate the trend. Figure 3.10(a) shows the heat losses from un-irradiated absorbers and the comparison with both experimental measurements. It can be seen from the figure, that the present model reproduces the behaviour of UVAC3 HCE reasonably well with a maximum deviation in glass temperature of 3.9 % and deviations in heat loss smaller than 12 %. The predicted results also follow the same trend of PTR70 HCE. The heat losses in un-irradiated absorbers are dominated by thermal radiation and the heat transfer coefficient to the environment corresponds to natural convection (no winds). As can be seen, the current model accurately predicts heat losses and gives better agreement than the previous heat losses validation with Sandia experiments [1]. Figure 3.10(b) shows the variation of the glass temperature respect to the absorber temperature and the comparison with experimental tests. The main reason of the difference encountered in glass temperature is due to the variation of the optical properties with temperature as well as the effect of anti-reflective coating applied to the glass which is not included in the present model. A possible under-prediction of the convection heat transfer coefficient may be the cause of the over-prediction of the glass temperature at high operating temperature.

Finally, the case of Dudley et al. [1] ($I_b = 933.7 W/m^2$, $\dot{m} = 0.68\ kg/s$, $T_{air} = 294.35\ K$ and $T_{in} = 375.35\ K$) has been tested. The results of the thermal behaviour around the circumference of the HCE are presented in Figures (3.11-3.12). The temperature profile of both absorber and glass envelope follows the non-uniform solar heat flux distribution which indicates that the conduction in both tubes is relatively small. The temperature of the absorber is symmetric and increases by moving along the HCE far away from the inlet. The four zones discussed in the distribution of the LCR are also present in the temperature distribution of both tubes. The temperature at the inlet of the absorber is close to the temperature of the un-irradiated absorber in the direct radiation zone where the solar flux is not concentrated.

The temperature of the absorber increases along the axial direction as shown in Figure 3.12 for different azimuthal positions (0°, 90° and 180°) and follows the same trend as the numerical results of Cheng et al. [15]. The absorber temperature is higher at 180° because the absorber receives more concentrated solar radiation at this angular position, while at 0° is the lowest one because there is no solar concentration in this position.

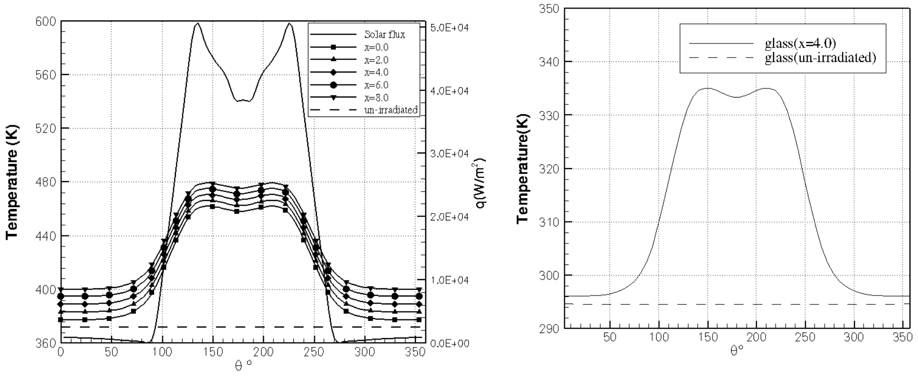

(a)

(b)

Figure 3.11: Circumferential temperature distribution on (a) the absorber tube for several longitudinal positions (b) the glass cover for x=4.0m

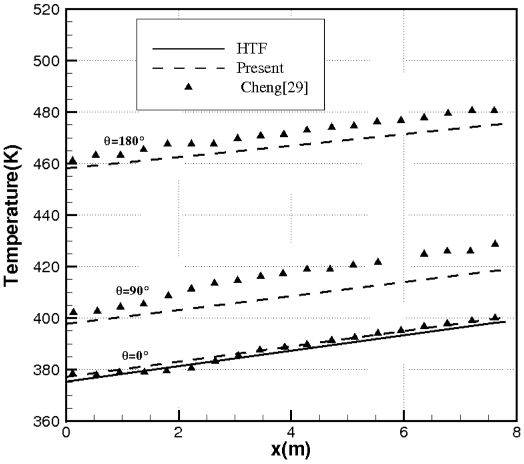

Figure 3.12: Variation of the temperature of the absorber tube and the HTF along the axial direction

3.5 Conclusions

A detailed numerical model based on energy balance about the HCE for the optical and thermal analysis of PTC has been developed. The proposed model included a detailed thermal radiative heat transfer analysis based on the crossed-string method. Different empirical correlations have been tested and selected according to the conditions under study. A FVM method for resolving the RTE and a new numerical-geometric method based on ray trace and FVM techniques are developed for calculating the non-uniform solar flux around the HCE. The validation of the optical model with available analytical results from the literature in the previous chapter has shown a quite good agreement. After the validation of the optical model, the overall thermal model is compared with the experimental measurements from Sandia National Laboratories [1]. Results obtained matched experimental ones, although some discrepancies are observed at higher temperatures. These discrepancies might be attributed to optical properties of the HCE, other unaccounted optical effects during the test operating, and possible errors due to correlations used for the heat transfer coefficients. Further validation is carried out by comparing the results of the thermal model with experimental measurements of un-irradiated receivers. It is shown that the present model is capable of estimating reasonably well the heat losses and temperature in the HCE. In addition to that, the overall model is tested for a given case of Dudley et al. [1] to study the thermal behaviour around the circumference of the HCE. The effect of the non-uniform incident solar radiation on the absorber tube and glass envelope was discussed. According to the results obtained, it can be concluded that the current numerical model is suitable for predicting the optical and thermal behaviour of the HCE under different operating conditions. The next chapter is dedicated to determine the effect of the non uniformity solar flux distribution in the convective heat losses to the ambient and taking into account the angle attack of the wind.

References

[1] V. Dudley, G. Kolb, M. Sloan, and D. Kearney. SEGS LS2 solar collector-test results. Technical report, Report of Sandia National Laboratories (SANDIA-94-1884), 1994.

[2] F. Burkholder and C. Kutscher. Heat-loss testing of Solel's UVAC3 parabolic trough receiver. Technical Report NREL/TP-550-42394, National Renewable Energy Laboratory, 2008.

[3] V. Gnielinski. New equations for heat and mass transfer in turbulent pipe and channel flow. *International Chemical Engineering*, 16(2):359–363, 1976.

[4] A. Ratzel, C. Hickox, and D. Gartling. Techniques for reducing thermal conduction and natural convection heat losses in annular receiver geometries. *Journal of Heat Transfer*, 101:108–113, 1979.

[5] S.C. Saxena and R.K. Joshi. *Thermal Accommodation and Adsorption Coefficients of Gases (CINDAS Data Series on Material Properties)*. Taylor & Francis, 1989.

[6] G.D. Raithby and K.G.T. Hollands. A general method of obtaining approximate solutions to laminar and turbulent free convection problems. *Advances in Heat Transfer*, 11:265–315, 1975.

[7] M.F. Modest. *Radiative heat transfer*. Academic Press, 2003.

[8] S.W Churchill and H.H.S Chu. Correlating equations for laminar and turbulent free convection from a horizontal cylinder. *International Journal of Heat and Mass Transfer*, 18(9):1049–1053, 1975.

[9] S.W Churchill and M Bernstein. A correlating equation for forced convection from gases and liquids to a circular cylinder in crossflow. *Journal of Heat Transfer*, 99:300–306, 1977.

[10] P.H. Gaskell and A.K.C. Lau. Curvatue-compensated convective transport: SMART, a new boundedness-preserving transport algorithm. *International Journal Numerical Methods Fluids*, 8(6):617–641, 1988.

[11] R. Foristall. Heat transfer analysis and modeling of aparabolic trough solar receiver implemented in engineering equation solver. Technical report, National Renewable Energy Laboratory(NREL), 2003.

[12] N. Naeeni and M. Yaghoubi. Analysis of wind flow around a parabolic collector (1) fluid flow. *Renewable Energy*, 32(11):1898–1916, 2007.

[13] N. Naeeni and M. Yaghoubi. Analysis of wind flow around a parabolic collector (2) fluid flow. *Renewable Energy*, 32(11):1259–1272, 2007.

[14] F. Burkholder and C. Kutscher. Heat loss testing of Schoot's 2008 PTR70 parabolic trough receiver. Technical Report NREL/TP-550-45633, National Renewable Energy Laboratory, 2009.

[15] Z.D. Cheng, Y.L. He, J. Xiao, Y.B. Tao, and R.J. Xu. Three-dimensional numerical study of heat transfer characteristics in the receiver tube of parabolic trough solar collector. *International Communications in Heat and Mass Transfer*, 37(7): 782–787, 2010.

Chapter 4

Numerical simulation of wind flow around a parabolic trough solar collector

Most of the contents of this chapter have been published as:
A.A. Hachicha, I. Rodríguez, J. Castro and A. Oliva. Numerical simulation of wind flow around a parabolic trough solar collector. *Applied Energy* 107 , pp. 426-437.

Abstract.

The use of parabolic trough solar technology in solar power plants has been increased in recent years. Such devices are located in open terrain and can be the subject of strong winds. As a result, the stability of these devices to track accurately the sun and the convection heat transfer from the receiver tube could be affected. A detailed numerical aerodynamic and heat transfer model based on Large Eddy Simulations (LES) modelling for these equipments is presented. First, the model is verified on a circular cylinder in a cross flow. The drag forces and the heat transfer coefficients are then validated with available experimental measurements. After that, simulations are performed on an Eurotrough solar collector to study the fluid flow and heat transfer around the solar collector and its receiver. Computations are carried out for a Reynolds number of $Re_W = 3.6 \times 10^5$ (based on the aperture) and for various pitch angles ($\theta = 0^\circ, 45^\circ, 90^\circ, 135^\circ, 180^\circ, 270^\circ$). The aerodynamic coefficients are calculated around the solar collector and validated with measurements performed in wind tunnel tests. Instantaneous velocity field is also studied and compared to aerodynamic coefficients for different pitch angles. The time-averaged flow is characterised by the formation of several recirculation regions around the solar collector and the receiver tube depending on the pitch angle. The study also presents a comparative study of the heat transfer coefficients around the heat collector element with the circular cylinder in a cross flow and the effect of the pitch angle on the Nusselt number.

4.1 Introduction

Parabolic trough solar collectors (PTC) constitute a proven device of thermal energy for industrial process heat and power generation. Currently, PTC is one of the most mature and prominent technologies for solar energy for production of electricity. The majority of the parabolic trough plants deployed operate at temperatures up to 400 Â°C using synthetic oil as heat transfer fluid (HTF)[1]. Parabolic trough collectors are built in modules that are supported from the ground by simple pedestals at either end. A PTC is basically constructed as a long parabolic trough-shaped mirror that reflects direct solar radiation and concentrates it onto a heat collector element (HCE) located in the focal line of the parabola. The HTF runs through the receiver tube and absorbs the concentrated sunlight. The surface of the absorber is covered with a selective coating which has a high absorptance for solar radiation and low emittance for thermal radiation. A glass envelope is used around the absorber tube to reduce the convective heat losses with vacuum in the space between the absorber and the glass cover. The PTC is aligned to the north-south axis and tracks the Sun from east to west as it moves across the sky using a tracking mechanism system.

In practice, the array field of solar collectors is located in an open terrain and it is sensitive to strong winds [2]. The surrounding air is usually turbulent and can affect the optical performance and wind resistance of the PTC, as well as, the heat exchange between the glass outer surface and the ambient air. Wind flow analysis is then required to understand the aerodynamic loading around the parabolic reflector, as well as, the convection heat transfer from the HCE.

Several numerical and experimental studies have been performed to determine the thermal performance and heat transfer characteristics of PTC [3, 4, 5, 6, 7]. However, only few studies of wind flow around the PTC have been published as commented in section 1.3 and numerical studies are rare. Up to now, the turbulence modelling of the fluid flow and heat transfer around the PTC has been solved using RANS models which suffer from inaccuracies in predictions of flow with massive separations and vortex shedding [8, 9]. The lack of precision of RANS models in these situations and the increase of computer power, together with the emergence of new high-efficiency sparse parallel algorithms, motivated the use of more accurate turbulent models such as Large Eddy Simulation models (LES). In LES, the largest scales of the flow are solved and requires modelling only for the smallest ones, while RANS models are focused on the mean flow and the effects of turbulence on mean flow properties.

In the present work, detailed numerical simulations based on LES modelling of the flow field and heat transfer around a full-scale parabolic trough solar collector are presented. The main objectives of this study are to demonstrate the capabilities of LES models for quantifying the fluid flow and the aerodynamic coefficients for various pitch angles, as well as, to identify the recirculation zone and vortex-shedding around the PTC and the HCE The thermal field and convection heat transfer around the HCE are also determined.

4.2 PTC numerical model

4.2.1 Mathematical model

The methodology used for solving the fluid flow and heat transfer around the PTC is similar to that of bluff body flow described in [10]. In this context, LES models have been proven to yield accurate results in flows with massive separations, reattachments and recirculations and they have been widely tested to simulate turbulent flow around obstacles [11, 12, 13, 14].

All the simulations are carried out using the CFD&HT code Termofluids [15], which is an unstructured and parallel object-oriented code for solving industrial flows. In Termofluids, the incompressible filtered Navier-Stokes and energy equations are written as

$$\begin{aligned} \nabla \cdot \overline{\boldsymbol{u}} &= \boldsymbol{0} && (4.1) \\ \frac{\partial \overline{\boldsymbol{u}}}{\partial t} + (\overline{u} \cdot \nabla)\overline{\boldsymbol{u}} - \nu \nabla^2 \overline{\boldsymbol{u}} + \rho^{-1} \nabla \overline{\boldsymbol{p}} + \overline{\boldsymbol{\mathcal{F}}} &= (\overline{u} \cdot \nabla)\overline{\boldsymbol{u}} - \overline{\mathsf{C}\,(\boldsymbol{u})\,\boldsymbol{u}} && \\ &\approx \nabla \cdot \tau && (4.2) \\ \frac{\partial \overline{\boldsymbol{T}}}{\partial t} + (\overline{u} \cdot \nabla)\overline{\boldsymbol{T}} - \kappa \nabla^2 \overline{\boldsymbol{T}} &= (\overline{u} \cdot \nabla)\overline{\boldsymbol{T}} - \overline{\mathsf{C}\,(\boldsymbol{u})\,\boldsymbol{T}} && \\ &\approx \nabla \cdot \tau_T && (4.3) \end{aligned}$$

where $\overline{\boldsymbol{u}}$, $\overline{\boldsymbol{p}}$, $\overline{\boldsymbol{T}}$ denote the filtered velocity vector, pressure and temperature fields respectively. ν , ρ and κ are the viscosity, density and thermal diffusivity. $\overline{\boldsymbol{\mathcal{F}}}$ are the filtered body forces, $\overline{\boldsymbol{\mathcal{F}}} = \beta_p(\overline{T} - T_{ref})\boldsymbol{g}$, being $\boldsymbol{g}$ the gravity vector and, β_p is the thermal expansion coefficient. Note that all the thermo-physical properties are evaluated at T_{ref}, which is the free stream temperature. The last term in equations 4.2 and 4.3 indicates some modelisation of the filtered non-linear convective term. τ represents the SGS stress tensor which is defined as

$$\tau = -2\nu_{SGS}\overline{S} + \frac{1}{3}(\tau : I) \tag{4.4}$$

where $\overline{S}$ is the filtered rate of strain $\overline{S} = \frac{1}{2}[\nabla(\overline{u}) + \nabla^*(\overline{u})]$ and ∇^* is the transpose of the gradient operator. τ_T term is evaluated as τ (4.4) but ν_{SGS} is substituted by $\kappa_{SGS} = \nu_{SGS}/Pr_t$, where Pr_t is the turbulent Prandtl number (0.9 in Termofluids code).

In the present study, the Wall-Adapting Local-Eddy viscosity [16] model within a Variational Multiscale approach [17] (VMS-WALE) is used for modelling the subgrid scale stress tensor. In the variational multiscale (VMS) approach, originally formulated by Hughes [17] for the Smagorinsky model in the Fourier space, three classes of scales are considered: large, small and unresolved scales. If a second filter, with filter length $\hat{l}$, is introduced (usually called test filter), a splitting of the scales can be performed, $f' = \overline{f} - \hat{f}$. Following Vreman [18] notation, f' is called the small-scale component, $\hat{f}$ the large-scale component, and $\overline{f}$ is the original resolved quantity. Thus, for the large-scale part of the resolved $\overline{u}$ a general governing equation can be derived,

$$\frac{\partial \overline{\boldsymbol{u}}}{\partial t} + (\overline{u} \cdot \nabla)\overline{\boldsymbol{u}} - \nu \nabla^2 \overline{\boldsymbol{u}} + \rho^{-1} \nabla \overline{\boldsymbol{p}} + \overline{\boldsymbol{\mathcal{F}}} = -\frac{\partial \hat{\tau}}{\partial x_j} - \frac{\partial \tau'}{\partial x_j} \tag{4.5}$$

where $\hat{\tau}$ is the subgrid term in the large-scale equation and τ' is the subgrid small-scale term. By neglecting the effect of the unresolved scales in the large-scale equation ($\hat{\tau} = 0$), we only need to model the τ'. In our implementation the small-small strategy is used in conjunction with the WALE model:

$$\tau' = -2\nu_{SGS} S' + \frac{1}{3}(\tau' : I) \tag{4.6}$$

$$\nu_{SGS} = (C_w^{VMS} \Delta)^2 \frac{(\nu' : \nu')^{3/2}}{(S' : S')^{5/2} + (\nu' : \nu')^{5/4}} \tag{4.7}$$

$$S' = \frac{1}{2}[\nabla(\overline{u'}) + \nabla^*(\overline{u'})] \tag{4.8}$$

$$\nu' = \frac{1}{2}[\nabla(\overline{u'})^2 + \nabla^*(\overline{u'})^2] - \frac{1}{3}(\nabla(\overline{u'})^2) \tag{4.9}$$

where C_w^{VMS} is the VMS coefficient, which lies in the range between 0.3 and 0.5. In Termofluids code [15] this value is set to 0.325 according to previous experiences with quasi-homogeneous turbulence and was tested for different flows (see for instance [11, 13, 14, 19, 20]).

4.2.2 Definition of the case and numerical model

The geometry of a full-scale Eurotrough solar collector [2] has been selected for this study. A typical HCE with a stainless steel absorber inner/outer diameter of 6.6/7.0 cm and glass cover of 10.9/11.5 inner/outer diameter has been considered in the simulations. The computational domain is defined by 5W in the upstream direction, 20W in the downstream direction (x-direction), 9W in the cross direction (y-direction), and πW in the span-wise direction (z-direction), where W=5.8m is the

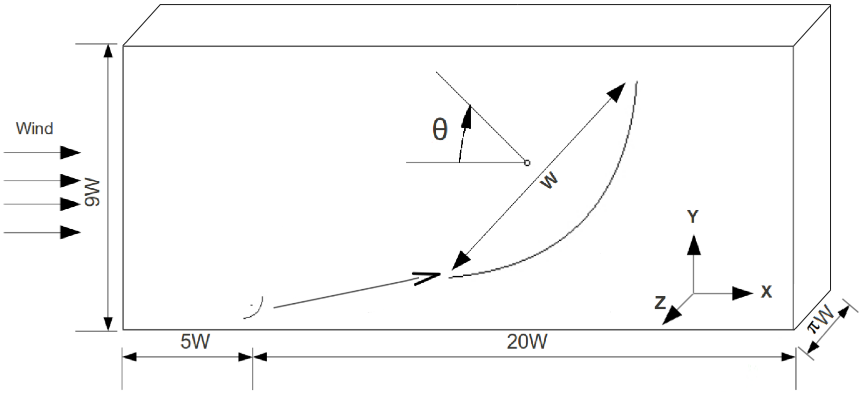

Figure 4.1: Computational domain of the wind flow study around an Eurotrough solar collector.

aperture of the parabola (see the figure 4.1). The parabolic collector is usually large in length compared to the parabola dimension. Thus, in such conditions, the flow in the span-wise direction (z-direction in figure 4.1) might be considered spatially periodic in that direction. Note that the use of spatially periodic domain implies that the span-wise size should be large enough to contain the largest scales of the flow. In this sense, various span-wise sizes have been tested (not shown here for the sake of brevity) in order to ensure that there was no influence in the results. After these studies, the length of πW for the span-wise directions is used in all the cases presented.

A uniform wind speed in the inlet velocity profile is considered. Although, the PTCs are exposed to the atmospheric boundary layer, the uniform velocity assumption represents the worst-case scenario for structural loading and could be incorporated as a design safety factor. Slip conditions are fixed in the top and bottom boundaries, while at the outlet a pressure-based condition is used. At the mirror and HCE surfaces, no-slip conditions are prescribed. As for the span-wise direction, periodic boundary conditions are imposed [21]. The Prandtl number is set to $Pr = \frac{\nu}{\kappa} = 0.7$ as for air. The temperatures of the glass cover and ambient air are fixed to $T_g = 350K$ and $T_{amb} = 300K$, respectively. A Neumann boundary condition ($\frac{\partial T}{\partial n} = 0$) is prescribed in the top, bottom and outlet boundaries for temperature.

The governing equations are discretised on a 3D unstructured mesh generated by the constant-step extrusion in the spanwise direction of a two dimensional unstructured grid. The mesh is refined around the mirror, the HCE and the near wake and then, stretched going away from the collector (see figure 4.2). A prism mesh is used

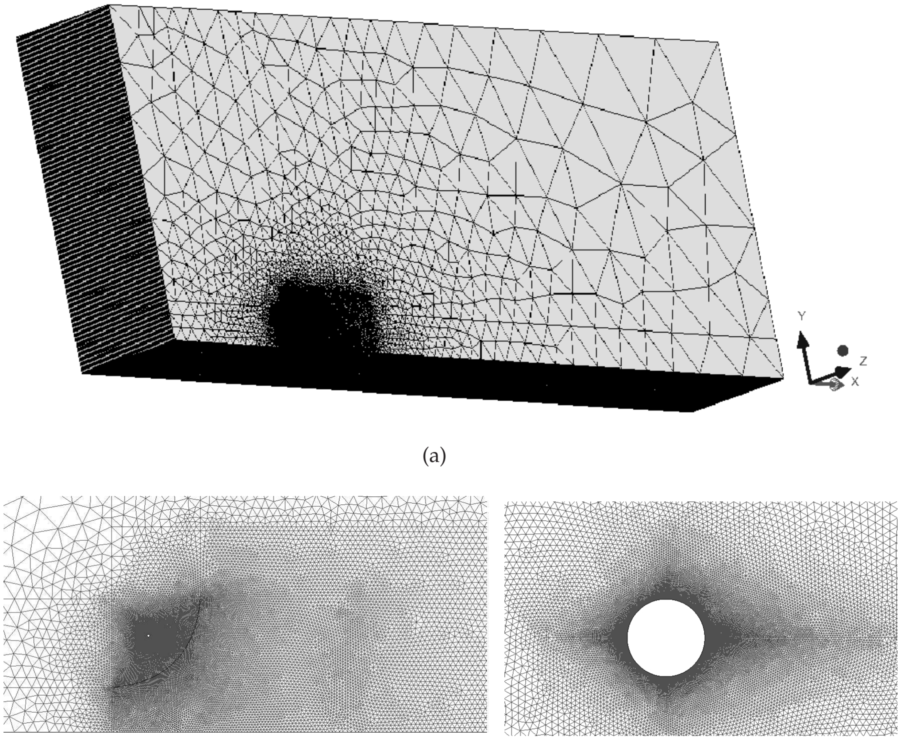

(a)

(b)

(c)

Figure 4.2: Example of mesh distribution at position $\theta = 45^\circ$:(a) 3D view (b) around PTC and (c) around HCE.

around the HCE to well capture the boundary layer.

The simulations are started from homogeneous flow and an impulsive flow initial condition is used. The flow field is advanced in time for initial duration to ensure statistically steady state. After all transients are washed out, statistics are collected for a sufficient long time which ensures temporal convergence.
Extensive grid refinement tests for each pitch angle (not shown here) are conducted in order to obtain a solution which accurately describes the fluid flow and heat transfer phenomena. The mesh is suited for each case of pitch angle and respect to the dimension of the problem. In order to capture the flow structures in the near wake of the PTC and around the HCE, mesh requirements are higher in these zones.

Table 4.1: Details of adopted meshes for each pitch angle

Position	0°	45°	90°	135°	180°	270°
Mesh plane	112322	104477	102914	81862	98375	104188
Number of planes	96	96	96	96	96	96
Grid size(MCVs)	10.78	10.02	9.87	7.85	9.44	10.0

However, due to the large difference between the dimensions of the aperture of the parabola and the receiver tube, the construction of the mesh is quite dense and complicated near these elements. For the sake of brevity, these studies are not shown and only results obtained with the finer grid for each pitch angle are presented. Indeed, finer meshes are about 10.78 Million Control Volumes(MCV) with 96 planes in the homogeneous direction. In table 4.1, the main characteristics of the meshes used for each pitch angle are given.

Numerical computations are carried out for different pitch angles ($\theta = 0°$, $45°$, $90°$, $135°$, $180°$, $270°$) and for Reynolds number $Re_D = \frac{uD}{\nu} = 7200$, based on the glass cover diameter. This Reynolds number corresponds to wind speed about $1\ m/s$ which is a typical value of wind speed encountered in solar plants. The Reynolds number has also been selected in order to compare the present results with the experimental results of Scholten and Murray [22] and Norberg [23] for the cross flow simulation around horizontal cylinder.

4.3 Validation of the numerical model

Although the code used for modelling the CFD&HT of fluid flow around parabolic collector and HCE described in previous section has been widely verified and validated using numerical results and experimental data from scientific research bibliography [10, 12, 24], simulations are also performed on a circular cylinder in a cross flow to test the accuracy of the numerical model and observe the effect of the parabolic collector on the HCE. The distribution of the drag forces around the circumference of the cylinder for $Re \simeq 7200$ is calculated and compared with experimental measurements of Scholten and Murray [22]. The boundary conditions and mesh distribution have been considered in a similar way as the previous section 4.2.2. The computational domain is extended to $[-15D, 25D]$;$[-10D, 10D]$;$[0, \pi D]$ in the stream-, cross- and span-wise directions respectively, and the cylinder with a diameter D is placed at (0,0,0). The results shown herein are computed for a finer grid of 130000×64 planes (i.e. 130000 CVs in the 2D planes extruded in 64 planes yielding

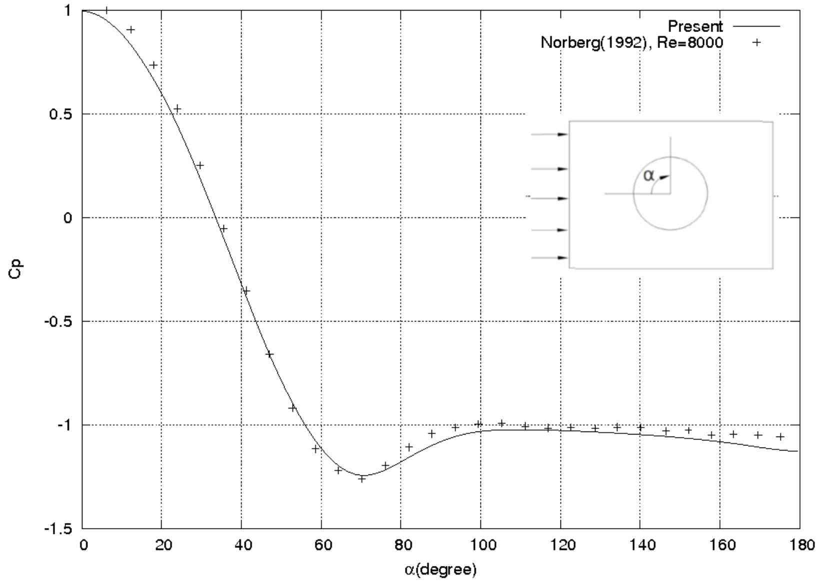

Figure 4.3: Variation of the drag coefficient around a circular cylinder in a cross flow. Comparison with experimental data of Norberg [23].

about 8.3MCVs).

First, the pressure distribution across the cylinder surface have been compared with experimental data of Norberg [23] at $Re = 8000$. The dimensionless pressure coefficient is calculated as

$$C_p = \frac{p - p_\infty}{\frac{1}{2}\rho u_\infty^2} \tag{4.10}$$

where p_∞ and u_∞ are the free-stream pressure and the velocity, respectively.

At these sub-critical Reynolds numbers, drag forces are almost constant over a large range of Reynolds numbers (see for instance [25]). Thus, it is expected that drag distributions at $Re = 7200$ compares well with that measured by Norberg [23] at $Re = 8000$. In figure 4.3, this comparison against experimental data is presented. It can be seen from this figure that the numerical results reproduce accurately experimental measurements [23] in the attached boundary layer zone, as well as, in the back zone with the same minimum magnitude and angle position where it occurs. Furthermore, the Nusselt number ($Nu = \frac{hD}{\lambda}$), which describes the heat transfer characteristics for the flow around the circumference of the cylinder in cross flow is calculated.

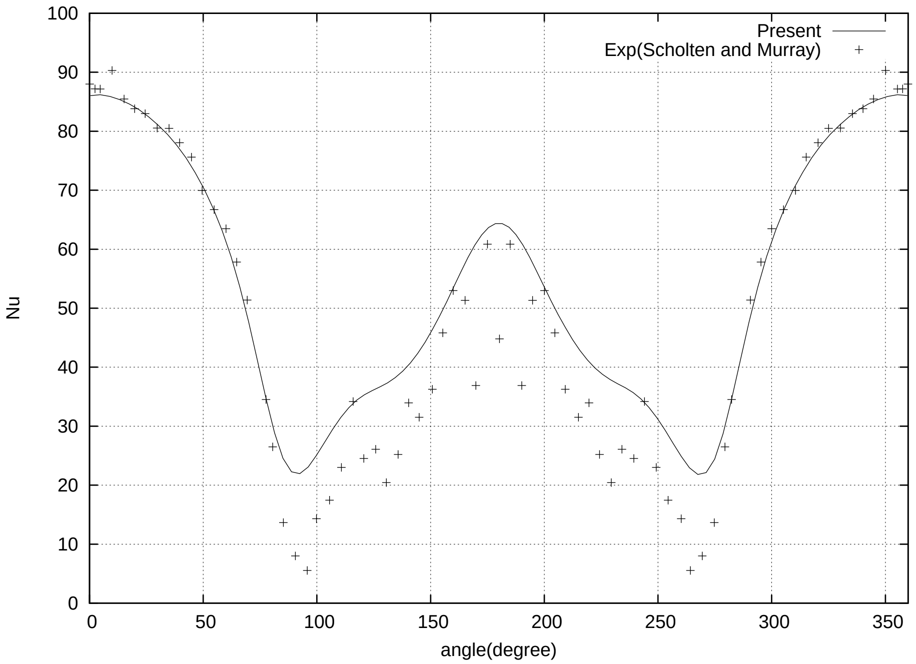

Figure 4.4: Variation of the Nusselt number around the HCE and comparison with cross flow horizontal cylinder and experimental data [22] at $Re = 7190$

The calculated local Nusselt number for the circular cylinder in cross flow gives a fair agreement with experimental measurements [22] and follows the same trends as shown in Figure 4.4. The Nusselt number is maximum at the leading edge or the front stagnation point (fsp) and, decreases smoothly by moving towards the top (or the bottom) of the cylinder. The minimum value occurs at about 90° from the stagnation point of the cylinder, which is associated with flow separation and the formation of a recirculation zone in the near wake. That is, the local separation restricts heat transfer away from the surface and causes the decrease of the Nusselt number. It increases again by approaching to the wake region as the turbulent wake allows heat to be removed. It should be pointed out that there are some differences respect to the experiments in the rear zone of the cylinder where heat transfer fluctuations are more random in nature and more complicated to measure [22]. Acording to Scholten and Murray [22], the high level of fluctuation in that zone are due to the extensive mixing of the fluid. This might be the reason of the discrepancies en-

countered between present results and experimental measurements. The predicted averaged Nusselt number is about 52.2, which represents a 5 % of difference compared to experimental results. However, the percentage of the fluctuation of the averaged Nusselt number for experimental measurements [22] was estimated to be 21.4 %. Thus, the present results are well within these experimental fluctuations.
By comparing the present computation results with the available experimental measurements [22, 23], a good agreement can be observed for both fluid flow and heat transfer characteristics, which proves the accuracy of the present numerical model and the turbulence model performance used herein.

4.4 Results and discussion

4.4.1 Averaged forces on the parabola

Numerical simulations are performed to study the wind flow of $1m/s$ around the PTC, which corresponds to Reynolds number based on the collector aperture of $Re_W = \frac{uW}{\nu} = 3.6 \times 10^5$ at different pitch angles ($\theta = 0°$, $\theta = 45°$, $\theta = 90°$, $\theta = 135°$, $\theta = 180°$, $\theta = 270°$).

Aerodynamic coefficients at these pitch angles are calculated and compared to experimental measurements in figure 4.5. The experimental measurements were carried out for an LS-2 solar collector [26] constructed at a scale of 1:45. Two types of wind-tunnel models were used for comparison: *i)* a light-weight model for measuring lift and drag dynamics wind loads using a high-frequency force balance and *ii)* a rigid plastic model instrumented with pressure taps for measuring pressure distribution over the surface of the PTC.
As can be seen from figure 4.5, the numerical predictions obtained are within the error-bars of both experimental measurements from the wind-tunnel data [27]. Discrepancies between computed and measured aerodynamic coefficients are mainly due to the unsteady flow behaviour and ground effects, which may affect the flow structures and separations behind the PTC and requires long measurement duration. On the other hand, it should be considered that there also could be some differences due to the scaling up of the Reynolds number used in the measurement model to avoid the compressibility effects. Although Hosoya et al. [27] studied the independence of the aerodynamic performances of the PTC, at the model scale Reynolds number range ($Re \sim 10^4$), it is not straightforward to extrapolate their study to the full scale case ($Re \sim 10^6$).
The zero pitch angle presents the maximum drag force (C_P) and it decreases by moving the parabolic trough toward the horizontal position ($\theta = 90°$). However, the absolute value of lift coefficient C_f is nearly zero at $\theta = 0°$ and increases by ap-

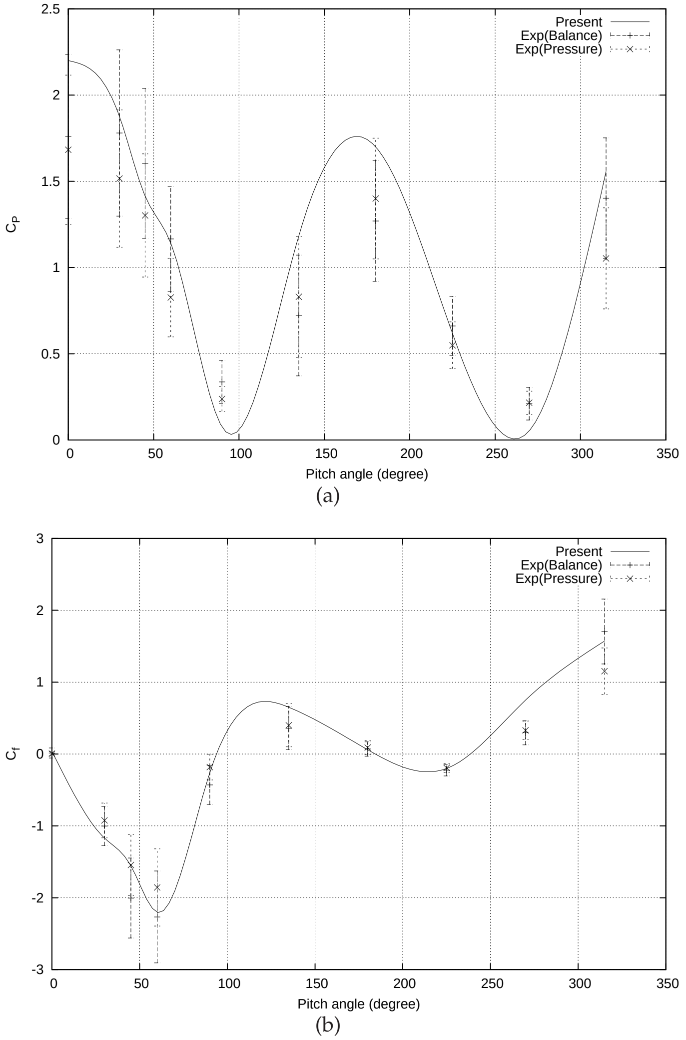

Figure 4.5: Predicted and measured aerodynamic parameters for the Eurotrough PTC (a)drag and (b)lift coefficients.

proaching to the horizontal position ($\theta = 90°$), as well as, to the stow mode ($\theta = 270°$) where the concave surface of the trough is facing the ground. The maximum absolute lift force occurred at about $\theta = 60°$.

4.4.2 Instantaneous flow

The variations of the aerodynamic coefficients can clearly be understood if the instantaneous flow is studied.

In figure 4.6, the instantaneous velocity field for different pitch angles ($\theta = 0°$,$45°$, $90°$, $135°$, $180°$ and $270°$) are depicted. The flow around the edge of the PTC is shown and the streak of flow stream known as shear layer is observed. The shear layer includes the separation zone and its trajectory depend on the pitch angle.
A large separated zone is observed at $\theta = 0°$. The turbulent flow in the detached region produces a large depression region in the back of the PTC being the responsible for the large value of drag coefficient obtained. The shear layer is more elevated at this position and the flow seems to follow the curvature of the PTC. With the increase of the pitch angle from $\theta = 0°$ to $\theta = 90°$, the separated zone is continuously reduced, which provokes a reduction of drag forces on the PTC surface. At pitch angle $\theta = 90°$, only a small recirculation zone is formed within the parabola region. This is the most favorable position for the PTC to work, i.e. when the parabola is aligned with the free-stream direction, the flow is completely attached to the parabola surface which provokes the reduction of the drag forces. By moving the PTC from $\theta = 90°$ to $\theta = 180°$, a large recirculation zone is formed in the opening of the parabola and the drag forces increase again. Unsteady vortices separate from the edge of the PTC and move further away from the collector. When the PTC approaches to the stow mode $\theta = 270°$, the separated zone is reduced again as well as the drag forces.

4.4.3 Mean flow configuration

The mean flow around the PTC show different structures and recirculation regions around the collector and the HCE. These flow structures are strongly related to the collector orientation and the pitch angle. Several recirculation regions are formed around the HCE depending on to the pitch angle and the position of the PTC. The different time-averaged flow configuration for each pitch angle around the solar collector and the HCE are depicted in figure 4.7.

For a pitch angle of $\theta = 0°$, a large recirculation region behind the PTC is observed. This region extends up to $7.03W$ with two large counter-rotating vortices in the leeward side of the collector. In this position, the PTC receives the maximum drag forces and minimum lift forces due to the shape of the collector. The flow

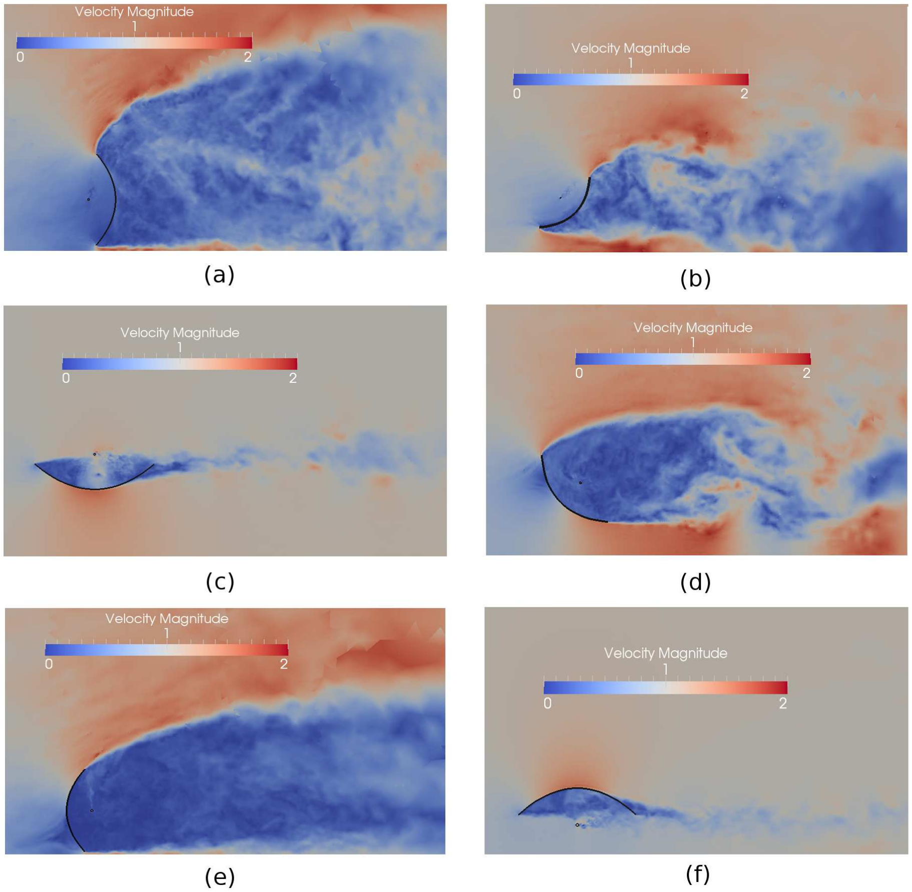

Figure 4.6: Instantaneous velocity field around the PTC for different pitch angles: (a) $\theta = 0°$, (b) $\theta = 45°$, (c) $\theta = 90°$, (d) $\theta = 135°$, (e) $\theta = 180°$, (f) $\theta = 270°$.

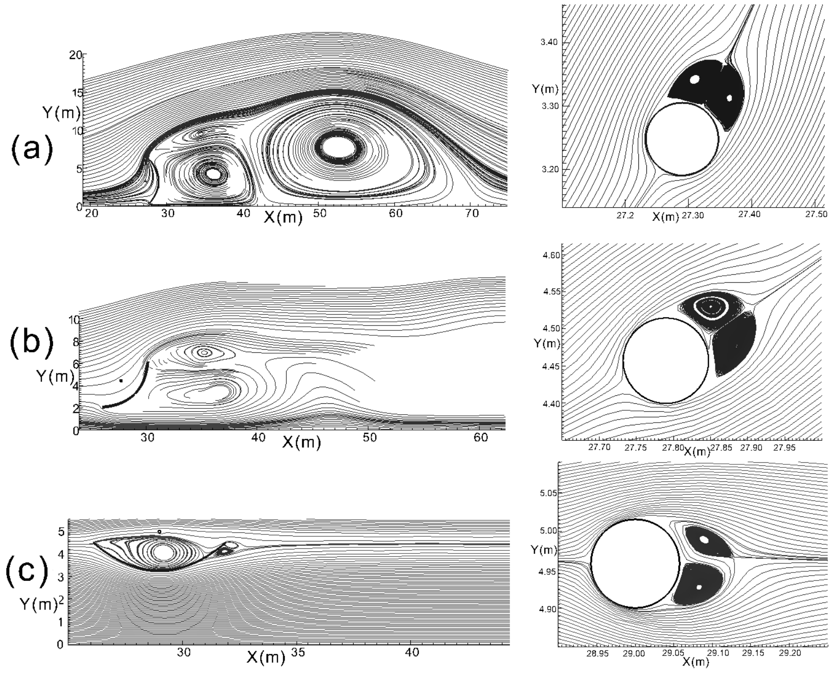

Figure 4.7: Streamlines for the time-averaged flow around the PTC and the HCE for different Pitch angles: (a) $\theta = 0°$, (b) $\theta = 45°$, (c) $\theta = 90°$.

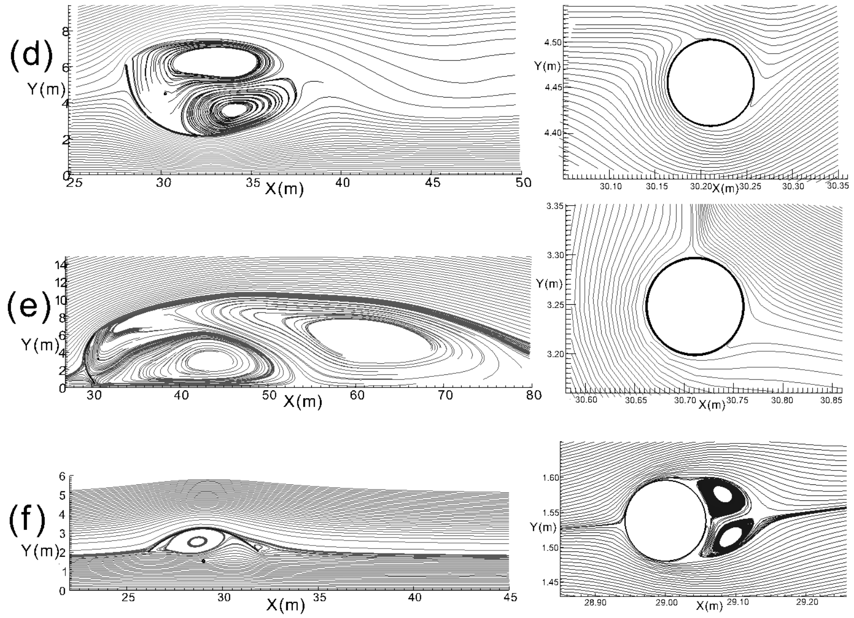

Figure 4.8: Streamlines for the time-averaged flow around the PTC and the HCE for different Pitch angles: (d) $\theta = 135°$, (e) $\theta = 180°$, (f) $\theta = 270°$.

around the HCE follows the tilt of the collector and seems to be oriented towards the upper edge of the PTC. Two small counter-rotating vortices attached to the backward side of the HCE can be observed.

At a pitch angle of $45°$ flow separation occurs from the upper and lower edges creating several recirculation regions behind the PTC. The recirculation region decreases compared to $\theta = 0°$ and the shear layer is much lower. Thus, the drag coefficient decreases and the absolute value of the lift coefficient increases. As for flow around the HCE similar to $\theta = 0°$, it follows the tilt of the collector and a recirculation bubble with two vortices is also formed in the wake region of the receiver tube.

The recirculation region is reduced sharply when the collector is approached to the horizontal position $90°$. For this position small eddies are formed in the leeward side of the PTC and the recirculation region is relatively small, which explain the minimum drag forces. Several eddies are also formed within the aperture of the collector without affecting the flow around the HCE. When the wind blows toward the back side of the collector, the flow separation is reduced due the flow direction and the convex shape of the collector. The flow around the HCE is similar to the cross flow around a circular cylinder and there is also formation of vortex shedding downstream the receiver tube.

At a pitch angle of $135°$, two large vortices are formed in the forward side of the PTC, where negative pressures are observed. The recirculation region is increased by moving the collector from the horizontal position, therefore the drag forces are increased. As the flow velocity within the recirculation zone is low, the flow around the HCE is laminar and no vortices are observed. The flow in the forward side of the PTC follows the curvature of the collector with the formation of two superposed large vortices. The receiver tube is located inside the upper vortex.

The recirculation region increases sharply at a pitch angle of $180°$ and extends up to $7.6W$ with two superposed large eddies formed behind the PTC. The shear layer is again elevated but not as much as for $\theta = 0°$, which explain the increase of the drag forces at $\theta = 180°$, yet remains lower than the vertical position ($\theta = 0°$). The receiver tube is placed into the upper vortex of the forward side of the PTC. The flow structure around the HCE is laminar and follows the curvature of the collector as well.

By moving the PTC towards the stow mode ($\theta = 270°$), the recirculation region is reduced sharply. Similar to the position $\theta = 90°$, only small eddies are observed behind the solar collector and the drag forces are then reduced. Another recirculation region is also formed in the concave of the parabola. The fluid flow around the HCE is also similar to the cross flow around a circular cylinder with a small deviation due to the effect of the ground. Behind the receiver tube, a small recirculation bubbles is formed.

According to the flow separation and recirculation regions, it can be concluded that the wind forces are important regarding to the mirrors stability for pitch angle $\theta > 90^\circ$ due to the eddies formation in the forward side of the PTC. However, for pitch angle $\theta < 90^\circ$ the eddies are stronger in the leeward side of the PTC which affect more the PTC structure stability, as well as, the tracking system.

4.4.4 Heat transfer around HCE

The heat transfer around the HCE is also studied for different pitch angles to determine the local Nusselt number around the HCE. Depending on the pitch angle, convection around the HCE might be forced or forced and free (mixed convection). The Richardson number ($Ri = Gr/Re^2$), which is a balance between the buoyancy forces to the viscous forces, is an important parameter to determine the nature of the convection mode: free, forced or mixed convection. When $Ri << 1$, free convection is negligible and only forced convection takes place. For $Ri >> 1$ free convection dominates and the mixed free and forced convection occurs for $Ri \approx 1$. In most of the cases considered in the present work (i.e for pitch angles of $\theta = 0^\circ, 45^\circ, 90^\circ$ and 270°), $Ri = 0.2$ which correspond to a forced convection. However, for pitch angles of 135° and 180°, the HCE is within the large recirculation bubble formed behind the parabola (see figure 4.7d and 4.7e). Under these conditions, flow velocities are extremely low (if compared to free-stream velocity) which decreases the Reynolds number and increase the Richardson number. Thus, in those cases free convection becomes as important as forced convection and buoyancy forces should be considered.

In figure A.0.2, the distribution of the local Nusselt number for different pitch angles is shown. Table 4.2 summarizes the average Nusselt number Nu_{avg} around the HCE and the local Nusselt number at the front stagnation point Nu_{fsp}, as well as the maximum Nusselt number Nu_{max} and the minimum Nusselt number Nu_{min} together with their position of occurrence. These results are also compared with available experimental data [22] and the correlation of Zukauskas [28], found in the literature for the case of cross flow around a circular cylinder and the results presented in section 4.3.

The local Nusselt number relates the actual heat transferred from the wall of the

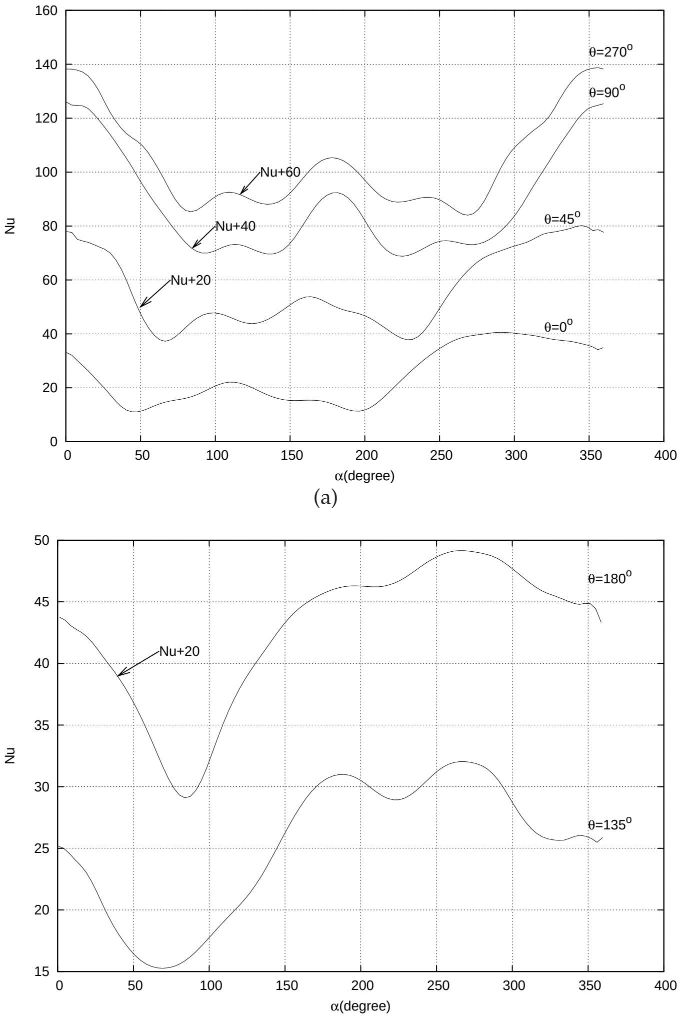

(a)

(b)

Figure 4.9: Variation of the local Nusselt number around the HCE for (a) forced convection (b) mixed convection.

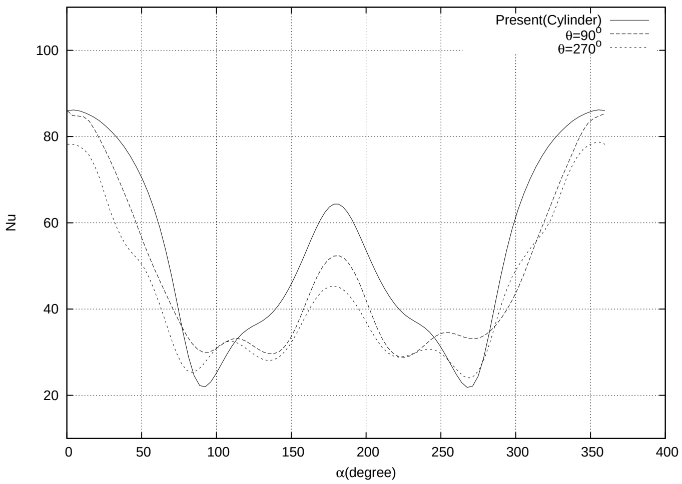

Figure 4.10: Influence of the parabola in the variation of the predicted Nusselt number around the HCE. Comparison against the Nusselt number for the circular cylinder case (without parabola). Dashed line for horizontal position $\theta = 90°$, dotted line for stow mode $\theta = 270°$ and solid line for the cross flow around circular cylinder.

glass cover to a reference value of the transferred heat.

$$Nu = \frac{q_{actual}}{q_{ref}} = \frac{-\lambda \partial T_r / \partial n}{-\lambda (T_g - T_{amb}) / D_g} \tag{4.11}$$

Where T_r is the temperature of the nearest node to the glass cover wall. The averaged Nusselt number Nu_{avg} is calculated by integrating Nusselt number around the HCE.

$$Nu_{avg} = \frac{1}{2\pi} \int_0^{2\pi} Nu_\alpha d\alpha \tag{4.12}$$

According to figure 4.9, the profile of local Nusselt number at $\theta = 0°$ is similar to the profile of Nusselt number for cross flow around circular cylinder but displaced towards the stagnation point by an angle of about $90°$. This can be explained by the displacement of the fluid structure around the HCE due to the tilt of the parabola shown in figure 4.7 (a). The magnitude of the averaged Nusselt number is reduced to 53% compared to the circular cylinder in the cross flow case. This is mainly due to the effect of the parabola that plays the role of a fence against the normal winds, which reduces the velocity around it and deviates the direction of the winds following its curvature.

For a pitch angle of $\theta = 45°$, the same phenomena is observed as $\theta = 0°$ and the local Nusselt number seems to be displaced towards the stagnation point by an angle of about $45°$ compared to the cross flow circular cylinder. As can be seen from figure 4.7 (b), the flow around the HCE is following the tilt of the parabola, which explain the distribution of Nusselt number around the HCE. Furthermore, the magnitude of the Nusselt number is reduced to 30% compared to the circular cylinder in cross flow case, which can be explained by the effect of the collector and its orientation. The magnitude of the velocity in this position is less affected than $\theta = 0°$ because of the orientation of the collector.

The distribution of the Nusselt number at a position of $\theta = 90°$ is symmetric and similar to the cross flow around the horizontal tube. The magnitude of the averaged Nusselt number is only reduced by 9%. This is due mainly to the effect of the parabola that allows the wind to pass through but slow down the velocity by its curvature. In figure 4.10, it is shown that the distribution of local Nuseelt number follows the same trend of cross flow condition which can be explain by the flow structure around the HCE shown in figure 4.7 (c).

By moving the PTC to the position $\theta = 135°$, mixed convection occurs and the profile of the local Nusselt number is no longer similar to the cross flow condition. In this case, the HCE is placed in the wake behind the PTC and the flow impinges on the HCE at $\theta > 180°$ where the Nusselt is maximum. The Nusselt number decreases in the upper side of the HCE where the flow is separated from the receiver tube, as can be seen from figure 4.7 (d). The magnitude of the averaged Nusselt number is reduced to 51% due to the effect of the PTC that reduces sharply the velocity and the direction of the winds.

At a pitch angle of $\theta = 180°$, mixed convection is also present and the local Nusselt number is different to the cross flow condition. As can be seen from figure 4.7 (e), the HCE is situated in the upper bubble of the downstream side. The fluid flow shocks with the receiver tube in the lower side where the local Nusselt number is higher and leaves in the upper side which explain the decrease of Nusselt number there. The magnitude of the averaged Nusselt number is also reduced to 56% due to effect of the solar collector.

Furthermore, the fluid flow around the HCE in the stow mode ($\theta = 270°$) is similar to the position $\theta = 90°$ and the cross flow around circular cylinder. The local Nusselt number is also symmetric and follows the same trend as can be seen from figure 4.10. The magnitude of the averaged Nusselt number is decreased by 16%, which is higher than the horizontal position ($\theta = 90°$) due to the effect of the ground

Table 4.2: Numerical data of averaged, front stagnation, maximum and minimum Nusselt numbers for each pitch angle and comparison with experiments [22] and the correlation of Zukauskas [28]

Position	Nu_{avg}	Nu_{fsp}	Nu_{max}/Pos	Nu_{min}/Pos
0°	24.5	33.1	41.4/289.5°	9.5/196.8°
45°	36.4	58	61.2/350.9°	15.9/67.5°
90°	47.4	86	86/0°	27.3/222°
135°	25.1	25.2	32.4/269.6°	15.1/64.6°
180°	22.5	23.7	29.1/269.5°	7.4/85.9°
270°	43.4	78.2	78.9/355.84°	21.1/273.4°
Cylinder	52.2	86	86.57/357.4 °	17.4/272.2°
Experimental [22]	49.5	88	90.3/9.9°	5.5/95.7°
Zukauskas [28]	47.3	-	-	-

in this position.

For different cases of pitch angles, the magnitude of the average Nusselt number is reduced compared to the cross flow condition. This reduction is desirable since it reduces heat losses from the HCE and improves the thermal efficiency.

4.5 Conclusions

A detailed numerical model based on LES models for simulating the fluid flow and heat transfer around a parabolic trough solar collector and its receiver tube is presented in this work. This study provides a quantitative assessment of velocity, pressure and temperature fields around an isolated parabolic solar collector and its receiver. First, the accuracy of the numerical model is verified on a circular cylinder in a cross flow. Pressure distribution and heat transfer characteristics around the circumference of the cylinder are calculated and validated with available experimental data. Then, numerical simulations are performed on a Eurotrough solar collector to evaluate the averaged forces in the parabola. The aerodynamic coefficients are calculated around the PTC and validated with experimental model-to-full scale measurements. Numerical results matched experimental ones, although some discrepancies are observed due to the unsteady flow behaviour and ground effects, as well as, to the scaling up of the Reynolds number in the measurement model. Furthermore, the instantaneous flow around the parabola are studied for different pitch angles in order to explain the variation of the aerodynamic coefficients. It is shown that the horizontal position $\theta = 90°$ is the most favourable position for the PTC to work where the drag forces are lower and increase by moving the PTC.

In addition to that, time-averaged flow for each pitch angle is studied around the PTC and the HCE. Several recirculation regions are observed which are strongly related to the collector orientation and the pitch angle. It is concluded that the stability of the mirrors are much more affected by wind forces for pitch angle $\theta > 90°$, while the PTC structure stability is more affected by wind forces for pitch angle $\theta < 90°$. After that, the heat transfer around the receiver tube is carried out for different pitch angles to calculate the Nusselt number. Depending on the pitch angle, convection around the HCE might be forced or mixed. The distribution of the Nusselt number around the HCE for $\theta = 90°$ and $\theta = 270°$ are symmetric and similar to the cross flow around circular cylinder. For pitch angles $\theta = 90°$ and $\theta = 45°$ the profile of the Nusselt number is similar to the cross flow circular cylinder but displaced towards the stagnation point by an angle proportional to the tilt of the PTC. However, the Nusselt number at $\theta = 135°$ and $\theta = 180°$ are quite different to the cross flow cylinder, where mixed convection occurs and the flow around the HCE is laminar. In these positions, i.e. where the recirculation region is formed in the forward side of the PTC, Nusselt number are the lowest being the most favourable position from a thermal point of view.

Finally, it has to be pointed out that the study of the turbulent flow around the solar collector and its receiver is of major interest for determining the aerodynamic behaviour and the overall efficiency of such devices. By means of these simulations, it is possible to predict the fluid flow structures and the heat transfer characteristics around the PTC and the HCE for an isolated PTC. However, solar collectors are used in array filed for solar plants. It is also of interest to study of the effect of higher wind speeds on the predicted results that will be treated in the next chapter.

References

[1] H. Price, E. Lüpfert, D. Kearney, E. Zarza, G. Cohen, R. Gee, and R. Mahoney. Advances in parabolic trough solar power technology. *Journal of Solar Energy Engineering*, 124(2):109–125, 2002.

[2] E. Lüpfert, M. Geyer, W. Schiel, A. Esteban, R. Osuna, E. Zarza, and P. Nava. EUROTROUGH design issues and prototype testing at PSA. In *Proceedings of ASME International Solar Energy Conference- Forum 2001*, pages 289–394, Washington, DC, April 21-25. Solar Energy: The power to Choose.

[3] R. Foristall. Heat transfer analysis and modeling of aparabolic trough solar receiver implemented in engineering equation solver. Technical report, National Renewable Energy Laboratory(NREL), 2003.

[4] O. García-Valladares and N. Velázquez. Numerical simulation of parabolic trough solar collector: improvement using counter flow concentric circular heat exchangers. *International Journal of Heat and Mass Transfer*, 52(3):597–609, 2009.

[5] R.V. Padilla, G. Demirkaya, D.Y. Goswami, E. Stefanakos, and M. Rahman. Heat transfer analysis of parabolic trough solar receiver. *Applied Energy*, 88(12):5097–5110, 2011.

[6] S.A. Kalogirou. A detailed thermal model of a parabolic trough collector receiver. *Energy*, 2012. http://dx.doi.org/10.1016/j.energy.2012.06.023.

[7] K. Ravi Kumar and K.S. Reddy. Thermal analysis of solar parabolic trough with porous disc receiver. *Applied Energy*, 86(9):1804–1812, 2009.

[8] W. Rodi. Comparison of LES and RANS calculations of the flow around bluff bodies. *Journal of Wind Engineering and Industrial Aerodynamics*, 69:55–75, 1997.

[9] Z.T. Xie and I.P. Castro. LES and RANS for turbulent flow over arrays of wall-mounted cubes. *Flow Turbulence and Combustion*, 76(3):291–312, 2006.

[10] I. Rodríguez, R. Borrell, O. Lehmkuhl, C.D. Pérez-Segarra, and A. Oliva. Direct numerical simulation of the flow over a spher at Re=3700. *Journal of Fluids Mechanis*, 679:263–287, 2011.

[11] O. Lehmkuhl, A. Baez, I. Rodríguez, and C.D. Pérez-Segara. Direct numerical simulation and large-eddy simultaions of the turbulent flow around a NACA-0012 airfoil. In *ICCHMT*, 2011.

[12] I. Rodríguez, O. Lehmkuhl, R. Borrell, and A. Oliva. Flow dynamics in the turbulent wake of a sphere at sub-critical Reynolds numbers. *Computers & Fluids*, 80:233–243, 2013.

[13] J. Calafell, O. Lehmkuhl, I. Rodríguez, and A. Oliva. On the Large-Eddy Simulation modelling of wind turbine dedicated airfoils at high Reynolds numbers. In K. Hanjalić, Y. Nagano, D. Borello, and S. Jakirlic, editors, *Turbulence, Heat and Mass Transfer*, volume 7, pages 1–12, Palermo, Italy, 2012. Begell House, Inc.

[14] D. Aljure, I. Rodríguez, O. Lehmkhul, R. Borrell, and A. Oliva. Flow and turbulent structures around simplified cars models. In *Conference on Modelling Fluid Flow (CMFF'12)*, pages 247–254, Budapest, Hungary, 2012.

[15] O. Lehmkuhl, C. D. Pérez-Segarra, R. Borrell, M. Soria, and A. Oliva. TERMOFLUIDS: A new Parallel unstructured CFD code for the simulation of turbulent industrial problems on low cost PC Cluster. In I.H. Tuncer, Ü. Gülcat, D.R. Emerson, and K. Matsuno, editors, *Proceedings of the 2005 Parallel Computational Fluid Dynamics Conference*, volume 67 of *Lecture Notes in Computational Science and Engineering*, pages 275–282. Springer, 2007.

[16] F. Nicoud and F. Ducros. Subgrid-scale stress modelling based on the square of the velocity gradient tensor. *Flow, Turbulence and Combustion*, 62:183–200, 1999.

[17] T. Hughes, L. Mazzei, and K. Jansen. Large eddy simulation and the variational multiscale method. *Computing and Visualization in Science*, 3:47–59, 2000.

[18] A. Vreman. The filtering analog of the variational multiscale method in large-eddy simulation. *Physics of fluids*, 15(8):L61–L64, 2003.

[19] I. Rodríguez, O. Lehmkuhl, R. Borell, and C.D. Pérez-Segarra. On DNS and LES of natural convection of wall-confined flows: Rayleigh-bernard convection. In Springer Netherlands, editor, *In Direct and Large-Eddy Simulation VIII*, pages 389–394, 2011.

[20] I. Rodríguez, C.D. Pérez-Segarra, O. Lehmkuhl, and A. Oliva. Modular object-oriented methodology for the resolution of molten salt storage tanks for csp plants. *Applied Energy*, 109:402–414, 2013.

[21] S.A. Orszag. Numerical methods for the simulation of turbulence. *Physics of Fluids*, 12(12):250–257, 1969.

[22] J.W. Scholten and D.B. Murray. Unsteady heat transfer and velocity of a cylinder in cross flow-i. low freestream turbulence. *Int Journal of Heat and Mass Transfer*, 41(10):1139–1148, 1998.

[23] C. Norberg. Pressure forces on a circular cylinder in cross flow. in bluff body wakes, dynamics and instabilities. In *Proc IUTAM Symp*, volume 115, pages 7–11, September 1992.

[24] R. Capdevila, O. Lehmkuhl, C.D. Pérez-Segarra, and G. Colomer. Turbulent natural convection in a differentially heated cavity of aspect ratio 5 filled with non-participating and participating grey media. In IOP Publishing, editor, *In Journal of physics: conference series*, 2011. doi: 10.1088/1742-6596/318/4/042048.

[25] E Achenbach. Distribution of local pressure and skin friction around a circular cylinder in cross-flow up to Re=5*10^6. *Journal of Fluid mechanics*, 34(4):625–639, 1968.

[26] G.E. Cohen, D.W. kearney, and G.J. Kolb. Final report on the operation and maintenance improvement for concentrating solar power plants. Technical Report SAND99-1290, Sandia National Laboratories, 1999.

[27] N. Hosoya, J.A. Peterka, R.C. Gee, and D Kearney. Wind tunnel tests of parabolic trough solar collectors. Technical Report NREL/SR-550-32282, National Renewable Energy Laboratory, 2008.

[28] A. Zukauskas. Heat transfer from tubes in cross flow. *Advances in Heat Transfer*, 8:93–160, 1972.

Chapter 5

Wind speed effect on the flow field and heat transfer around a parabolic trough solar collector

Most of the contents of this chapter have been published as:
A.A. Hachicha, I. Rodríguez and A. Oliva. Wind speed effect on the flow field and heat transfer around a parabolic trough solar collector. *Applied Energy* (submitted) .

Abstract.

The parabolic trough solar collector is currently one of the most mature and prominent solar technology for production of electricity. These systems are usually located in an open terrain where strong winds may occur and affect their stability and optical performance, as well as, the heat exchange between the solar receiver and the ambient air. In this context, a wind flow analysis around a parabolic trough solar collector under real working conditions is performed. A numerical aerodynamic and heat transfer study based on Large Eddy Simulations is carried out to characterize the wind loads and the heat transfer coefficients. After the study carried out in Chapter 4 at $Re_{W1} = 3.9 \times 10^5$, computations are performed at higher Reynolds number of $Re_{W2} = 1 \times 10^6$ and for various pitch angles. The effects of wind speed and pitch angle on the averaged and instantaneous flow have been assessed. The aerodynamic coefficients are calculated around the solar collector and validated with measurements performed in wind tunnel tests. The variation of the heat transfer coefficient around the heat collector element with the Reynolds number is presented and compared to the circular cylinder in cross flow. Unsteady flow is studied for three pitch angles: $\theta = 0^\circ$, $\theta = 45^\circ$ and $\theta = 90^\circ$ and different structures and recirculation regions have been identified. A spectral analysis has been also carried out around the parabola and its receiver in order to detect the most relevant frequencies related to the vortex shedding mechanism which affect the stability of the collector.

5.1 Introduction

Parabolic trough solar collectors (PTC) are considered as one of the most mature, successful, and proven solar technology for electricity generation. PTCs are typically operated at 400° C and a synthetic oil is commonly used as heat transfer fluid (HTF). A PTC consists of a parabolic trough-shaped mirror that focus sunrays onto a heat collector element (HCE) that is mounted in the focal line of the parabola. The HTF circulates through the solar field to transport the absorbed heat. The solar field is made up of several solar reflectors composed in series which concentrate the direct solar radiation by means of a Sun-tracking system. The HCE is typically composed of a metal receiver tube and a glass envelope covering it with a vacuum between these two to reduce the convective heat losses.

The thermal and optical performances of PTC are related to the applied load coming from the wind action on the structure and the tracking system. During real work conditions, the array field of solar collectors require a good accuracy in terms of both mechanical strength and optical precision. Such requirements are sensitive to turbulent wind conditions and should be considered in the design of these systems. Hence, a wind flow analysis plays a major role for designing the solar collectors and can lead to a better understanding of the aerodynamic loading around the parabolic reflector, as well as, the convection heat transfer from the HCE.

Since the 1970s, numerous numerical and experimental studies have been proposed to study the heat transfer characteristics of PTC [1, 2, 3, 4]. However, wind flow studies around the PTC are scarce. In the late of 1970s and early 1980s, Sandia National Laboratories sponsored some wind tunnel tests, which were published in different reports [5, 6, 7, 8]. These reports provided mean wind load coefficients for an isolated parabolic trough solar collector and for a collector within an array field. Hosoya et al. [9] carried out a series of wind tunnel experiments about a PTC to determine the mean and maximum wind load coefficients on a PTC for different configurations. They also included in their study the effect of the location of the PTC in the collector field, as well as, the use of a porous fence. Gong et al. [10] performed field measurements on the Yan Qing solar collector in China to determine the boundary layer wind characteristics and the effect of wind loads on solar collectors for different configurations.

The majority of the numerical studies for studying wind flow around solar collectors are based on the Reynolds-Averaged Navier Stokes equations (RANS) [11, 12] which suffer from inaccuracies in predictions of flow with massive separations [13, 14].

A recent study by the authors [15] based on Large Eddy Simulations to quantify the fluid flow and heat transfer around a PTC for various pitch angles and a fixed wind speed 1 m/s. The study showed that this kind of detailed numerical simulations are feasible, but the effects of a higher wind speed was not explored.

In the present work, following the previous experiences, the impact of wind speed closer to real working conditions is considered. To do this, the wind flow around the PTC at a wind speed of 3 m/s is studied and compared to the results obtained at 1 m/s. These cases correspond with Reynolds numbers of $Re_{W1} = 3.6 \times 10^5$ and $Re_{W2} = 1 \times 10^6$ (the Reynolds number is defined in terms of the free-stream velocity and the aperture $Re_W = \frac{U_{ref} W}{\nu}$). Wind speed effects on unsteady and averaged fluid flow and heat transfer characteristics are assessed. Furthermore, a power spectra analysis is carried out to analyse the impact of the unsteady flow conditions on the PTC stability.

5.2 PTC numerical model

5.2.1 Mathematical model

The same methodology presented in the previous Chapter [15] for solving the fluid flow and heat transfer around the PTC is here adopted. This methodology has been proven and validated in turbulent flows around bluff bodies with massive separations and recirculation [16, 17, 18, 19]. Simulations are performed using the CFD&HT code Termofluids [20] which is an unstructured and parallel object-oriented code for solving industrial flows.

5.2.2 Definition of the case. Geometry and boundary conditions

Large-eddy simulations of the wind flow around a PTC at $Re_W = 10^6$ and different pitch angles of ($\theta = 0°, 45°, 90°, 135°$ and $270°$) have been performed. Here, Reynolds number has been defined in terms of the free-stream velocity U_{ref} and the parabola aperture W ($Re_W = \frac{U_{ref} W}{\nu}$). This Reynolds number corresponds with a wind speed of $U_{ref} = 3m/s$ which is a typical value of wind speed encountered in solar plants. In addition, the flow around the parabola has been compared to that obtained by the authors at a lower Reynolds numbers of $Re = 3.6 \times 10^5$ ($U_{ref} = 1m/s$) [15]. All computed flows are around a full-scale Eurotrough solar collector [21] and its typical HCE with a stainless steel absorber (inner/outer diameter of $6.6/7.0$ cm) and glass cover ($10.9/11.5$ cm of inner/outer diameter). As in the previous work [15], the same domain size of $25W \times 9W \times \pi W$ with the same steam-, cross stream- and span-wise directions has been used. The parabola of aperture $W = 5.8m$ is located at $5W$ in the stream-wise direction (see figure 5.1). For solving the computational domain, no-slip conditions at the parabola and HCE have been imposed. At the inlet, a uniform inlet velocity profile has been prescribed. For the top and bottom boundaries, slip conditions have been set, whereas in the span-wise

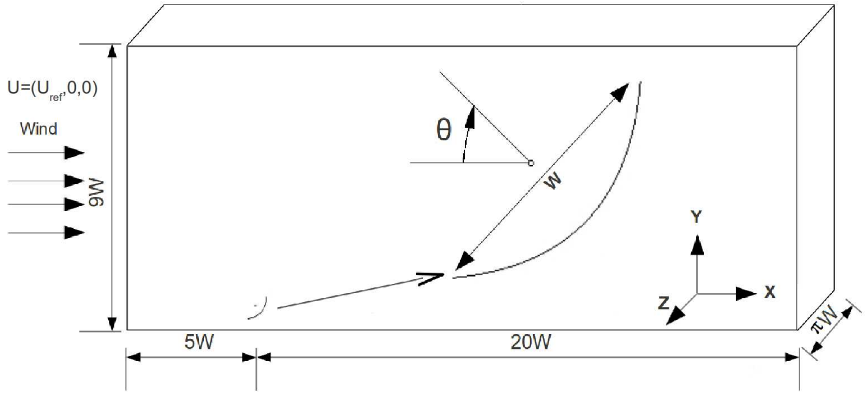

Figure 5.1: Computational domain of the wind flow study around an Eurotrough solar collector.

Table 5.1: Details of adopted meshes for each pitch angle

Position	0°	45°	90°	135°	180°	270°
Mesh plane	112322	104477	102914	99281	106223	104188
Number of planes	96	96	96	96	96	96
Grid size(MCVs)	10.78	10.02	9.87	9.53	10.19	10.0

direction, the flow has been considered to be spatially periodic, thus periodic boundary conditions have been imposed. For solving the energy equation, temperatures of the glass cover and ambient air are fixed to $T_g = 350K$ and $T_{amb} = 300K$, respectively. A Neumann boundary condition ($\frac{\partial T}{\partial n} = 0$) is prescribed in the top, bottom and outlet boundaries for temperature.

For more details about boundary conditions, the reader is referred to [15]. In termofluids, the governing equations (equations 4.1-4.3) have been discretised on a collocated unstructured grid arrangement by means of finite volume techniques using second-order conservative schemes [22]. The 3D meshes used for solving the computational domain have been obtained by the constant-step extrusion in the span-wise direction of a two-dimensional unstructured grid. Although not shown here, extensive grid refinements for each pitch angle have been conducted. Details of the final computational meshes for each pitch angle are given in table 5.1.

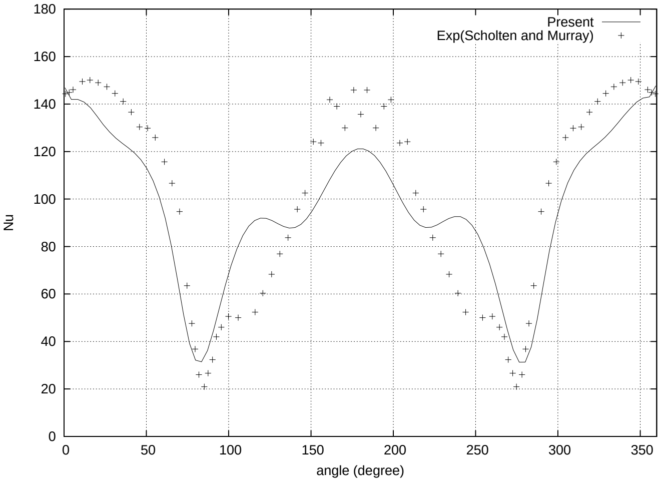

Figure 5.2: Variation of the Nusselt number around a cross flow horizontal cylinder and comparison with experimental measurements [23] at $Re_D = 21600$

5.3 Heat transfer from a circular cylinder in cross flow and wind speed effects

In order to analyse the influence of the wind speed in the heat transfer of the HCE, the numerical model has been first applied on a circular cylinder in cross flow. In this work, simulations have been performed for a Reynolds number of $Re_D = 21600$ (here Reynolds number is defined in terms of the free-stream velocity and cylinder diameter, $Re_D = U_{ref}D/\nu$) which corresponds with a wind speed of 3 m/s. Heat transfer characteristics around the cylinder have been calculated and compared against experimental measurements of Scholten and Murray [23]. In addition, results have also been compared to the lower Reynolds number of $Re = 7200$ [15] (which corresponds with wind speed of $1m/s$). The boundary conditions and mesh distribution have been considered in a similar way as the previous section 5.2.2. The computational domain is extended to $[-15D, 25D]$;$[-10D, 10D]$;$[0, \pi D]$ in the stream-, cross- and span-wise directions respectively, and the cylinder with a diameter D is placed at (0,0,0). The results shown herein are computed for a finer grid of 147000×64 planes (i.e. 147000 CVs in the 2D planes extruded in 64 planes yielding about 9.4 MCVs).

In figure 5.2, the predicted local Nusselt number around the circular cylinder is plotted. For comparison, the results of Scholten and Murray [23] are also shown. As

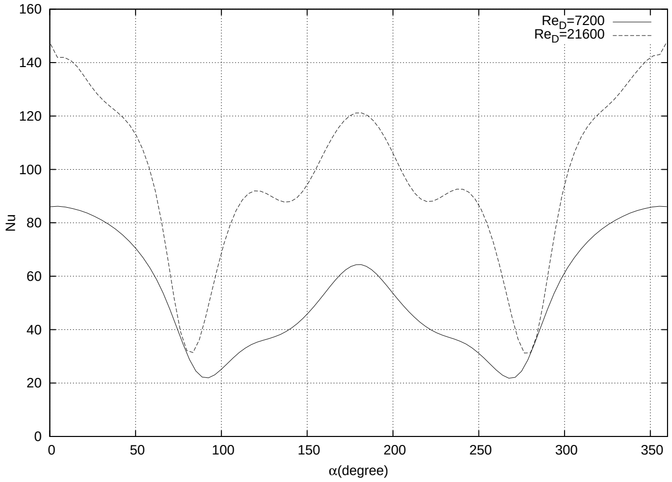

Figure 5.3: Comparison of Nusselt number around a circular cylinder in cross flow for two Reynolds numbers: $Re_D = 7200$ and $Re_D = 21600$

can be observed a fair agreement between both numerical and experimental results has been obtained. In general, numerical results follow the same trend that the experimental ones. The minimum local values of the heat transfer coefficient occurs at about $85°$ from the stagnation point, whereas the maximum values are reached at the stagnation point and at the rear end of the cylinder. As observed in $Re_D = 7200$ (see [15]), large differences from experiments are found to occur in the back size of the cylinder as the flow fluctuations are the largest which makes more difficult experimental measurements [23]. When comparing both Reynolds numbers (see figure 5.3), i.e, $Re_D = 7200$ and $Re_D = 21600$, it can be observed the increasing of inertial effects due to the increasing of Reynolds number which lead to the earlier separation of the boundary layer. Indeed, there is a displacement of the location of the minimum Nusselt number at $Re_D = 21600$ towards the stagnation point. The variation of the Nusselt number in the rear zone of the cylinder is smoother at $Re_D = 7200$ and a secondary peak is observed for $Re_D = 21600$ (at about $118°$). By increasing the Reynolds number from $Re_D = 7200$ to $Re_D = 21600$, the overall magnitude of the Nusselt number increases by a factor of 2 from 52.2 to 101.1 The value reported on the experiments was 103.4 (for $Re_D = 21600$), being the average difference between both numerical and experimental results of about 2.2%.

5.4 Results and discussion

5.4.1 Wind speed effects

As aforementioned, simulations have been conducted to study the wind effects around the PTC for two Reynolds numbers based on the aperture $Re_{W1} = 3.6 \times 10^5$ and $Re_{W2} = 1 \times 10^6$ and different pitch angles of $\theta = 0°$, $\theta = 45°$, $\theta = 90°$, $\theta = 135°$, $\theta = 180°$, $\theta = 270°$. Thereafter, these effects are analysed in terms of the average forces on the parabola, the flow configurations and the instantaneous flow.

Averaged forces

The average forces on the parabola have been validated respect to the experimental data [9] in the previous work [15]. To that end, the wind flow was studied around a typical LS-2 parabolic trough solar collector (without solar receiver) as proposed in the experimental study [5] and simulations were performed for a full-scale case with a Reynolds number about 2×10^6. In the present work, drag and lift coefficients have been computed for the PTC under study at different pitch angles and for both Reynolds numbers. The comparison with experimental measurements and those obtained for the LS-2 PTC are depicted in figure 5.4.

As can be seen from figure 5.4, numerical results obtained are almost within the error-bars of experimental measurements from the wind-tunnel data [9]. Discrepancies between computed and measured aerodynamic coefficients are mainly due to the unsteady flow behaviour and ground effects, which may affect the flow structures and separations behind the PTC and requires long measurement duration. The averaged aerodynamic coefficients at both Reynolds numbers exhibit an almost identical profile, which proves the stability of the aerodynamic coefficients at this range of Reynolds number. The predicted results are also in agreement with the experimental observations of Hosoya et al. [9]. In their scaled-down experimental tests carried out at Reynolds numbers $Re < 5 \times 10^4$, they concluded that beyond $Re = 5 \times 10^4$ load coefficients were independent of the Reynolds numbers, being thus directly extrapolated to a full-scale PTC. In the light of the load coefficients here presented, the aforementioned hypothesis of Hosoya et al. [9] can be confirmed. It is also worth noting that the independence of averaged aerodynamic coefficients with Reynolds numbers is also commented in other experimental results [24]. However, it was mentioned that it could be affected where the leading edge is close to the alignment with the stream causing some errors on the lift coefficient [24]. Yet, there are also some differences between numerical results of the LS-2 PTC and Eurotrough PTC which are due to the geometry of both solar collectors. It should be pointed out that from a numerical point of view the results presented for the LS-2 are statistically more converged in time than those for the Eurotrough. This is due to the more com-

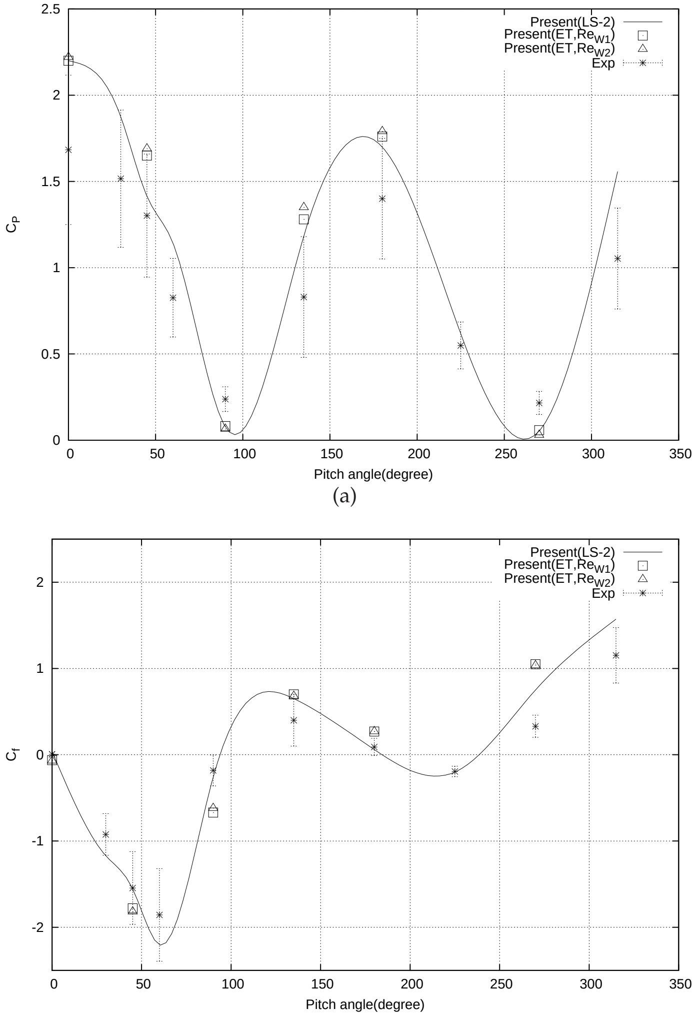

(a)

(b)

Figure 5.4: Predicted and measured aerodynamic coefficients for the LS-2 and the Eurotrough PTC.Wind speed effect and comparison with wind-tunnel data [9].(a)drag and (b)lift coefficients.

Table 5.2: Variation of the ratio of the non-dimensional recirculation length (L_r/W) to collector aperture with pitch angle and comparison between both Reynolds numbers

Pitch angle	$\theta = 0°$	$\theta = 45°$	$\theta = 90°$	$\theta = 135°$	$\theta = 180°$	$\theta = 270°$
$Re_{W1} = 3.6 \times 10^5$	7.65	2.21	0.09	1.6	9	0.2
$Re_{W2} = 1 \times 10^6$	8.32	3.06	0.1	1.47	8.3	0.17

plex grid used in the simulation of the Eurotrough PTC. In the latter, the geometry considered also included the receiver tube (which was not included in the LS-2 simulations), which imposes a large difference in scales between the parabola and the receiver. Thus, in the numerical simulations the explicit algorithm requires smaller time-steps (of about 5×10^{-5}) for solving all the relevant temporal scales of the flow, dominated by the flow around the receiver. This decrease in the time-step, together with the complex flow around the receiver impose larger simulation time in order to reach a statistical averaged flow.

Time-averaged flow

The time-averaged flow is also studied for different pitch angles and compared for both Reynolds numbers. Different structures and recirculation regions are encountered around the collector and the HCE. These flow structures are strongly related to the collector orientation and the pitch angle. The effect of the wind speed on the structures and recirculation regions observed around the PTC has also been assessed. By increasing the Reynolds number, the flow pattern does not change and the recirculation regions are similar to those found at $Re_W = 3.6 \times 10^5$ with small variation of the recirculation length behind the parabola as shown in figure 5.5.

The recirculation length for different pitch angles and for both Reynolds number is determined and presented in table 5.2. It can be seen from this table that the recirculation length is almost in the same range for both Reynolds numbers. This similarity has also been depicted in the comparison of averaged streamlines for both Reynolds numbers (see figure 5.5). However, in general terms it is observed that the recirculation length enlarges with the Reynolds number when the concave surface of the parabola is exposed to the wind direction, i.e $\theta < 90°$, and shrinks for the convex surface configuration ($\theta > 90°$).

At vertical position of $\theta = 0°$, a large recirculation region is observed behind the PTC with a maximum drag and minimum lift forces. This region increases with the Reynolds number and extends up to $8.32W$ at $Re_{W2} = 1 \times 10^6$. By moving the PTC to a pitch angle of $45°$, the recirculation decreases compared to the vertical position

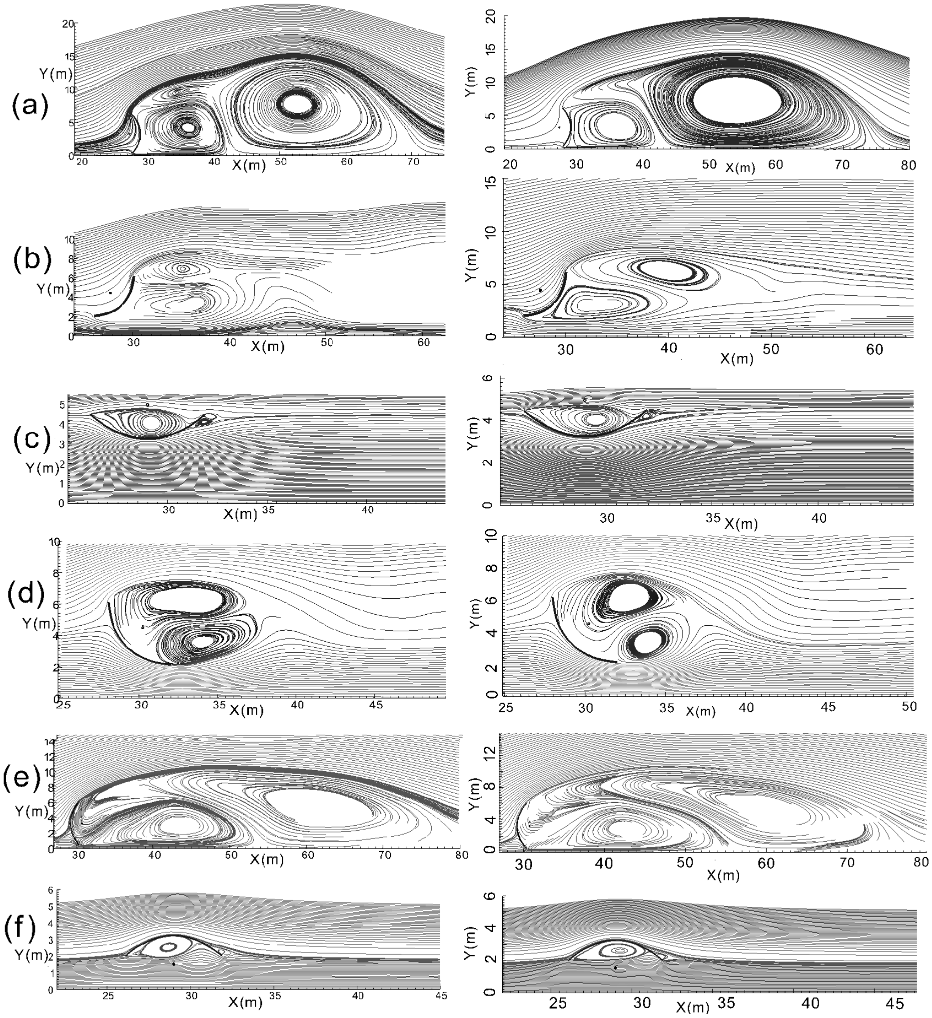

Figure 5.5: Streamlines for the time-averaged flow around the parabolic collector for different pitch angles: (a) $\theta = 0°$, (b) $\theta = 45°$, (c) $\theta = 90°$, (d) $\theta = 135°$, (e) $\theta = 180°$, (f) $\theta = 270°$. Comparison between both Reynolds numbers: Re_{W1} (left) and Re_{W2} (right).

and the shear layer is reduced. However, its length at Re_{W2} is almost a 30% larger than for Re_{W1} extending up to $3.06W$. The drag coefficient decreases whereas the absolute value of the lift coefficient increases.
The minimum of recirculation length occurs at the horizontal position of $90°$, where only small eddies are encountered in the leeward side of the PTC. This value is about $0.1W$ for both Reynolds numbers. The drag forces also reach their minimum values at this position. At a pitch angle of $135°$, the recirculation region enlarges again and a pair of medium-sized eddies are formed behind the PTC where negative pressure is observed. However, due to the aerodynamic profile of the collector, the recirculation length shrinks with Reynolds number and extends up to $1.47W$ at Re_{W2}. By moving the PTC to the vertical position at $180°$, the recirculation length reaches a new maximum and similar to $\theta = 0°$ two large eddies are formed behind the PTC. The shear layer is again elevated and drag forces are also increased. Comparing both Reynolds numbers at this pitch angle, the recirculation length is about 7% smaller for the higher Reynolds number which is due to the convex surface configuration. When the PTC is placed at the stow position, i.e $\theta = 270°$, the recirculation region is sharply reduced similarly to the working position $\theta = 90°$. Therefore, the drag forces decrease as well. At this position, the recirculation length remain almost unchanged with the Reynolds number around $0.2W$.

Heat transfer around HCE

As it has been discussed in the previous work [15], the convection taking place around the HCE is divided into forced convection (for pitch angles of $\theta = 0°, 45°, 90°$ and $270°$) and mixed (free and forced) convection (for pitch angles of $135°$ and $180°$). In figure 5.6, the distribution of the local Nusselt number for different pitch angles together with the comparison between both Reynolds numbers is shown. According to this figure, the profile of Nusselt number around the HCE is affected with the pitch angle and the displacement of the fluid structure around the HCE due to the tilt of the parabola. At higher wind speed, i.e. higher Reynolds numbers, the profile of Nusselt number follows a similar trend to that observed at the lower speed Re_{W1}. However, there is an increase in the magnitude and the peaks become more pronounced at all pitch angles. Moreover, the effect of the parabola and the ground becomes more significant with increasing the Reynolds number. While at the lower Reynolds number the local distribution of the Nusselt number was observed to follow the same trend to that of a circular cylinder in cross flow [15], this is not the case for Re_{W2}. This can be clearly observed in figure 5.7, where the distribution at pitch angles of $\theta = 90°$ and $\theta = 270°$ (working and stow modes), together with the circular cylinder in cross-flow are depicted. Large differences in the behaviour are obtained in the rear zone. At these positions, the combined effect of the parabola and the ground tend to reduce the large fluctuations of the near wake leading to a smoother distribution of the Nusselt number in the rear zone especially when it comes to the minimum and maximum magnitudes.

Table 5.3 summarizes the average, front stagnation, maximum and minimum Nusselt numbers (Nu_{avg}, Nu_{fsp}, Nu_{max}, Nu_{min}, respectively) together with the location where the extrema occurs for both Reynolds number Re_{W1} and Re_{W2}. These results are also compared with available experimental data [23] and the correlation of Zukauskas [25], for a circular cylinder and the numerical results presented in section 5.3.

As expected, the higher the Reynolds number, the higher the average magnitude of the Nusselt number. Furthermore, compared to the circular cylinder in cross flow at the same Reynolds number there is a reduction in the average Nusselt number. This is mainly due to the effect of the parabola which is desirable as it reduces the heat losses from the HCE, thus improving the performance of the PTC. When the parabola is placed at the vertical position of $\theta = 0°$, the averaged Nusselt number is increased by 70% compared to the lower wind speed case and reduced to 59% compared to the circular cylinder in cross flow case. At a pitch angle of $\theta = 45°$, the averaged Nusselt number is increased by 68% compared to the lower wind speed case and reduced to 40% compared to the circular cylinder in cross flow case. Although the effect of the parabola is less important than the vertical position $\theta = 0°$, the peaks for a pitch angle of $45°$ increase considerably at high wind speed (see also figure 5.6-b). The profile of Nusselt number still follows the tilt of the parabola and remains unchanged with increasing the Reynolds number. The distribution of the Nusselt number at the working position $\theta = 90°$ is symmetric (see figure 5.6-c) and its averaged magnitude increased by 85% when compared to the lower wind speed case. At a pitch angle of $\theta = 135°$, the averaged Nusselt number is increased by 72% compared to the lower wind speed case and reduced to 55% compared to the circular cylinder in cross flow case. At this position mixed convection occurs and the profile of Nusselt number is quite different to that of the circular cylinder in cross flow. The effect of wind speed is significant and the peaks increase sharply compared to the lower wind speed which exhibits a flatter profile (see figure 5.6-d). A similar behaviour takes also place at $\theta = 180°$ where mixed convection occurs. The averaged Nusselt number at Re_{W2} is a 61% higher than at Re_{W1} and about 64% compared to the circular cylinder. By moving the PTC to the stow position $\theta = 270°$, the Nusselt number profile is also symmetric (see figure 5.6-f) and similar to the working position $\theta = 90°$. The averaged Nusselt number is a 62% higher at Re_{W2} compared to the lower wind speed case and 30.5% compared to the circular cylinder.

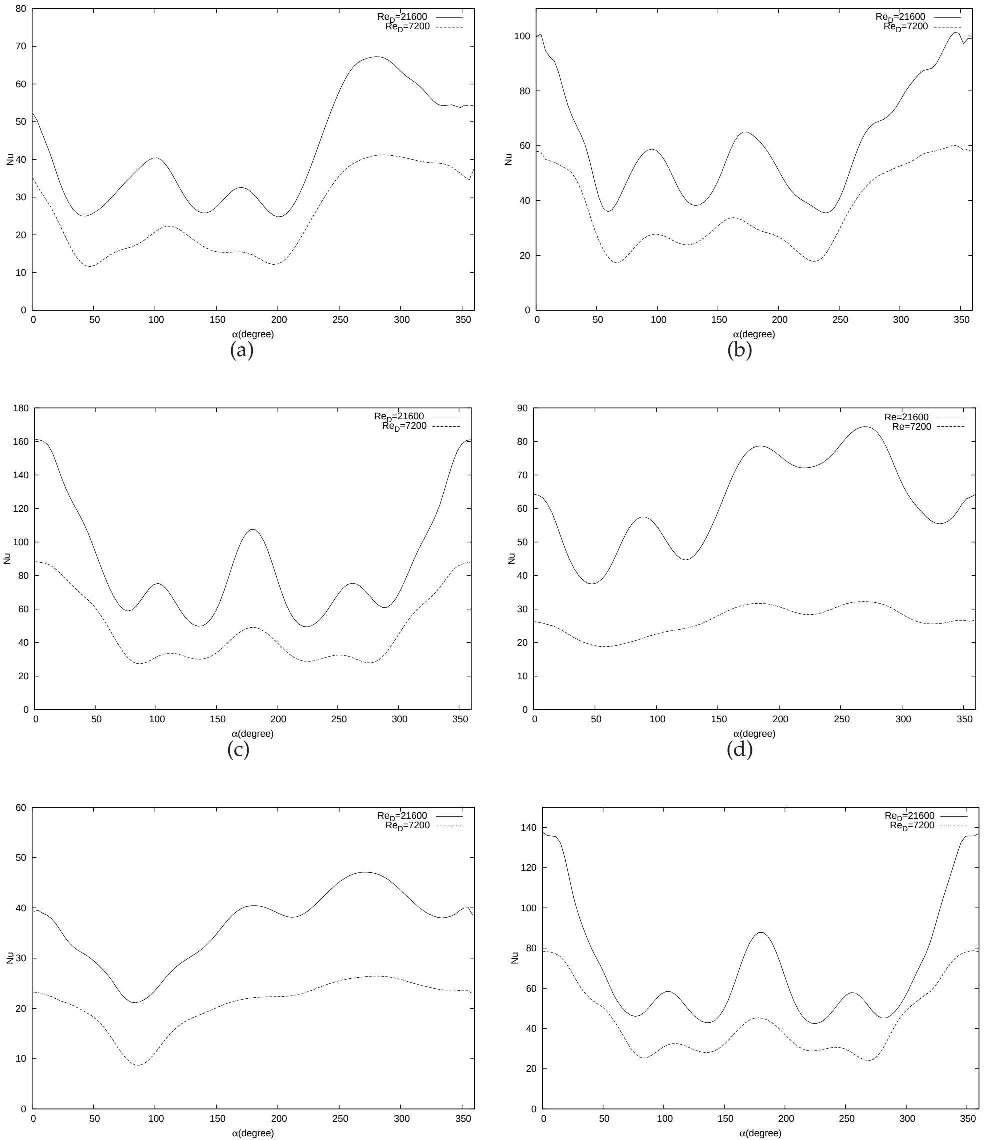

(a) (b) (c) (d) (e) (f)

Figure 5.6: Variation of the local Nusselt number around the HCE for different wind speed at (a) $\theta = 0°$ (b) $\theta = 45°$ (c) $\theta = 90°$ (d) $\theta = 135°$ (e) $\theta = 180°$ (f) $\theta = 270°$

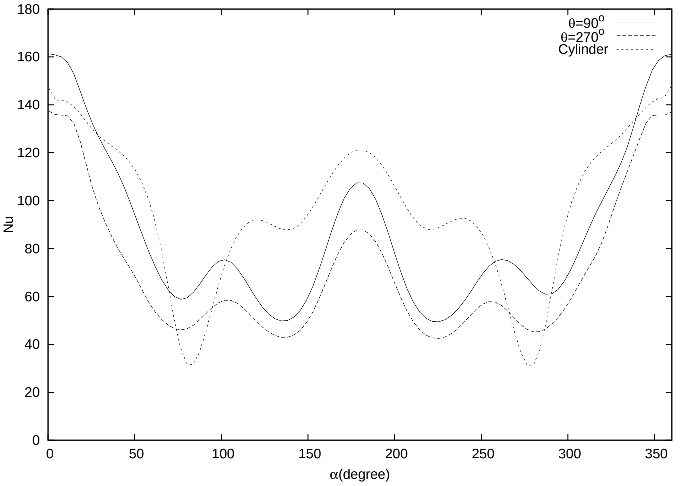

Figure 5.7: Comparison of the profile of Nusselt number for horizontal positions ($\theta = 90^\circ$ and $\theta = 270^\circ$) with the Nusselt number for the circular cylinder in cross flow case (without parabola) at $Re_D = 21600$

Table 5.3: Numerical data of averaged, front stagnation, maximum and minimum Nusselt numbers for each pitch angle and comparison with experiments [23] and the correlation of Zukauskas [25]

Position	Nu_{avg}		Nu_{fsp}		$Nu_{max}/Position$		$Nu_{min}/Position$	
	Re_{W1}	Re_{W2}	Re_{W1}	Re_{W2}	Re_{W1}	Re_{W2}	Re_{W1}	Re_{W2}
0°	24.5	41.6	33.1	52.3	41.4/289.5°	69.3/265.0°	9.5/196.8°	21.8/203.2°
45°	36.4	61.0	58.0	99.8	61.2/350.9°	104.2/347.8°	15.9/67.5°	31.1/56.1°
90°	47.4	87.8	86.0	161.3	86.0/0.0°	161.5/1.89°	27.3/222.0°	46.4/222.0°
135°	25.1	54.6	25.2	55.0	32.4/269.6°	71.7/182.4°	15.1/64.6°	37.1/48.3°
180°	22.5	36.3	23.7	39.3	29.1/269.5°	47.9/269.5°	7.4/85.9°	19.5/80.4°
270°	43.4	70.3	78.2	138.0	78.9/355.8°	139.8/350.5°	21.1/273.4°	39.9/281.7°
Cylinder	52.2	101.1	86.0	146.7	86.6/357.4°	147.7/359.5°	17.4/272.2°	8.7/78.5°
Exp [23]	49.5	103.4	88.0	148.0	90.3/9.9°	150.1/15.7°	5.5/95.7°	20.9/85.2°
Corr [25]	47.3	91.3	-	-	-	-	-	-

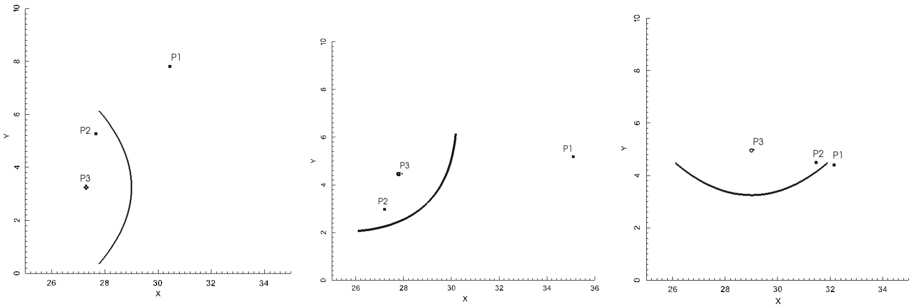

(a) (b) (c)

Figure 5.8: Location of the computational probes. (a) $\theta = 0°$, (b) $\theta = 45°$ and (c) $\theta = 90°$

5.4.2 Unsteady-state flow

The study of the unsteady flow field around the PTC at different pitch angles might be useful to gain insight into the flow behaviour in order to be able of controlling undesirable fluctuating forces. It should be borne in mind that the collector structure should sustain wind loads as well as keep accurate sun tracking. Vortex shedding in the wake of the PTC induces alternating forces perpendicular to the wind direction which might affect its structure. These vortices, depending on the pitch angle, are shed at a determined frequency and might produce undesirable effects such as deflections, vibrations, torsional moments, resonance with the structure and, at the end, stresses leading to the structure failure. Thus, in order to study the unsteady behaviour, instantaneous flow structures and frequencies have been examined at three pitch angles of $\theta = 0°$, $\theta = 45°$ and $\theta = 90°$. These angles describe the three possible positions occupied by the parabola, i.e. vertical, inclined and horizontal positions.

Single-point measurements have been carried out by positioning probes at different locations around the parabola. The frequencies of the fluctuations of the cross-stream velocity component have been computed by using the Lomb periodogram technique [26] and the resulting spectra have been averaged in the periodic direction. For the sake of brevity only 3 probes for each pitch angle are shown and compared for both Reynolds numbers. Only the most relevant results are here presented. The location of these probes are given in figure 5.8.

For all pitch angles, and due to the sharp edges of the parabola the fluid undergoes a rapid transition to turbulence. Depending on the pitch angle, the sharp edges produce flow separation which prevents the pressure from recovering (large recirculation region behind the parabola) and therefore, a high pressure drag is observed.

The separated flow at the sharp edges forms a shear-layer which resembles to be much like that formed behind a square cylinder or a normal plate [27]. These shear layers are characterised by the formation of instabilities which cause the fluid to become unstable in the presence of sharp corners. These instabilities increase in amplitude and accumulate into large vortical structures which are shed into the wake. As it will be further explained, depending on the pitch angle the level of coherence of these structures might form a turbulent wake similar to a von Kármán vortex street.

The analysis of the unsteady flow structures around the PTC shows the formation of stable vortices behind the parabola for most pitch angles. In figure 5.9 the velocity flow field of the three pitch angles and both Reynolds numbers (Re_{W1} and Re_{W2}) are depicted. Qualitatively, the instantaneous flow field are quite similar for both Reynolds numbers. A large separated zone is observed at $\theta = 0°$. The turbulent flow in the detached region produces a large depression region in the back of the PTC being the responsible for the large value of the drag coefficient obtained. The shear layer is more elevated at this position and the flow seems to follow the curvature of the PTC. However, the height of the recirculation zone decreases as the Reynolds number increases and the flow becomes more turbulent. Similar to previous observations [15], the height of the detached flow tends to decrease as the pitch angle moves from $\theta = 0°$ to $\theta = 90°$. The latter is the most favourable position for the PTC to work in terms of both unsteady forces and magnitude of averaged aerodynamic coefficients.

The structures formed at the different pitch angles are also observed by means of the instantaneous pressure map (see figure 5.10). A striking fact is that depending on the pitch angle the wake structure is completely different.

Starting from $\theta = 0°$, shear-layer instabilities at both sides of the parabola are observed (see figure 5.10a). These structures grow-up, but as a consequence of the interaction of the bottom shear-layer with the ground, the transverse motion of the separated shear layers is suppressed with the formation of vortices flowing downstream in a parallel manner. As a result, the level of coherence of the flow is low and only a small peak in the spectrum of the cross-stream velocity fluctuations is observed. This peak is captured at probe P2 (see figure 5.11) for Re_{W2} at $St_W = \frac{fW}{U_{ref}} = 0.34$. The peak is more pronounced at the higher Reynolds number than for the lower one but still it can be seen at $St_W = 0.28$ as a small footprint in the energy for Re_{W1} .

At $\theta = 45°$, as the bottom corner moves off the ground, both shear-layers are allowed to interact and vortices shed into the wake form a von Kármán-like vortex street (see figure 5.10b). By analysing the energy spectrum for cross-stream velocity fluctuations of probe P1 (see figure 5.12), one can notice that for the higher Reynolds number the peak in the energy is more distinguishable indicating a high coherence in the signal. In fact, the signal capture what can be identified as a double-peak mechanism. As the process of vortex shedding is asymmetric vortices formed at

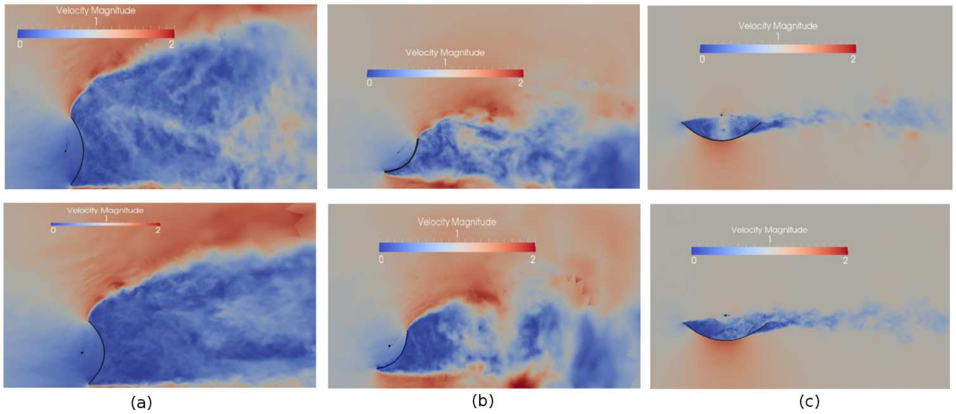

Figure 5.9: Instantaneous velocity field around the PTC for different pitch angles: (a) $\theta = 0°$, (b) $\theta = 45°$, (c) $\theta = 90°$ and Reynolds numbers: Re_{W1} (first row) and Re_{W2} (second row).

the top corner have a slight different period than those formed at the bottom corner leading to the double-peak observed in the energy spectrum. The same double-peak is also captured at the lower Reynolds number but at a lower frequency. Note also that at the lower Reynolds number, the flow is not so coherent and turbulent fluctuations are less energetic.

Finally, when the parabola is at $\theta = 90°$, leading-edge corner shear-layers instabilities move downstream and interacts with those structures formed in the wake of the receiver, breaking down into more complicated and disorganised structures near the trailing-edge corner (see figure 5.10c). As a result, the energy spectrum around the PTC at this position can not capture a distinguishable peak corresponding to the vortex shedding phenomenon (see figure 5.13).

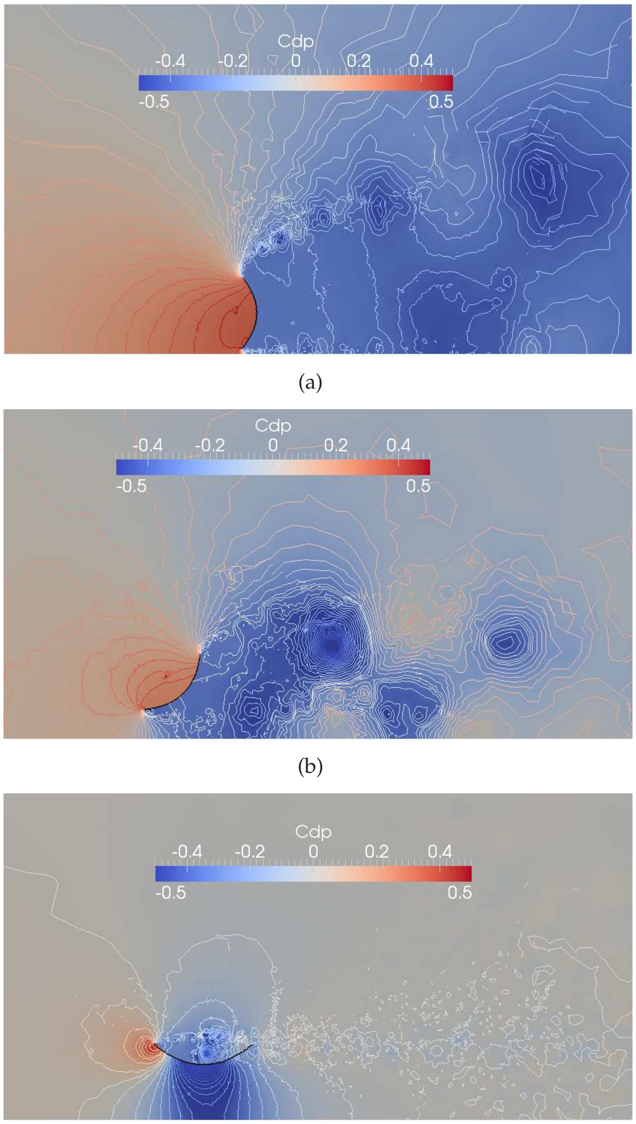

(a)

(b)

(c)

Figure 5.10: Instantaneous pressure contours for pitch angle: (a) $\theta = 0^\circ$, (b) $\theta = 45^\circ$ and (c) $\theta = 90^\circ$ at Re_{W2}.

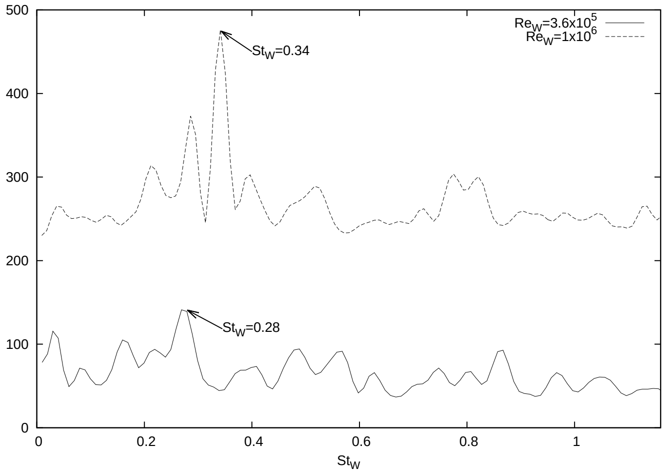

Figure 5.11: Energy spectrum of the cross stream velocity fluctuations at P2 probe near to the PTC (see figure for details 5.8) for pitch angle $\theta = 0°$ and comparison between both Reynolds numbers.

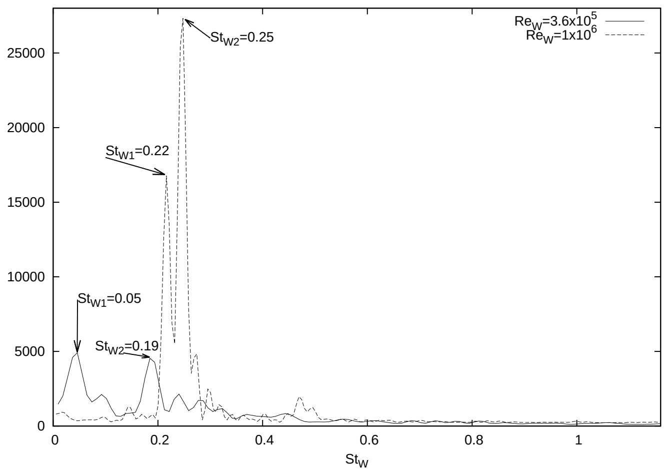

Figure 5.12: Energy spectrum of the cross stream velocity fluctuations at P1 probe near to the PTC (see figure for details 5.8) for pitch angle $\theta = 45°$ and comparison between both Reynolds numbers.

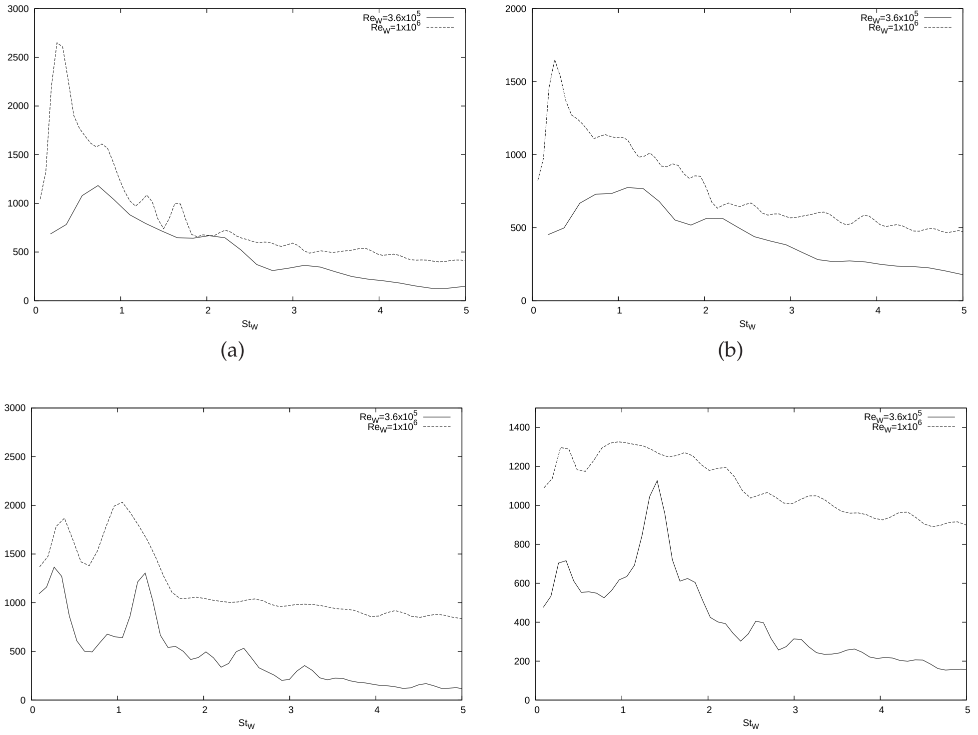

(a) (b)

(c) (d)

Figure 5.13: Energy spectrum at two probes around the PTC (P1 for the top, P2 for the bottom) for pitch angle $\theta = 90°$ and comparison between both Reynolds numbers. (a and c) stream-wise and (b and e) cross stream velocity fluctuations.

For all pitch angles, the observed frequencies are better captured for the high Reynolds number where the energy peak is more pronounced. From the stability point of view of the PTC, even though the magnitude of the drag forces at vertical positions are higher, turbulence fluctuations are more important at intermediate positions ($0° < \theta < 90°$). At these positions, the interaction between the shear-layer formed at both corners of the parabola produces an unsteady flow with a highly coherent vortex shedding which might lead to vibrations and the horizontal position is also demonstrated to be the most favourable position as it presents the minimum drag forces and turbulence fluctuations.

In addition, the spectral analysis is also carried out around the HCE to detect the relevant frequencies related to the receiver tube. Depending on the pitch angle, vortex shedding behind the HCE is also detected (see figure 5.14). Similar to the parabola, it is better captured at the higher Reynolds number but less coherent than the signal captured in the flow past a circular cylinder (see for instance [28]). This is due to the interaction of the flow with the parabola and to the turbulent fluctuations that this interaction produces which might be seen as broaden peaks (see for instance figure 5.14b,c) being the energy distributed along a large range of frequencies.

In spite of this, vortex shedding is captured and the results show that as the pitch angle increases from $0°$ to $90°$ the vortex shedding frequency increases and approaches to the typical value encountered in circular cylinder $St_D = \frac{fD}{U_{ref}} = 0.2$ [29, 30]. Indeed, the value of Strouhal number turns from $St_D = 0.05$ at pitch angle $\theta = 0°$ to $St_D = 0.19$ at pitch angle $\theta = 90°$. This can be explained by the effect of the parabola on the HCE which decreases by moving to the horizontal position. It should be pointed out that the unsteady flow and spectral analysis presented in this work for three pitch angles, i.e. $0°$, $45°$ and $90°$ can be extrapolated to the other positions because of the similarity of the flow configuration.

5.5 Conclusions

In the present work, a numerical study based on LES of the fluid flow and heat transfer around a parabolic trough solar collector and its receiver tube has been performed. The effects of wind speed and pitch angle on the aerodynamic behaviour and heat transfer characteristics around the PTC at Reynolds numbers similar to that encountered in working conditions have been addressed. It has been concluded that the averaged aerodynamic coefficient are stable with the Reynolds numbers in conformity with experimental results from literature. Furthermore, the structures and recirculation region observed in the time-averaged flow around the PTC and the HCE are quite similar for the Reynolds numbers studied. However, a small variation of the recirculation length behind the parabola has been identified due to the aerodynamic profile and depending to the collector orientation. Heat transfer coefficients

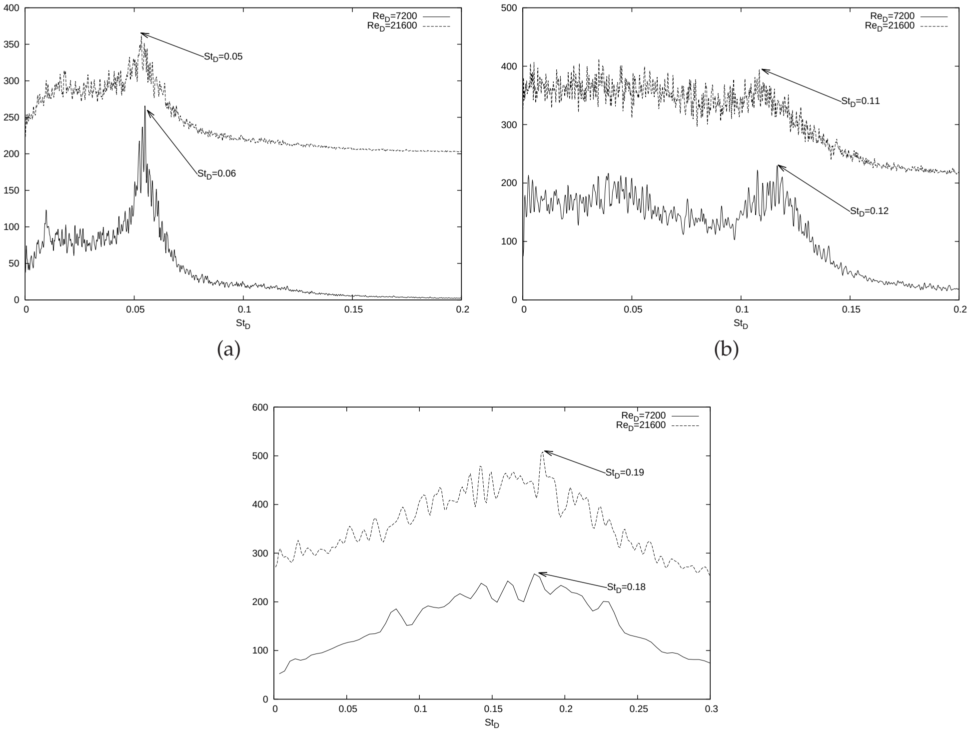

(a)

(b)

(c)

Figure 5.14: Energy spectrum around the HCE (at probe P3) for pitch angle: $\theta = 0°$, $\theta = 45°$ and $\theta = 90°$ and comparison between both Reynolds numbers.

around the HCE are also calculated and compared for different pitch angles and wind speeds. The distribution of Nusselt number for the higher wind speed shows a similar trend to the lower wind speed with higher magnitude and significant peaks. By studying the unsteady flow around the PTC, undesirable effects on the stability of the collector have been addressed for different pitch angles. Indeed, instantaneous flow structures and frequencies have been studied and compared for different orientations and Reynolds numbers. It has been observed that the turbulence is incoherent in the vertical position and becomes much more coherent by moving to intermediate positions allowing the interaction between upper and lower shear layers. This interaction is the consequence of the formation of a von Kármán-like vortex street and has been clearly detected in different stations. In general, the observed frequencies around the PTC are better captured at high Reynolds number and turbulence fluctuations are more important at inclined position. As a result, care must be taken when operating the collector at these positions, specially under high wind loads, as these turbulent fluctuations might be responsible for vibrations and stresses which lead to structure failure. Similar to the parabola, vortex shedding frequency has also been detected behind the HCE. This frequency varies with the pitch angle and approaches to the typical value encountered in circular cylinder when the parabola is placed at horizontal position.

References

[1] R. Foristall. Heat transfer analysis and modeling of aparabolic trough solar receiver implemented in engineering equation solver. Technical report, National Renewable Energy Laboratory(NREL), 2003.

[2] O. García-Valladares and N. Velázquez. Numerical simulation of parabolic trough solar collector: improvement using counter flow concentric circular heat exchangers. *International Journal of Heat and Mass Transfer*, 52(3):597–609, 2009.

[3] R.V. Padilla, G. Demirkaya, D.Y. Goswami, E. Stefanakos, and M. Rahman. Heat transfer analysis of parabolic trough solar receiver. *Applied Energy*, 88(12):5097–5110, 2011.

[4] A.A. Hachicha, I. Rodríguez, R. Capdevila, and A. Oliva. Heat transfer analysis and numerical simulation of a parabolic trough solar collector. *Applied Energy*, 111:581–592, 2013.

[5] J.A. Peterka and R.G. Derickson. Wind load design methods for ground-based heliostats and parabolic dish collectors. Technical Report SAND 92-7009, Sandia National Laboratories, 1992.

[6] J.A. Peterka, J.M. Sinou, and J.E. Cermak. Mean wind forces on parabolic-trough solar collectors. Technical Report SAND 80-7023, Sandia National Laboratories, 1980.

[7] D.E. Randall, D.D. McBride, and R.E. Tate. Steady-state wind loading on parabolic-trough solar collectors. Technical Report SAND 79-2134, Sandia National Laboratories, 1980.

[8] D.E. Randall, R.E. Tate, and D.A. Powers. Experimental results of pitching moment tests on parabolic-trough solar-collector array configurations. Technical Report SAND 82-1569, Sandia National Laboratories, 1982.

[9] N. Hosoya, J.A. Peterka, R.C. Gee, and D Kearney. Wind tunnel tests of parabolic trough solar collectors. Technical Report NREL/SR-550-32282, National Renewable Energy Laboratory, 2008.

[10] B. Gong, Z. Wang, Z. Li, J. Zhang, and X. Fu. Field measurements of boundary layer wind characteristics and wind loads of a parabolic trough solar collector. *Solar energy*, 86(6):1880–1898, 2012.

[11] N. Naeeni and M. Yaghoubi. Analysis of wind flow around a parabolic collector (1) fluid flow. *Renewable Energy*, 32(11):1898–1916, 2007.

[12] N. Naeeni and M. Yaghoubi. Analysis of wind flow around a parabolic collector (2) fluid flow. *Renewable Energy*, 32(11):1259–1272, 2007.

[13] W. Rodi. Comparison of LES and RANS calculations of the flow around bluff bodies. *Journal of Wind Engineering and Industrial Aerodynamics*, 69:55–75, 1997.

[14] Z.T. Xie and I.P. Castro. LES and RANS for turbulent flow over arrays of wall-mounted cubes. *Flow Turbulence and Combustion*, 76(3):291–312, 2006.

[15] A.A. Hachicha, I. Rodríguez, J. Castro, and A. Oliva. Numerical simulation of wind flow around a parabolic trough solar collector. *Applied Energy*, 107:426–437, 2013.

[16] O. Lehmkuhl, A. Baez, I. Rodríguez, and C.D. Pérez-Segara. Direct numerical simulation and large-eddy simultaions of the turbulent flow around a NACA-0012 airfoil. In *ICCHMT*, 2011.

[17] I. Rodríguez, O. Lehmkuhl, R. Borrell, and A. Oliva. Flow dynamics in the turbulent wake of a sphere at sub-critical Reynolds numbers. *Computers & Fluids*, 80:233–243, 2013.

[18] O. Lehmkuhl, I. Rodríguez, A. Baez, A. Oliva, and C.D. Pérez-Segarra. On the large-eddy simulations for the flow around aerodynamic profiles using unstructured grids. *Computers & Fluids*, 84:176–189, 2013.

[19] D. Aljure, I. Rodríguez, O. Lehmkhul, R. Borrell, and A. Oliva. Flow and turbulent structures around simplified cars models. In *Conference on Modelling Fluid Flow (CMFF'12)*, pages 247–254, Budapest, Hungary, 2012.

[20] O. Lehmkuhl, C. D. Pérez-Segarra, R. Borrell, M. Soria, and A. Oliva. TERMOFLUIDS: A new Parallel unstructured CFD code for the simulation of turbulent industrial problems on low cost PC Cluster. In I.H. Tuncer, Ü. Gülcat, D.R. Emerson, and K. Matsuno, editors, *Proceedings of the 2005 Parallel Computational Fluid Dynamics Conference*, volume 67 of *Lecture Notes in Computational Science and Engineering*, pages 275–282. Springer, 2007.

[21] E. Lüpfert, M. Geyer, W. Schiel, A. Esteban, R. Osuna, E. Zarza, and P. Nava. EUROTROUGH design issues and prototype testing at PSA. In *Proceedings of ASME International Solar Energy Conference- Forum 2001*, pages 289–394, Washington, DC, April 21-25. Solar Energy: The power to Choose.

[22] R.W.C.P. Verstappen and A.E.P. Veldman. Symmetry-preserving discretization of turbulent flow. *Journal of Computational Physics*, 187:343–368, 2003.

[23] J.W. Scholten and D.B. Murray. Unsteady heat transfer and velocity of a cylinder in cross flow-i. low freestream turbulence. *Int Journal of Heat and Mass Transfer*, 41(10):1139–1148, 1998.

[24] D.E. Randall, D.D. McBride, and R.E. Tate. Parabolic trough solar collector wind loading. *In American Society of Mechanical Engineers, Energy technology conference and exhibition*, 1:18–20, 1980.

[25] A. Zukauskas. Heat transfer from tubes in cross flow. *Advances in Heat Transfer*, 8:93–160, 1972.

[26] N. Lomb. Least-squares frequency analysis of unequally spaced data. *Astrophysics and Space Science*, 39:117–462, 1976.

[27] J.H. Gerrard. The wakes of cylindrical bluff bodies at low Reynolds number. *Philosophical Transactions for the Royal Society of London*, 288(A):351–382, 1978.

[28] O. Lehmkuhl, I. Rodríguez, R. Borrell, and A. Oliva. Low-frequency unsteadiness in the vortex formation region of a circular cylinder. *Physics of Fluids*, 25 (085109), 2013. doi:10.1063/1.4818641.

[29] U. Fey, M. König, and H. Eckelmann. A new Strouhal-Reynolds-number relationship for the circular cylinder in the range $47 < \mathrm{Re} < 2 \times 10^5$. *Physics of Fluids*, 10(7):1547–1549, 1998.

[30] M.M. Zdravkovich. *Flow around circular cylinders*, volume 2. Oxford University Press, 2003.

Chapter 6

Conclusions and further work

Given the scope of the use of concentrating solar power (CSP) technologies, parabolic trough solar collectors are an attractive technology to produce electricity from thermal solar energy. In this dissertation, a comprehensive methodology for modelling a parabolic trough solar collector (PTC) has been developed.

In the first chapter of the thesis a brief description of solar concentrating solar technology with a special emphasis on parabolic trough solar collectors is performed. The state-of-the-art in modelling PTC is presented and main objectives in optical, thermal and aerodynamic modelling of the PTC are depicted.

In Chapter 2, an optical model for determining the solar heat flux around the heat collector element (HCE) has been developed. The Finite Volume Method (FVM) for solving the radiative transfer equations has been first implemented and successfully tested in two-dimensional enclosures. This methodology has been applied to a solar collector by discretising the spatial and angular domain. However, two major drawbacks have been identified in this model: the high computational cost due to the spatial and angular discretisation of all the domain of the parabola which is huge compared to the solar receiver, and the modelling of solar radiation as a collimated beam without taking into account the finite size of the Sun. Therefore, a new optical model based on ray tracing and FVM techniques has been proposed to study the solar radiation around the solar receiver. The new model uses a numerical-geometrical approach that takes into account the optic cone and reduces the computational cost compared to the FVM solution. The accuracy of the new optical model has been verified with analytical and experimental results. The local concentration ratio (LCR) has been calculated around the HCE and different zones are depicted according to its distribution along the azimuthal direction. It has been shown, that the new optical model yields better results than the MCRT model for the conditions under study.

In addition, a general model based on an energy balance about the HCE to predict accurately the heat losses and thermal performances of a PTC has been developed in Chapter 3. Different elements of the solar receiver are discretised into several segments considering the non-uniform distribution of solar flux in the azimuthal direction given by the new optical model. The solar heat flux is determined as a pre-processing task and coupled to the energy balance model. The set of linear algebraic equations obtained from the discretisation of the governing equations are implemented with the corresponding boundary conditions and then solved using direct solver. The overall model has been validated with experimental measurements of irradiated and un-irradiated receivers. Heat losses and thermal efficiency are calculated and validated with Sandia Laboratories tests. The temperature profile of both absorber and glass envelope are depicted and has shown a similar trend to the solar flux distribution. Although, some discrepancies have been observed due to optical properties of the HCE and other unaccounted optical effects during the test operating, predicted results have shown good agreement with numerical and experimental results.

The convection heat losses to the ambient and the effect of wind flow on the fluid flow and heat characteristics around a parabolic trough solar collector has been carried out in Chapter 4. A numerical aerodynamic and heat transfer model based on Large Eddy Simulations (LES) has been developed. Simulations are performed for different configuration at Reynolds number of $Re_W = 3.6\times10^5$ based on the aperture of the parabolic collector and for various pitch angles ($\theta = 0°, 45°, 90°, 135°, 180°, 270°$). First, the LES model is verified on a circular cylinder in a cross low where pressure distribution and heat transfer characteristics around the circumference of the cylinder are validated with experimental data. The aerodynamic coefficients around the parabolic collector are then calculated and validated with experimental measurements form NREL Laboratory. It has shown that that the horizontal position $\theta = 90°$ is the most favourable position for the PTC to work where the drag forces are lower and increase by moving the PTC. Several recirculation regions are observed in the time-averaged flow which are strongly related to the collector orientation and the pitch angle. It was concluded that the stability of the mirrors are much affected by wind forces for pitch angle $\theta = 90°$, while the PTC structure stability is more affected by wind forces for pitch angle $\theta < 90°$. The Nusselt number are also calculated around the solar receiver for different pitch angles and compared to the circular cylinder in cross flow. From a thermal point of view, the positions $\theta = 135°$ and $180°$ are the most favourable where the Nusselt number is lower and the flow around the HCE is laminar.

In Chapter 5, the study conducted in Chapter 4 has been extended to a higher Reynolds numbers in order to analyse how the fluid flow and heat transfer are affected by the influence of a higher velocity. Large Eddy simulations are performed around a parabolic trough solar collector for Reynolds number of $Re_{W2} = 1\times10^6$ and various pitch angles. This Reynolds number corresponds to realistic working conditions for solar plants, i.e. the wind speed is about $3m/s$. Aerodynamic coefficients around parabolic collector are calculated and compared to that of the lower Reynolds number and to experimental data. Averaged and instantaneous velocity and pressures maps have been compared for different pitch angles and wind speeds. It has been shown, that the averaged aerodynamic coefficients exhibit an almost identical profile in the range of Reynolds number studied which has confirmed the hypothesis made in experimental measurements about the independence of the drag coefficients with the Reynolds number for $Re > 5 \times 10^4$. In the same way, the profile of Nusselt number has shown a similar trend for both wind speeds with larger and significant peaks at the higher wind speed case. A power spectra analysis has been carried out by positioning probes at different locations around the parabola. This analysis has shown that when the parabola is placed in the vertical position ($\theta = 0°$), turbulent vortices are irregular and without coherence, whereas at intermediate angles $0° < \theta < 90°$) due to the interaction of the shear layers, vortices shed are more coherent, with a pronounced peak at the vortex shedding frequency. From a stability point of view, the coherent turbulence might affect the collector structure by alternating forces perpendicular to the wind direction leading to stresses on the parabola. In this context, the vortex shedding frequency around the PTC and HCE have been determined for different pitch angles and for both Reynolds numbers.

Further work

The main outcome of the present Ph.D is the heat transfer and fluid dynamic study of a parabolic trough collector for concentrated solar power systems. The study has included the optical, thermal and aerodynamic behaviour of such collectors under different working conditions. The developed methodology has been validated with experimental measurements and analytical results from literature. However, different improvements and further investigations can be addressed to have a more realistic view of their behaviour taking into account realistic conditions in solar plant. One of these improvement could be the study of the fluid flow and heat transfer for a parabolic trough collector in a deep array of collectors placed in the solar field. Furthermore, an upgrade of the proposed correlations by taking into account the effect of wind and pitch angle on the convection heat transfer with the environment could be considered in the future.

Appendix A

First steps in the thesis

This thesis has been developed through many steps. First, a numerical code for solving Navier-Stokes equations was developed and applied to different study cases. This code was validated to benchmark cases such as: Smith Hutton problem [1], driven cavity flow problem [2] and thermal driven cavity [3].

The same methodology was afterwards applied to study a confined two dimensional flow of an incompressible fluid in a channel with a heated square cylinder placed symmetrically on the centre line (see figure A.1). This study case has been motivated from theoretical and experimental considerations, because of the wide occurrence of flow around bluff bodies in chemical and process engineering. This case might be considered as a starting point for the work developed within this thesis, as it deals with the fluid flow and heat transfer around bluff bodies. Thereafter, a brief description of the case and its main results are summarised.

A.0.1 Definition of the problem

The test case defined was a square cylinder with side b exposed to a constant free stream velocity at the inlet with a uniform velocity ($U_\infty = 1$) and a uniform temperature ($T_\infty = 0$). The blockage ratio $Bl = b/L_2$ is fixed to 5% ($L_2 = 20b$) as it has been proven (Sohankar [4]) that the boundaries are sufficiently far away and their presence has a little effect on the characteristics of the flow near the cylinder.
The total non-dimensional distance between the upper and the lower walls is $L_2 = 20$ and the total non-dimensional length of the channel is $L_1 = 26$. The non-dimensional distance between the inlet and the front surface of the cylinder is taken as $X_U = 8.5$ and the non-dimensional distance between the rear surface of the cylinder and the outlet surface is taken as $X_d = 16.5$.
The square cylinder is heated to a constant temperature $T_W (> T_\infty)$.

This case is defined by two dimensionless numbers:

$$Re = \frac{\rho U_\infty b}{\mu}$$

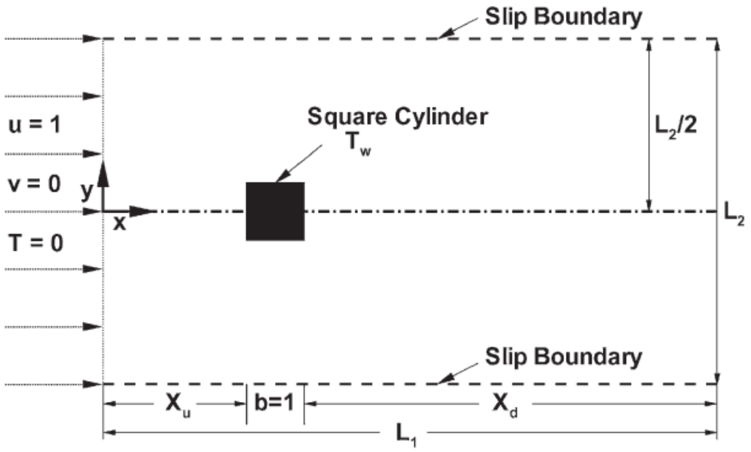

Figure A.1: Domain and boundary conditions

$$Pr = \frac{\mu c_P}{k}$$

The dimensionless boundary conditions of this problem can be written as follows.

- Top and bottom boundaries: $\left(\frac{\partial U}{\partial Y}\right) = 0, V = 0\ , \theta = 0$
- Surface of the cylinder: $U = 0, V = 0\ , \theta = 1$
- Inlet boundaries: $U = 1, V = 0\ , \theta = 0$
- Outlet boundaries: an artificial boundary of Orlanski [5] has been used, with the average non-dimensional stream-wise velocity $U_c = 1$ and χ is the dependent variable , U, V or T.

$$\frac{\partial \chi}{\partial \zeta} + U_c \frac{\partial \chi}{\partial X} = 0 \tag{A.1}$$

The finite volume method (FVM) is used for the integration of the discretised form of the governing equations over each control volume. The velocity-pressure coupling of the momentum equation is solved by means of a classical fractional step projection [6]. A staggered grid arrangement is used in which velocity components are stored at the midpoints of the cell sides to which they are normal. The pressure

and temperature are stored in the center of the cell. An explicit-second-order Adam-Bashford scheme is used for the convective term and a central difference is adopted for the time derivative term. The time step is calculated every time iteration by using CFL condition [7].
After a study of the grid independence, the mesh (165×132) has been selected as it captures quite good the details of the flow around the cylinder with a reasonable computational effort.

This problem is carried out numerically in 2-D and for different Reynolds numbers:

- Steady flow with $Re = 2, 10, 20, 40$.
- Unsteady flow with $Re = 80$ to 140 in steps of 20.

The Prandtl number has been fixed for all the numerical computations at 0.7 (as for air).

A.0.2 Results

Two different regimes depending on the Reynolds number are obtained:*i)* steady regime $Re < 40$ and *ii)* transient regime $Re > 40$. The steady regime is characterised by a recirculating region consisting of two symmetric vortices appears behind the cylinder. This recirculating region increases in size with the increase of Reynolds number (see figure A.0.2).

The recirculation length is calculated for different Reynolds numbers and shown in figure A.3(a). There is a good agreement with the empirical relation for circular cylinder under steady conditions with a maximum deviation of 7%.

The variation of the drag coefficient with Reynolds number is calculated and compared with experimental results of Shimizu [8] and numerical results of Sharma and Eswaran [9]. The present results follow the same trend and the agreement with is fairly good. The heat transfer is also studied around the square cylinder and isotherms are shown in figure A.0.2 for different Reynolds numbers $Re = 2, 10, 20, 40$. It can be seen from this figure that the front surface has the maximum crowding of the temperature contours, indicating the highest Nusselt number, as compared with the other surfaces of the cylinder.

The variation of the average Nusselt number for each surface with the Reynolds number is plotted in figure A.0.2 and compared with the empirical expression proposed by Sharma and Eswaran [9] for the square cylinder. As can be seen, the predicted numerical results are closer to the empirical expression proposed by Sharma

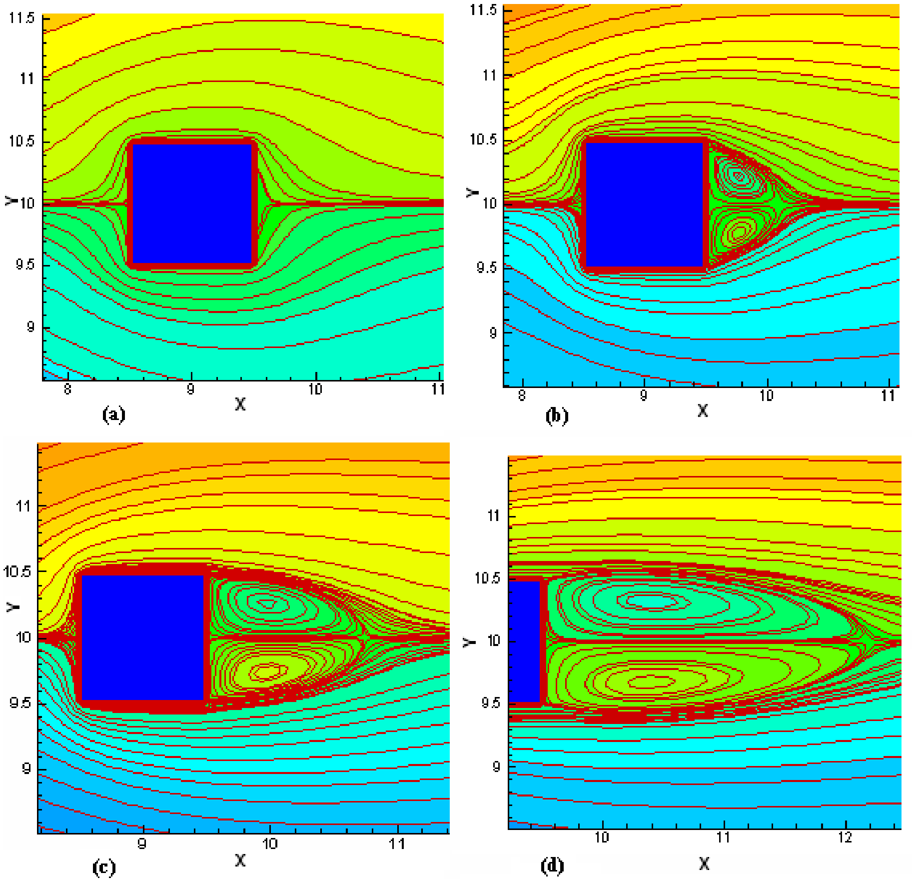

Figure A.2: Streamlines around the square cylinder for different Reynolds numbers :(a) Re=2, (b) Re=10, (c) Re=20, (d) Re=40

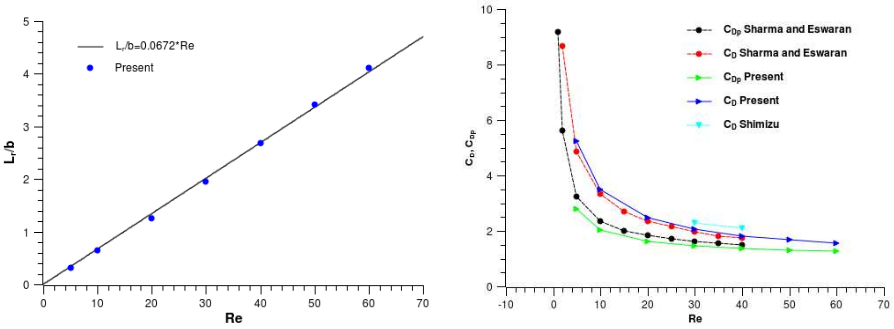

(a) (b)

Figure A.3: Variation of the (a) recirculation length and (b) drag coefficient together with pressure drag with Reynolds number

and Eswaran [9] for the calculation of the Nusselt Number for the square cylinder with a maximum of variation of 6%. The flow around the square cylinder becomes unsteady by $Re = 60$ [10, 11]. For the unsteady laminar regime simulations have been performed for Re=80, 100, 120, 140. Figure A.6 shows the instantaneous streamlines of the laminar vortex shedding near the square cylinder at $Re = 100$ for eight successive moments of the whole period separated by $\Delta t = \frac{p}{8}$ time units (p is the period of the vortex shedding) .
As can be seen from this figure, the vortices start to separate alternatively from the trailing edge of the cylinder and move downstream in a periodic flow because of the phenomenon of von Kármán vortex shedding.

In table A.1, the main average parameters obtained from the computations are compared to the results of Sharma and Eswaran [9]. As can be seen, a good agreement is obtained with maximum of deviation of 8% for the recirculation length L_r, 2% for the total and pressure drag C_{Dp}, 3% for the Nusselt number Nu and 7% for the Strouhal number. The largest deviations are mainly due to the difference on the grid and the numerical schemes adopted by Sharma and Eswaran [9].

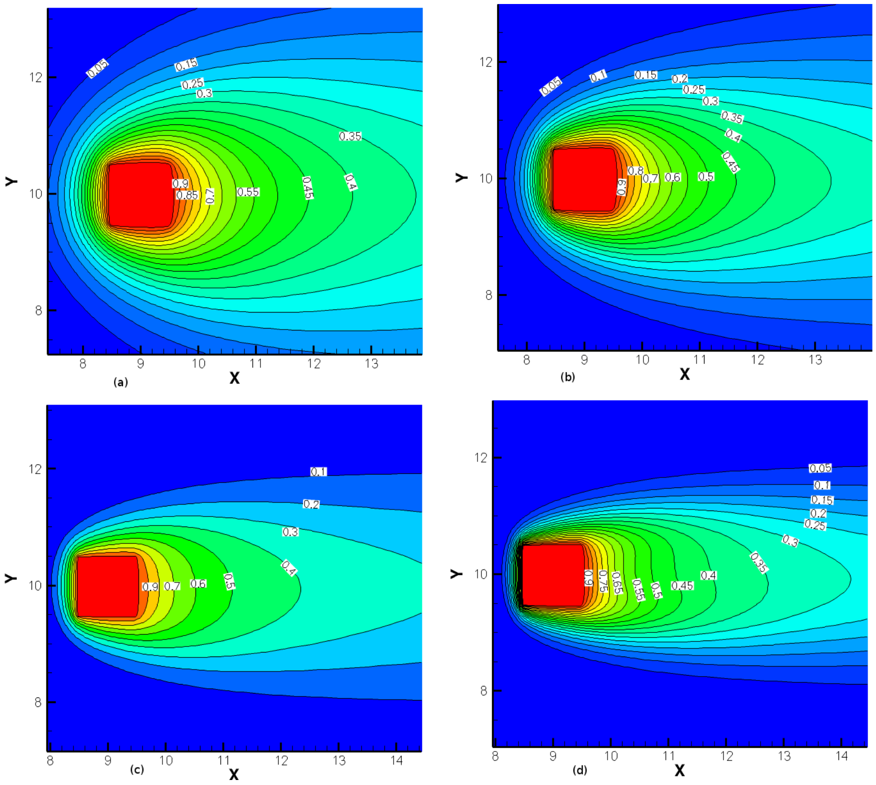

Figure A.4: Isotherms around the square cylinder for different Reynolds numbers :(a) Re=2, (b)Re=10, (c) Re=20, (d) Re=40

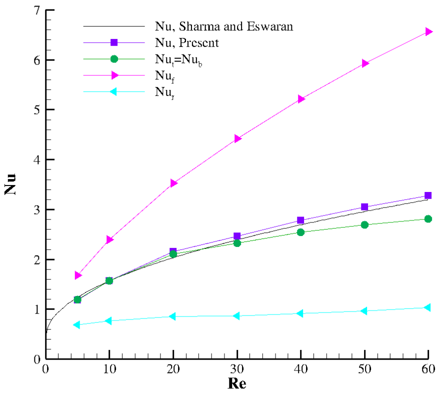

Figure A.5: Variation of Nusselt number for the cylinder(Nu) and each of its faces($Nu_t = Nu_b$, Nu_f, Nu_r) with Reynolds number

Table A.1: Variation of the main average parameter with Reynolds number and comparison with the results of Sharma and Eswaran [9]

Re	results	$L_r(\%error)$	$C_{Dp}(\%error)$	$C_D(\%error)$	$Nu(\%error)$	$St(\%error)$
80	present	2.228(6.38)	1.417(1.6)	1.549(0.9)	3.749(2.56)	0.136(2.22)
	num [9]	2.145	1.440	1.535	3.652	0.140
100	present	2.060(7.29)	1.445 (0.06)	1.502(0.53)	4.105(1.81)	0.1435(3.49)
	num [9]	1.920	1.444	1.494	4.032	0.1487
120	present	1.9162(8.24)	1.482 (1.9)	1.490(1.27)	4.417(0.98)	0.147(5.09)
	num [9]	1.770	1.454	1.472	4.374	0.155
140	present	1.783(7.79)	1.445 (0.06)	1.502(0.53)	4.704(0.31)	0.148 (6.32)
	num [9]	1.650	1.444	1.494	4.689	0.158

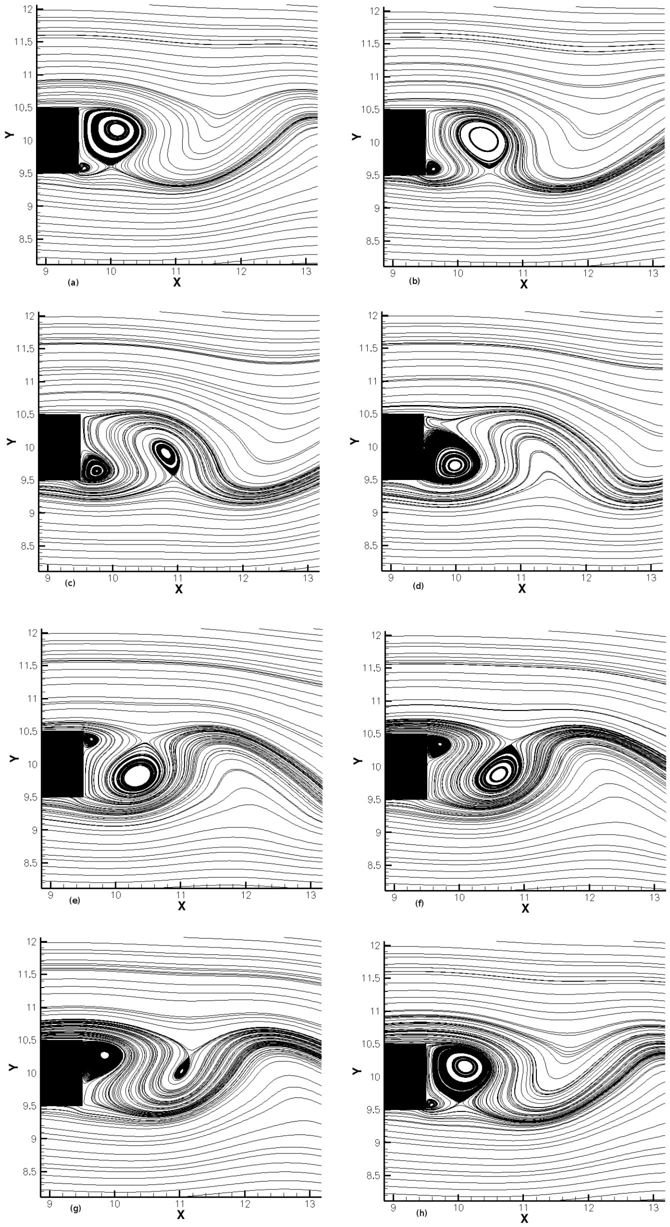

Figure A.6: Instantaneous streamlines near the square cylinder in eight successive moment of the vortex shedding at $Re = 100$

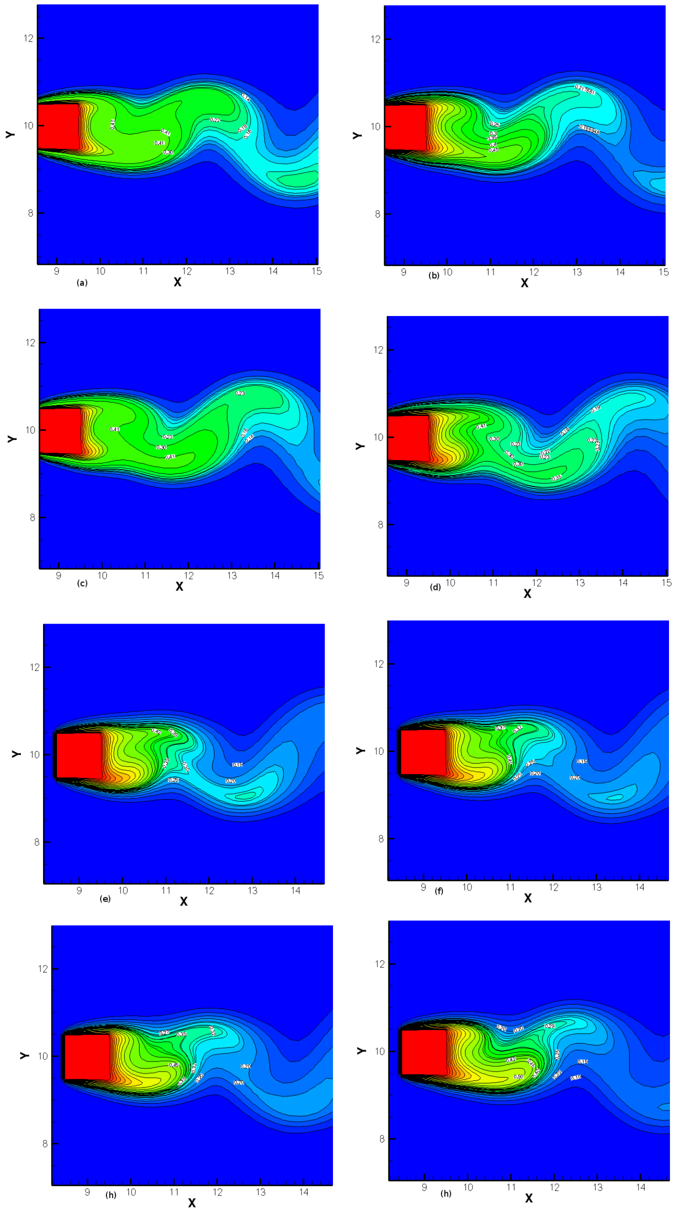

Figure A.7: Instantaneous isotherms near the square cylinder in eight successive moment of the vortex shedding at $Re = 100$

References

[1] R.M. Smith and A.G. Hutton. The numerical treatment of advection: a performance comparison of current methods. *Numerical Heat Transfer*, 5:439–461, 1982.

[2] U. Chia, K.N. Ghia, and C.T. Shin. High-Re solutions for incompressible flow using the Navier-Stokes equations and a multigrid method. *Journal of computational physics*, 48:378–411, 1982.

[3] G. de Vahl Davis. Natural convection of air in a square cavity: a bench mark numerical solution. *International Journal for Numerical Methods in Fluids*, 3(3): 249–264, 1983.

[4] C. Sohankar, C. Norberg, and L. Davidson. Low-Reynolds-number flow around a square cylinder at incidence: study of blockage, onset of vortex shedding and outlet boundary condition. *International Journal for numerical methods in fluids*, 26:39–56, 1998.

[5] I. Orlanski. A simple boundary condition for unbounded hyperbolic flows. *Journal of computational Physics*, 21:251–269, 1976.

[6] A.J. Chorin. Numerical solution of the navier-stockes equations. *Journal of computational physics*, 22:745–762, 1968.

[7] R. Courant, K. Friedrichs, and H. Lewy. Über die paratiellen differenzengleichungen der mathimatischen physik. *Mathematishe Annalen*, 100:32–74, 1928.

[8] Y. Shimizu and Y. Tanida. Fluid forces acting on cylinders of rectangular cross-section. *Trans. Japan Soc. Mech. Eng. B*, 44:2699–2706, 1978.

[9] A. Sharma and V. Eswaran. Heat fluid flow across a square cylinder in the two-dimensional laminar flow regime. *Numerical Heat Transfer*, Part A(45):247–269, 2004.

[10] A. Sohankar, C. Norber, and L. Davidson. Numerical simulation of unsteady low-Reynolds number flow around rectangular cylinders at incidence. *Journal of Wind Engineering and Industrial Aerodynamics*, 69:189–201, 1997.

[11] A. Sohankar, C. Norberg, and L. Davidson. Numerical simulation of unsteady low-Reynolds number flow around a square two-dimensional cylinder. In *Proc. 12 th Australian Fluid Mechanics Conf*, pages 517–520, Sydney, Australia, 1995. Solar Energy: The power to Choose.

Appendix B

Convection between the HTF and the HCE

The convection heat transfer coefficient between the HTF and the absorber tube has been calculated as commented in section 3.2.1 using the Gnielinski correlation [1] and assuming that the Nusselt profile at the absorber control volume is similar to an isothermal circular tube at the same temperature. However, the flow inside the HCE is turbulent with a non-uniform heat flux around the absorber wall. In order to look for a method which improves the calculation of the Nusselt number, a study of the turbulent heat transfer in the HCE with circumferentially varying heat flux is carried out. The study is based on the Ramm-Johannsen analysis[2] which was validated with experimental data. This analysis is restricted to cases where the heat flux variation $q(\phi)$ may be expressed in terms of Fourier series.

$$q(\phi) = \sum_{n=1}^{\infty} q_n(\phi) \tag{B.1}$$

where

$$q_n(\phi) = a_n cos(n\phi) + b_n sin(n\phi) \tag{B.2}$$

and

$$\int_0^{2\pi} q(\phi) d\phi = 0 \tag{B.3}$$

Under these conditions, the solution of the turbulent heat transfer is developed in [2] and yields to a dimensionless wall temperature T^* in the following form

$$T^*(\phi) = G_0 + \sum_{n=1}^{\infty} G_n(a_n cos(n\phi) + b_n sin(n\phi)) \tag{B.4}$$

where G_n are presents the circumferential temperature functions that depend parametrically on Reynolds and Prandtl numbers. The local Nusselt number at any angular position is given as

$$Nu_{\infty}(\phi) = \frac{2q(\phi)/q_0}{G_0 + \sum_{n=1}^{\infty} G_n(a_n cos(n\phi) + b_n sin(n\phi))} \tag{B.5}$$

In our case, the heat flux distribution around the absorber is approximated to a sinusoidal function and only the first harmonic is considered.

$$q(\phi) = q_0(1 + b_1 sin(\frac{\pi}{2} - \phi)) \tag{B.6}$$

where q_0 is the average heat flux around the circumference of the absorber and b_1 is determined in a manner that gives positive Nusselt number. Using this analysis, the dimensionless local wall temperature is given by a sinusoidal function

$$T^*(\phi) = G_0 + b_1 G_1 sin(\frac{\pi}{2} - \phi) = G_0 \left(1 + b_1 \frac{G_1}{G_0} sin(\frac{\pi}{2} - \phi)\right) \tag{B.7}$$

Compared to the correlation used in chapter 3, this analysis may give accurate solution of Nusselt and temperature distribution around the absorber wall but the profile of temperature will be sinusoidal and far from the real distribution that should follow the same trend as the solar flux (see figure B.1).

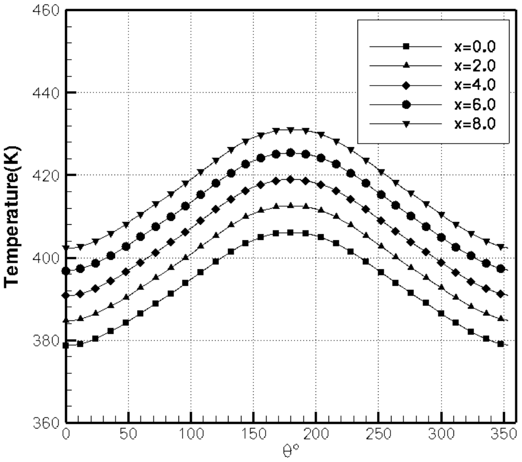

Figure B.1: Circumferential temperature distribution around the absorber tube for the case of Dudley et al. [3] ($I_b = 933.7 W/m^2$, $\dot{m} = 0.68\ kg/s$, $T_{air} = 294.35\ K$ and $T_{in} = 375.35\ K$) using the Ramm-Johannsen analysis [2]

References

[1] V. Gnielinski. New equations for heat and mass transfer in turbulent pipe and channel flow. *International Chemical Engineering*, 16(2):359–363, 1976.

[2] D. Gärtner, K. Johannsen, and H. Ramm. Turbulent heat transfer in a circular tube with circumferentially varying thermal boundary conditions. *International Journal of Heat Mass Transfer*, 17:1003–1018, 1974.

[3] V. Dudley, G. Kolb, M. Sloan, and D. Kearney. SEGS LS2 solar collector-test results. Technical report, Report of Sandia National Laboratories (SANDIA-94-1884), 1994.

Appendix C

PTC performances using FVM in optical modelling

One of the first approaches used in the heat transfer model presented in Chapter 3 was to use the FVM for evaluating the solar radiation flux distribution in the receiver. Then, the first attempt was to couple the FVM developed in Chapter 2 in the general algorithm as a pre-processing for the calculation of the concentrated solar flux. The same cases described in table 3.1 have been simulated and compared with experimental results [1] for the cermet selective coating with air and vacuum in the annulus space. Figure C.1 shows the evolution of the heat losses and performance of the PTC respect to the HTF temperature obtained using the FVM for the optical modelling. According to this figure, the heat losses increase with the fluid temperature which give rise to the drop of thermal efficiency. The three components of thermal losses (conduction, convection and radiation) vary in different ways depending on the configuration of the receiver. When there is vacuum in the annulus, conduction and convection across the annulus is effectively eliminated. On the contrary, when there is no vacuum, the heat losses increase significantly due to convection and conduction, as expected. The results follow the same trend as the experimental ones of Dudley et al. [1] and show a fair agreement in the heat losses especially for low temperatures. However, there is an overestimation of the efficiency which is due essentially to the realistic conditions that are not considered in the optical model such as: dirt effect, shading, changes in reflection and refraction and selective coating incident angle effects.

Based on test case of Dudley et al. [1] ($I_b = 933.7W/m^2$, $\dot{m} = 0.68\ kg/s$, $T_{air} = 294.35\ K$ and $T_{in} = 375.35\ K$) the distribution of the temperature throughout the whole absorber and glass envelope is represented in figure C.2.

The non-uniform temperature distribution around the HCE follows the same trend as the solar flux distribution in the azimuthal direction. The temperature of the absorber increases with the increase of the axial direction as shown in figure C.3. The temperature is compared between three azimuthal position (0°, 90° and 180°).

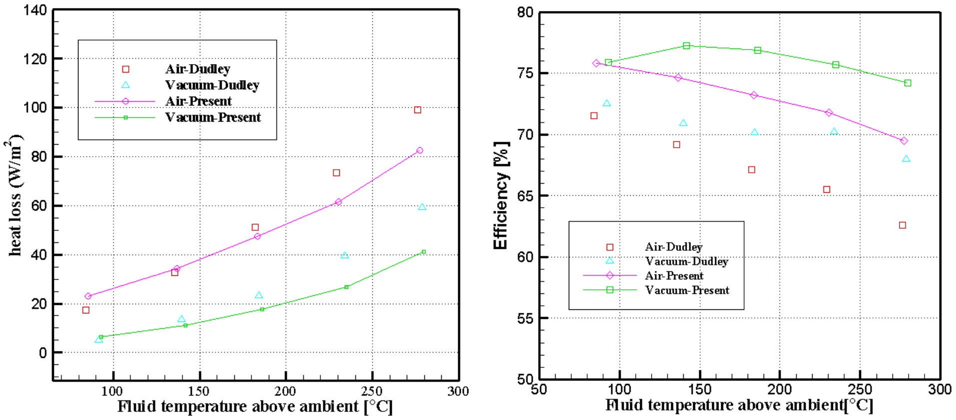

(a) (b)

Figure C.1: Comparison of the (a) heat losses and (b) Efficiency, with experimental results of Sandia Laboratories for air and vacuum in annulus using the FVM in optical modelling

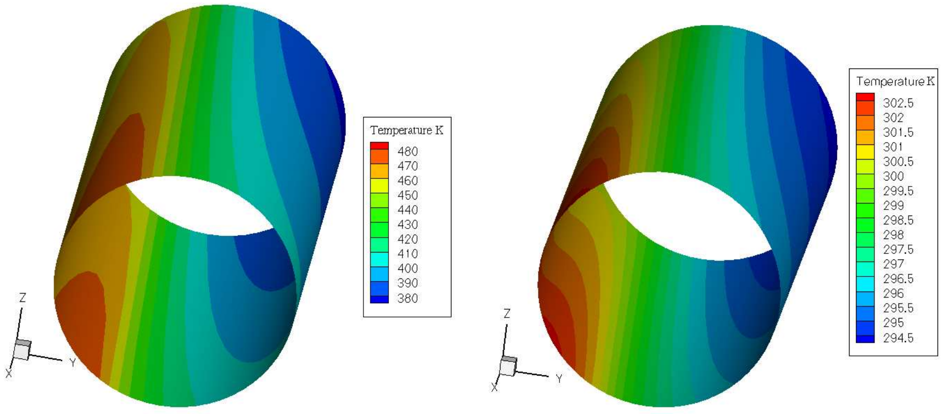

(a) (b)

Figure C.2: Distribution of the temperature of the whole (a) absorber and (b) glass envelope

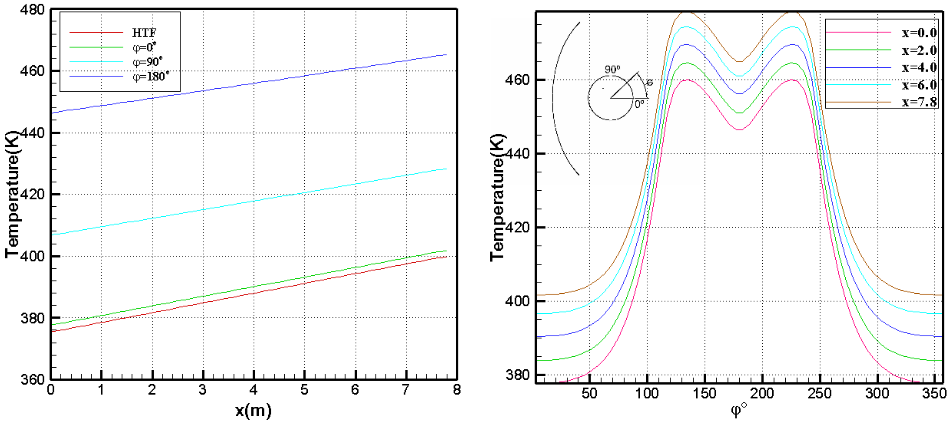

(a) (b)

Figure C.3: Variation of the temperature of the absorber (a) with the HTF along the axial direction and (b) azimuthal direction

The position 180° corresponds to the highest temperature because it receives more concentrated solar radiation while at 0° is the lowest one because there is no solar concentration in this direction (only direct radiation). The maximum of solar concentration is at about 135 ° which correspond to the maximum of the solar energy flux. By moving along the receiver, the same trend of the temperature distribution is conserved with a higher magnitude.

Even though, there is a good similarity in the overall thermal performances between the predicted results obtained with the FVM and the new optical model, it has been shown that the solar flux distribution profile is much more accurate with the new optical model (see Chapter 2) and take into account the finite size of the Sun. Thus, the temperature profile of both the absorber and glass envelope tubes will be more realistic and reliable with this optical model.

References

[1] V. Dudley, G. Kolb, M. Sloan, and D. Kearney. SEGS LS2 solar collector-test results. Technical report, Report of Sandia National Laboratories (SANDIA-94-1884), 1994.

Nomenclature

Latin symbols

A	area $[m^2]$
b	square side length $[m]$
B	interaction coefficient
Bl	blockage ratio
C_D	pressure coefficient
C_p	specific heat at constant pressure $[J/kgK]$
D	diameter $[m]$
e	thickness of the tube $[m]$
f	focal distance of the parabola or frequency
f_d	diffuse fraction of the reflectivity
F	view factor
$\mathcal{F}$	body forces
g	gravity$[m/s^2]$
GC	geometric concentration
h	convective heat transfer coefficient $[W/m^2K]$
$\hbar$	enthalpy [J/kg]
H	irradiation$[W/m^2]$
i	incident direction
I	irradiation per unit length $[W/m]$
I_b	Planck black body intensity $[W/m^2]$
J	radiosity $[W/m^2]$
k	thermal conductivity $[W/mK]$
l	control angle
L	length
$\dot{m}$	mass flow rate $[kg/s]$
n	normal direction to the reflector surface
N	number of control volumes
Nu	Nusselt number (hD/k)
p	period of vortex shedding
P	pressure $[Pa]$
Pr	Prandtl number $(\mu C_p/k)$
$\dot{q}$	net heat flux per unit of length $[W/m]$
q	radiative heat flux $[W/m]$

$\dot{\mathrm{Q}}$	power $[W]$
r	reflected direction
Ra	Rayleigh number $(g\beta_p\Delta TD^3/(\nu\xi)$
Re	Reynolds number $(\rho vD/\mu)$
s	distance travelled by a ray $[m]$
S	source function
St	Strouhal number (fD/U)
t	time$[s]$
T	temperature $[K]$
U	nondimensional velocity
v	velocity$[m/s]$
V	volume $[m^3]$
w	spatial weighting factor
W	aperture $[m]$
$\dot{\mathrm{W}}$	work $[W]$
X	non-dimesional distance
Greek symbols	
α	absorptance factor
β	spectral extinction coefficient
β_p	thermal expansion coefficient $[1/K]$
δ	molecular diameter $[m]$ or Dirac delta function
ϵ	emittance
η	efficiency
γ	intercept factor
κ	absorption coefficient
λ	mean-free path between collisions of a molecule
μ	dynamic viscosity $[kg/ms]$
ν	kinematic viscosity $[m^2/s]$ or wavenumber $[m^{-1}]$
ω	ratio of specific heat for the annulus gas
Ω	direction of observation
Φ	scattering phase function
ϕ	azimuthal direction
ϕ_s	finite size of the Sun
χ	dependent variable
κ	thermal diffusivity
ρ	density $[kg/m^3]$
ρ_s	specular reflectance

σ	Stefan-Boltzmann constant $5.67 \times 10^{-8} [W/m^2 K^4]$
σ_s	scattering coefficient
τ	transmittance or SGS stress tensor
τ_c	optical depth
ζ	non dimensional time
θ	circumferential direction or pitch angle
θ_{rim}	rim angle
φ	angle between the reflected ray and the x axis
ξ	thermal diffusivity $[m^2/s]$
Subscripts	
a	absorber
an	annular region
avg	average
c	collimated or collector
d	diffuse
$cond$	conduction
$conv$	convection
e	environment
eff	effective
ex	exterior
f	fluid
fsp	front stagnation point
g	glass envelope
in	input, Inner
inc	incident
opt	optical
out	output
ref	reflected
r	recirculation
s	sky
$s.inc$	solar incident
$s.rad$	solar radiation
std	standard temperature and pressure
$t.rad$	thermal radiation
th	thermal
u	useful
z	longitudinal direction

Abbreviations

CFD	computational fluid dynamics
CFL	Courant-Friedrichs-Lewy condition
CSP	concentrating solar power
CRS	central receiver system
DE	dish engine
$DISS$	direct solar steam
DSG	direct steam generation
FVM	finite volume method
GC	geometric concentration
HCE	heat collector element
HT	heat transfer
HTF	heat transfer fluid
IPH	industrial process heat
$ISCCS$	integrated solar combined cyle system
LCR	local concentration ratio
LES	large-eddy simulation
LFC	linear Fresnel collector
LS	Luz solar collector
$MCRT$	Monte Carlo ray-tracing method
MCV	million control volumes
NRM	net radiation method
ORC	organic Rankine cycle
PTC	parabolic trough solar collector
PTR	Schott solar receiver
$RANS$	Reynolds-averaged Navier-Stokes
RTE	radiative transfer equation
SCE	Southern California Edison
SGS	subgrid-scale
$SEGS$	solar electric generating system
PSA	plataforma solar de Almerìa
TES	thermal energy storage
$UVAC$	universal vacuum collector by Solel
VMS	variational multiscale

List of Publications

This is an exhaustive list of publications carried out within the framework of the present thesis.

Papers on International Journals

A.A. Hachicha, I. Rodríguez, R. Capdevila and A. Oliva. Heat transfer analysis and numerical simulation of a parabolic trough solar collector. *Applied Energy* 2013; 111: 582-592.

A.A. Hachicha, I. Rodríguez, J. Castro and A. Oliva. Numerical simulation of wind flow around a parabolic trough solar collector. *Applied Energy* 107 , pp. 426-437.

A.A. Hachicha, I. Rodríguez and A. Oliva. Wind speed effect on the flow field and heat transfer around a parabolic trough solar collector. *Applied Energy* (submitted) .

Articles on Conferences Proceedings

A.A. Hachicha, I. Rodríguez, R. Capdevila and A. Oliva. Numerical simulation of a parabolic trough solar collector considering the concentrated energy flux distribution In 30th ISES World congress, Kassel, Germany 2011, SWC 2011, (5), pp. 3976-3987

A.A. Hachicha, I. Rodríguez, R. Capdevila and A. Oliva. Large-eddy simulations of fluid flow and heat transfer around a parabolic trough solar collector In Eurosun conference, Rijeka, Croatia 2012

A.A. Hachicha, I. Rodríguez, O. Lehmkuhl and A. Oliva. On the CFD&HT of the flow around a parabolic trough solar collector under real working conditions In SolarPACES conference, Las Vegas, USA 2013